Numerical modelling of the thermal decomposition of methane to hydrogen and carbon black

by

Ambuj Punia

A thesis submitted in partial fulfillment of the requirements for the degree of

Doctor of Philosophy

Departments of Mechanical Engineering
University of Alberta

Abstract

Fossil fuel combustion results in carbon dioxide (CO_2) and particulate emissions which are linked to climate change and health problems, respectively. Hydrogen can be an alternative zero-emission fuel for future energy systems. However, hydrogen is not sufficiently available in nature in its pure form, so it needs to be extracted. Methane pyrolysis enables the production of hydrogen through the use of methane while eliminating its combustion thereby eliminating CO_2 and particulate emissions. Methane, heated to high temperatures in the absence of oxygen, converts to hydrogen, solid carbon, and a small fraction of intermediate hydrocarbons. The amount of products generated depends on the temperature and pressure of the reactor.

Methane pyrolysis is complex and results in many products in addition to hydrogen, such as ethane, ethylene, acetylene, naphthalene, and pyrene. Furthermore, the quality of carbon depends on the accurate prediction of intermediate species and carbon formation because of a number of reasons: a) first, the quantification of the intermediates helps in a better understanding of the pathways a fuel goes through while decomposing; b) the decomposition process can be controlled and optimized if the details about the intermediates are known; c) improved understanding towards carbon formation results in the development of a catalyst; and d) avoiding the formation of intermediates that are unsafe or reactive. A reaction mechanism reflecting the decomposition chemistry and a soot model is needed. Therefore, in the present work, we developed a detailed methane pyrolysis model capable of predicting intermediates and carbon formation.

To achieve this goal, different reaction mechanisms available in the literature were

integrated in a 0D isothermal, isochoric batch reactor model and the numerical predictions were compared to experimental results in literature at different temperatures and pressures. Results showed that almost all the detailed reaction models struggled to accurately predict the decomposition products at above-atmospheric pressures irrespective of carbon formation. The observed discrepancy was attributed to the slow rate parameters of the reaction mechanisms considered. Therefore, a methodology was developed to obtain a more accurate mechanism.

First, the mechanism showing the best agreement with the experimental data was selected and reduced using a graph-based method. Then, the rate parameters of the reduced mechanism in the high-pressure limit were recalculated by least-square parameter estimation until they accurately tracked methane and hydrogen mole fraction profiles while taking into account solid carbon formation. The optimized model was tested against the available experimental data in the high-pressure regime and shows significant improvement in its prediction capabilities compared to the original kinetic model. A reaction pathway analysis tracking carbon element shows that due to the change in the rate parameters, additional pathways, such as C_2H_5 <=> IC_3H_7 <=> NC_3H_7 <=> C_2H_4 <=> C_2H_3 <=> C_2H_2, appeared at high-pressure that previously were considered unimportant in driving up the decomposition process.

Finally, a transient 0D monodisperse population balance model was implemented to track soot formation during methane pyrolysis. The model accounted for particle formation due to soot nucleation, and its evolution due to soot agglomeration and surface growth. The model was validated against benchmark results from the literature and then it was coupled with the optimized gas-phase model. The combined model shows that soot nucleation acts for a very short duration and the particle evolution is mainly governed by soot agglomeration and surface growth. A compact and dense particle was predicted at lower and higher temperatures of 892 K and 1292 K, respectively, whereas at an intermediate temperature of 1093 K, a porous particle structure was predicted by the model. Additionally, it was found that the

surface growth model altered acetylene kinetics and increased its consumption rate compared to pure nucleation. A parametric study on the effect of soot nucleation for different residence times on particle formation revealed that extended soot nucleation leads to lower particle number concentration and the primary particle diameter at the end of the reaction. The model developed can be used to quantify the amount of soot generated during methane pyrolysis.

Keywords: methane pyrolysis, hydrogen, kinetic modeling, chemical kinetics, soot formation, reaction pathway, optimization.

Preface

Parts of Chapters 1, 2, 3, and 6 have been published as Punia, A., Tatum, J., Kostiuk, L., Olfert, J., and Secanell, M. (2023) "Analysis of methane pyrolysis experiments at high pressure using available reactor models". In: *Chemical Engineering Journal*, p. 144183 (available online at https://doi.org/10.1016/j.cej.2023.144183). I was responsible for conceptualization, literature review, model development, software implementation, data analysis, and manuscript writing and review. J. Tatum was responsible for conducting experiments, technical discussions, data analysis, and manuscript writing. L. Kostiuk helped with the conceptualization and manuscript review. J. Olfert helped with the conceptualization and manuscript review. M. Secanell was the supervising author and provided help with conceptualization and manuscript review.

Parts of Chapters 1, 2, 4, and 6 have been submitted for publication as Punia, A., Kostiuk, L., Olfert, J., and Secanell, M. (2024) "A reduced methane pyrolysis mechanism for above-atmospheric pressure conditions". In: *Chemical Engineering Journal*. I was responsible for conceptualization, literature review, model development, software implementation, data analysis, and manuscript writing and review. L. Kostiuk helped with the conceptualization and manuscript review. J. Olfert helped with the conceptualization and manuscript review. M. Secanell was the supervising author and provided help with conceptualization, manuscript writing and review.

I have co-authored the following publication: Tatum, J., Punia, A., Kostiuk, L., Secanell, M., and Olfert, J. (2023) "Analysis of methane pyrolysis experiments at high pressure using available reactor models". In: *Data in Brief*, vol. 47, p. 108953 (avail-

able online at https://doi.org/10.1016/j.dib.2023.108953). J. Tatum was responsible for conceptualization, literature review, conducting experiments, manuscript writing, and review. M. Secanell, L. Kostiuk, and I contributed equally to that publication and were responsible for manuscript writing, and review. J. Olfert was the supervising author and provided help with manuscript review.

Ambuj Punia

August 23, 2024

To my family

Acknowledgments

I would like to sincerely thank my Ph.D. supervisor, Dr. Marc Secanell (Department of Mechanical Engineering), for guiding me and making this happen. It was a challenge to move to a new country and you made sure I was at home all these years. Your constant support during the research really helped me in becoming a better researcher. Your knowledge in different fields of science continues to amaze me. Being your student in the finite element class or as a teaching assistant during MEC E 230, I always found your style of teaching to be one of the best that I came across so far. Finally, your way of cracking jokes is something I always look forward to. Thank you for being an awesome supervisor, once again.

I would like to thank my second Ph.D. supervisor, Dr. Jason Olfert (Department of Mechanical Engineering), for his guidance and various technical discussions. I have always learnt something new after our bi-weekly group meeetings, especially the research discussions you do in a jolly way.

In addition to my two supervisors, I would like to thank Dr. Larry Kostiuk (Department of Mechanical Engineering), of my supervisory committee for all the thoughtful comments and sponsoring my trip for Tsinghua-Princeton summer school on Combustion, 2018.

Coming to ESDLab for my Ph.D. was one of the best decisions as I was lucky to have such helpful labmates. Thank you James Tatum for performing the experiments and providing me with the experimental data. Looking forward to working with you in the future. Sincere thanks to Dr. Aslan Koskian who was always there to help me fix my code, and for coming with me to all the Indian restaurants. Thank you Dr.

Michael Moore for being such a wonderful labmate and for all your help during your stay at the ESDLab. Would love to meet again, especially in Dublin. Thank you Dr. Vaishnavi Kale for your help with optimization. I still miss those morning runs with you and Aslan. I extend my thanks to Dr. Manas Mandal, Elena, and all other past members of the group for their help.

I would like to acknowledge the financial support I received over the years from the Future Energy Sytems, that I was a part of and from MITACS for giving me a chance to work as an intern. Thank you Dr. Ehsan Abbasi Atibeh for your guidance and for funding the last two terms of my Ph.D.. Also, I am thankful for access to high performance computing clusters provided by the Digital Research Alliance of Canada (previously Compute Canada), which were critical resources that enabled me to complete my work.

Finally, I thank my parents, Mr. Kiran Pal Singh and Mrs. Manjula Chaudhary, and my sister, Mrs. Rashmi Singh, for their patience and unconditional love, and support. It would have been impossible to even get started with such a big commitment without their support.

Table of Contents

1 Introduction **1**

1.1 Motivation 1

1.2 Literature Review 4

1.2.1 Background 4

1.2.2 Experimental studies 6

1.2.3 Numerical studies 18

1.2.4 Mechanism reduction 26

1.2.5 Mechanism optimization 32

1.2.6 Reaction mechanism and reactor design software 34

1.2.7 Solid phase 35

1.2.8 Reactor design 43

1.3 Thesis Objectives 48

2 Methodology **50**

2.1 Pyrolysis reactor model 51

2.1.1 Gas-phase model 51

2.1.2 Carbon formation model 55

2.2 Kinetic model analysis 56

2.2.1 Thermodynamic analysis 56

2.2.2 Model reduction 59

2.2.3 Parameter estimation framework 64

2.2.4 Reaction path analysis 69

2.2.5 Soot formation model for the pyrolysis reactor 71

3 Mechanism selection 82

3.1 Results and discussion 82

3.1.1 Sub-atmospheric pressure operation 82

3.1.2 Above-atmospheric pressure operation 85

3.1.3 Discussion 99

3.2 Conclusion 100

4 Mechanism reduction and rate parameter optimization 102

4.1 Model reduction 102

4.1.1 High-pressure (HP) reduction 103

4.1.2 Low-pressure (LP) reduction 106

4.1.3 Discussion 107

4.2 Rate parameter optimization 108

4.2.1 Model validation at above-atmospheric pressure 109

4.2.2 Model validation at low-pressure 112

4.2.3 Discussion 117

4.3 Path flux analysis 118

4.3.1 Use of non-similar threshold values for the path flux analysis . 123

5 Carbon formation 124

5.1 Validation against the benchmark results 124

5.1.1 Pure coagulation 125

5.1.2 Coagulation and surface growth 126

5.1.3 Aggregation/agglomeration and surface growth 127

5.2 Soot formation during methane pyrolysis 129

5.2.1 Low temperature 129

5.2.2 Intermediate temperature 130

5.2.3 High temperature 131
5.2.4 Discussion 132

6 Conclusion and future work **141**
6.1 Conclusion 141
6.2 Future work 144

Bibliography **146**

Appendix A: Gas-phase experiments and modelling analysis **160**
A.1 Effect of carbon accumulation 160
A.2 Reaction path analysis 161
A.3 Equilibrium analysis calculation 161

Appendix B: Reaction-type entries and reduced model validation **169**
B.1 Reaction-type entries in Cantera 169
B.2 Model reduction data 169
B.3 Reduced model validation under low-pressure conditions 169
B.3.1 Original vs reduced model predictions 171
B.3.2 Reduced vs optimized model predictions 171

List of Tables

1.1 Summary of initial methane dissociation. 8

1.2 Experimental studies performed for understanding the kinetics of methane thermal decomposition 14

1.3 Rate parameters proposed for single-step kinetic modeling. 22

2.1 Reaction mechanisms used for MTD. 57

2.2 Sampling conditions for reducing the kinetic model using DRGEP at low and high pressures. 65

2.3 Parameters used for minimizing the objective function. 68

B.1 Reduction in the number of species and reactions with an increase in the error in the reduced model. 170

List of Figures

1.1 Experimental work conducted on methane pyrolysis using the batch (blue) and tube (black) reactors. Literature data are from references [22, 25, 31–43]. 6

1.2 Comparison of the log (k) vs temperature (K) for the initial dissociation of methane. The legends denote the studies from where the kinetic data was obtained: Kevorkian et al. [46], Kozlov and Knorre [54], Skinner and Ruehrwein [55], Bowman [52], Palmer and Hirt [53], Davidson et al. [51](denoted "Davidson et al.1"), Arutyunov and Vedeneev [33] and Davidson et al. [44] (denoted "Davidson et al.2"). 9

1.3 Schematic of soot formation. 38

1.4 Basic outline of a plug flow reactor. 44

2.1 Schematic of the DRGEP-based model reduction. 60

2.2 Schematic of the algorithm used to obtain the optimized values of the pre-exponential factors and the activation energies. 64

2.3 Schematic of the soot generated from the gas-phase in the present work. 70

2.4 Implementation of the soot model and coupling with the gas-phase model to obtain the particle morphology. 80

3.1 Experimental and numerical concentration of a) hydrogen; b) acetylene; c) ethylene; and d) ethane at 1038 K and 59 kPa. Markers represent the experimental data obtained from references [31, 32]. Lines represent the reaction mechanisms used, namely GRIMECH 3.0 [82], NUIGMech 1.1 [90], Ranzi et al. [87], Appel et al. [69], and AramcoMech 3.0 [83]. Data for H_2 was not available in reference [32]. . . . 83

3.2 Experimental and numerical concentration of a) ethylene; and b) ethane at 995 K and 59 kPa. Markers represent the experimental data obtained from reference [31]. Lines represent the reaction mechanisms used, namely GRIMECH 3.0 [82], NUIGMech 1.1 [90], Ranzi et al. [87], Appel et al. [69], and AramcoMech 3.0 [83]. 84

3.3 Experimental and numerical concentration of a) ethylene; and b) ethane at 1038 K and 13 kPa. Markers represent the experimental data obtained from references [32]. Lines represent the reaction mechanisms used, namely GRIMECH 3.0 [82], NUIGMech 1.1 [90], Ranzi et al. [87], Appel et al. [69], and AramcoMech 3.0 [83]. 84

3.4 Comparison of the model predictions against the in-house experimental data at 892 K and 398.8 kPa for a) methane; b) hydrogen; c) ethane; d) ethylene; e) acetylene; and f) carbon mass. Markers represent the experimental data obtained in this study. Lines represent the reaction mechanisms used, namely GRIMECH 3.0 [82], NUIGMech 1.1 [90], Ranzi et al. [87], Appel et al. [69], and AramcoMech 3.0 [83]. 86

3.5 Reaction flux diagram for hydrogen element at 0.5 atm (left) and 4 atm (right), 892 K and 300 s using a flux limit of 0.01. NUIGMech 1.1 [90]'s reaction mechanism was used to generate the flux diagram. 'fwd' and 'rev' are the net forward and reverse hydrogen element fluxes, respectively. The number above the 'fwd' flux represents the net flux as given by equation (2.2.22). 87

3.6 Comparison of the model predictions against experimental data at 1093 K and 398.8 kPa for a) methane; b) hydrogen; c) ethane; d) ethylene; e) acetylene; and f) carbon mass. Markers represent the experimental data obtained from this study. Lines represent the reaction mechanisms used, namely GRIMECH 3.0 [82], NUIGMech 1.1 [90], Ranzi et al. [87], Appel et al. [69], and AramcoMech 3.0 [83]. 90

3.7 Reaction flux diagram for hydrogen element at 0.5 atm (left) and 4 atm (right), 1093 K and 300 s using a flux limit of 0.1. A flux threshold was used to filter the reactions below the value provided in the sub-caption. NUIGMech 1.1 [90] reaction mechanism was used to generate the flux diagram. 'fwd' and 'rev' are the net forward and reverse hydrogen element fluxes, respectively. The number above the 'fwd' flux represents the net flux as given by equation (2.2.22). 'IND' in subfigure b refers to indene (C_9H_8). 91

3.8 Comparison of the model predictions for ethane at sub- and above-atmospheric pressure conditions. Markers in sub-figure a) represent the sub-atmospheric pressure experimental data obtained from reference [32] at 1103 K and 59 kPa, whereas the markers in sub-figure b) represent the high pressure experimental data obtained from the experimental facility at 1093 K and 398.8 kPa. Line represent the reaction mechanism used, namely NUIGMech 1.1 [90]. Note that y-axis data in sub-figure a) was available in concentration units and hence taken as it is from the article [32]. 93

3.9 Comparison of the model predictions against experimental data at 1292 K and 398.8 kPa for a) methane; b) hydrogen; c) ethane; d) ethylene; e) acetylene; and f) carbon mass. Markers represent the experimental data obtained from this study. Lines represent the reaction mechanisms used, namely GRIMECH 3.0 [82], NUIGMech 1.1 [90], Ranzi et al. [87], Appel et al. [69], and AramcoMech 3.0 [83]. Note that the results for the legend 'NUIGMech 1.1 with carbon' were obtained using a reduced NUIGMech 1.1 mechanism at 1292 K and 398.8 kPa. 95

3.10 Reaction flux diagram for hydrogen element at 0.5 atm (left) and 4 atm (right), 1292 K and 300 s using a flux limit of 0.1. A flux threshold was used to filter the reactions below the value provided in the sub-caption. NUIGMech 1.1 [90] reaction mechanism was used to generate the flux diagram. 'fwd' and 'rev' are the net forward and reverse hydrogen element fluxes, respectively. The number above the 'fwd' flux represents the net flux as given by equation (2.2.22). 'IND' in subfigures a and b refers to indene (C_9H_8). 96

4.1 Comparison of the number of species, number of reactions, and overall error with an increase in the threshold. 103

4.2 Comparison of the original and the reduced model predictions at 892 K and 398.8 kPa for: a) methane; b) hydrogen; c) ethane; d) ethylene; e) acetylene; and f) benzene. 104

4.3 Comparison of the original and the reduced model predictions at 1093 K and 398.8 kPa for: a) methane; b) hydrogen; c) ethane; d) ethylene; e) acetylene; and f) benzene. 104

4.4 Comparison of the original and the reduced model predictions at 1292 K and 398.8 kPa for: a) methane; b) hydrogen; c) ethane; d) ethylene; e) acetylene; and f) benzene. 105

4.5 Comparison of the original and the reduced model predictions at 1038 K and 59 kPa for: a) acetylene; b) ethylene; c) ethane; d) hydrogen; e) propene; and f) allene. 105
4.6 Reduction in least-square residual with an increase in the number of function evaluations using the reduced, perturbed, and random multi-start kinetic models as initial design variable sets. A Coliny pattern search method was used during the fitting process. 107
4.7 Comparison of the optimized and reduced model predictions against the experimental data at 892 K and 398.8 kPa for a) methane; b) hydrogen; c) ethane; d) ethylene; e) acetylene; and f) carbon. The triangle in CH_4 and H_2 indicates the mole fraction percentage predicted using the thermodynamic equation (1.2.1). 109
4.8 Comparison of the optimized and reduced model predictions against the experimental data at 1093 K and 398.8 kPa for a) methane; b) hydrogen; c) ethane; d) ethylene; e) acetylene; and f) carbon. The triangle in CH_4 and H_2 indicates the mole fraction percentage predicted using the thermodynamic equation (1.2.1). 110
4.9 Comparison of the optimized and reduced model predictions against the experimental data at 1292 K and 398.8 kPa for a) methane; b) hydrogen; c) ethane; d) ethylene; e) acetylene; and f) carbon. The triangle in CH_4 and H_2 indicates the mole fraction percentage predicted using the thermodynamic equation (1.2.1). 111
4.10 Comparison of the optimized model predictions against the experimental data at 1038 K and 13 kPa for a) ethane; and b) ethylene. 113
4.11 Comparison of the optimized model predictions against the experimental data at 1038 K and 59 kPa for a) acetylene; b) ethylene; c) ethane; d) hydrogen; e) propene; and f) allene. 113

4.12 Comparison of the optimized model predictions against the experimental data at 1103 K and 59 kPa for a) ethylene; b) ethane; and c) acetylene. 114
4.13 Comparison of the optimized model predictions against the experimental data from Arutyunov et al. [33] at 1100 K and 58 kPa for a) methane and hydrogen; b) acetylene; c) ethylene; and d) ethane. 115
4.14 Comparison of the optimized model predictions for methane and hydrogen against the experimental data Arutyunov et al. [33] at 1200 K and at a) 15 kPa; and b) 93 kPa. 116
4.15 Comparison of the optimized model predictions against the experimental data at 1200 K and 58 kPa for a) methane; b) hydrogen; c) acetylene; d) ethylene; and e) ethane. 117
4.16 Reaction flux diagram for carbon element at 892 K and 398.8 kPa using the reduced and the optimized kinetic models at 100 s. 'fwd' and 'rev' are the net forward and reverse carbon element fluxes, respectively. The number above the 'fwd' flux represents the net flux as given by Punia et al. [1]. The flux diagram was obtained using a threshold limit of 0.1 and 0.2 for the reduced and fitted reaction models, respectively. 119
4.17 Reaction flux diagram for carbon element at 1093 K and 398.8 kPa using the reduced and the optimized kinetic models at 100 s. 'fwd' and 'rev' are the net forward and reverse carbon element fluxes, respectively. The number above the 'fwd' flux represents the net flux as given by Punia et al. [1]. 120

4.18 Reaction flux diagram for carbon element at 1292 K and 398.8 kPa using the reduced and the optimized kinetic models at 100 s. 'fwd' and 'rev' are the net forward and reverse carbon element fluxes, respectively. The number above the 'fwd' flux represents the net flux as given by Punia et al. [1]. The flux diagram was obtained using a threshold limit of 0.1 and 0.25 for the reduced and fitted reaction models, respectively. 122

5.1 Aggregate number density (left) and particle diameter (right) comparison between the model implemented in this work and data reproduced from Kholghy et al. [151] for pure coagulation at 1830 K and 101325 Pa. 125

5.2 Aggregate number density (left) and soot volume fraction (right) comparison between the model implemented in this work and data reproduced from Kholghy et al. [151] for simultaneous coagulation and surface growth at 1830 K and 101325 Pa. 126

5.3 Comparison of a) the aggregate number density; b) the number of primary particles per aggregate; c) primary particle diameter; and d) the mobility diameter with the data reproduced from Kholghy et al. [151]'s model for simultaneous aggregation/agglomeration and surface growth at 1830 K and 101325 Pa in a premixed ethylene flame. 128

5.4 Transient evolution of a) soot particle number density; b) the number of primary particles per aggregate; c) soot primary particle diameter; d) soot particle mobility diameter; and e) soot particle gyration diameter, at 892 K and 398.8 kPa. 128

5.5 Transient evolution of a) soot particle number density; b) the number of primary particles per aggregate; c) soot primary particle diameter; d) soot particle mobility diameter; and e) soot particle gyration diameter, at 1093 K and 398.8 kPa. 130

5.6 Transient evolution of a) soot particle number density; b) the number of primary particles per aggregate; c) soot primary particle diameter; d) soot particle mobility diameter; and e) soot particle gyration diameter, at 1292 K and 398.8 kPa. 131
5.7 Transient evolution of soot particle number density for particle nucleation at 892 K, 1093 K, and 1292 K, and at 398.8 kPa. 132
5.8 Transient evolution of a) soot particle number density; b) the number of primary particles per aggregate; c) soot primary particle diameter; d) soot particle mobility diameter; and e) soot particle gyration diameter, at different nucleation times at 892 K and 398.8 kPa. 134
5.9 Transient evolution of a) soot particle number density; b) the number of primary particles per aggregate; c) soot primary particle diameter; d) soot particle mobility diameter; and e) soot particle gyration diameter, at different nucleation times at 1093 K and 398.8 kPa. 135
5.10 Transient evolution of a) soot particle number density; b) the number of primary particles per aggregate; c) soot primary particle diameter; d) soot particle mobility diameter; and e) soot particle gyration diameter, at different nucleation times at 1292 K and 398.8 kPa. 136
5.11 Transient evolution of experimental and model predictions of mole fraction (%) of acetylene with and without surface growth at 892 K and 398.8 kPa. 137
5.12 Transient evolution of experimental and model predictions of mole fraction (%) of acetylene with and without surface growth at 1093 K and 398.8 kPa. 138
5.13 Transient evolution of experimental and model predictions of mole fraction (%) of acetylene with and without surface growth at 1292 K and 398.8 kPa. 139

A.1 Hydrogen production as the test is repeated without cleaning at a) 899 K; and b) 1088 K. 161

A.2 Reaction flux diagram for hydrogen element at 892 K and 0.5 atm and 300 s. A flux threshold of 0.001 was used to filter the reactions below this value. The reaction mechanism used to generate the flux diagram was taken from reference [90]. 'fwd' and 'rev' are the net forward and reverse hydrogen element fluxes, respectively. The number above the 'fwd' flux represents the net flux as given by Equation (2.2.21). 162

A.3 Reaction flux diagram for hydrogen element at 1093 K and 0.5 atm and 300 s. A flux threshold of 0.03 was used to filter the reactions below this value. The reaction mechanism used to generate the flux diagram was taken from reference [90]. 'fwd' and 'rev' are the net forward and reverse hydrogen element fluxes, respectively. The number above the 'fwd' flux represents the net flux as given by Equation (2.2.21). 163

A.4 Reaction flux diagram for hydrogen element at 1292 K and 0.5 atm and 300 s. A flux threshold of 0.03 was used to filter the reactions below this value. The reaction mechanism used to generate the flux diagram was taken from reference [90]. 'fwd' and 'rev' are the net forward and reverse hydrogen element fluxes, respectively. The number above the 'fwd' flux represents the net flux as given by Equation (2.2.21). 164

A.5 Reaction flux diagram for hydrogen element at 892 K and 4 atm and 300 s. A flux threshold of 0.001 was used to filter the reactions below this value. The reaction mechanism used to generate the flux diagram was taken from reference [90]. 'fwd' and 'rev' are the net forward and reverse hydrogen element fluxes, respectively. The number above the 'fwd' flux represents the net flux as given by Equation (2.2.21). 165

A.6 Reaction flux diagram for hydrogen element at 1093 K and 4 atm and 300 s. A flux threshold of 0.03 was used to filter the reactions below this value. The reaction mechanism used to generate the flux diagram was taken from reference [90]. 'fwd' and 'rev' are the net forward and reverse hydrogen element fluxes, respectively. The number above the 'fwd' flux represents the net flux as given by Equation (2.2.21). 166

A.7 Reaction flux diagram for hydrogen element at 1292 K and 4 atm and 300 s. A flux threshold of 0.03 was used to filter the reactions below this value. The reaction mechanism used to generate the flux diagram was taken from reference [90]. 'fwd' and 'rev' are the net forward and reverse hydrogen element fluxes, respectively. The number above the 'fwd' flux represents the net flux as given by Equation (2.2.21). 167

A.8 Comparison of equilibrium hydrogen mole fraction in the gas phase (without solid carbon) obtained at different temperatures and 100 kPa pressure. The reference data for the equilibrium model validation was taken from Abanades et al. [9]. 168

B.1 Fall-off and pressure-dependent type reactions in Cantera [124] format in the input reaction mechanism. 169

B.2 Comparison of the original and the reduced model predictions at 1200 K and 58 kPa for: a) methane and hydrogen; b) acetylene; c) ethylene; and d) ethane. 170

B.3 Comparison of the fitted model predictions against the experimental data at 995 K and 59 kPa for a) ethylene; and b) ethane. 171

B.4 Comparison of the fitted model predictions against the experimental data at 1300 K and 59 kPa for a) methane; b) hydrogen; c) acetylene; d) ethylene; and e) ethane. 172

List of Symbols

Abbreviations

BDF Backward differentiation formula

CAHM Carbon addition and hydrogen migration

CFD Computational fluid dynamics

DRG Directed relation graph

DRGEP Directed relation graph with error propagation

DRGEPSA Directed relation graph with error propagation and sensitivity analysis

HACA Hydrogen abstraction, and acetylene addition

MTD Methane thermal decomposition

NIST National Institute of Standards and Technology

ODE Ordinary differential equation

OIC Overall importance coefficient

PAH Polycyclic aromatic hydrocarbons

PFA Path flux analysis

PFR Plug flow reactor

PV Photovoltaic

pyMARS Python based model automatic reduction

RRR Reaction reduction ratio

slpm Standard liter per minute

SMR Steam methane reforming

SRR Species reduction ratio

VCS Villars-Cruise-Smith algorithm

Constants

k_{b} Boltzmann's constant, 1.38065×10^{-23} J/K

R_{u} Universal gas constant, ≈8.314 J/(mol·K)

Greek

β particle collision frequency

$\dot{\chi}_{\mathrm{soot}}$ radical site density of the surface of soot particles

$\lambda_{\mathrm{particle}}$ particle mean free path, m

μ gas viscosity, Pa·s

μ_i chemical potential of the i^{th} species

ν_{ij} stoichiometric coefficient of the i^{th} species in the j^{th} elementary reaction

ρ_{soot} particle density, 1800 kg/m^3

Latin

A_j pre-exponential factor for the j^{th} elementary reaction, 1/s

A_{tot} total aggregate surface area, m^2/m^3

C_i concentration of i^{th} gaseous species

C_{tot} total carbon molar, mol/m^3

D diffusion coefficient, m^2/s

d_g gyration diameter of an aggregate

d_m mobility diameter of an aggregate

d_p	primary particle diameter
$E_{\mathrm{a},j}$	activation energy for the j^{th} elementary reaction, J/mol
G	total Gibbs energy of the mixture
g	mean particle distance
I	Total number of gaseous species in the reaction mechanism
J	Total number of elementary reactions in the reaction mechanism
K_s	reaction rate constant for adding an acetylene molecule to the surface of a soot particle
$k_{\mathrm{b},j}$	backward reaction rate constant, 1/s
$K_{\mathrm{eq},j}$	equilibrium constant for the j^{th} elementary reaction
$k_{\mathrm{f},j}$	forward reaction rate constant, 1/s
M	molar mass of a particular species, kg/mol
m	reactor mass, kg
m_{ag}	mass of a single aggregate, kg
N	Aggregate number density, $\#/\mathrm{m}^3$
n_j	temperature exponent for the j^{th} elementary reaction
n_p	number of primary particles in an aggregate
P	pressure inside the reactor, Pa
r_j	kinetic reaction rate for the j^{th} elementary reaction
S	production or consumption rate of a particular species, $\mathrm{mol}/(\mathrm{m}^3\mathrm{s})$
T	gas temperature inside the reactor
V	reactor volume, m^3
X_i	mole fraction of i^{th} species
Y	mass fraction

Chapter 1

Introduction[1]

1.1 Motivation

The global primary energy demand is expected to increase from 630 EJ in 2022 to 670 EJ by 2030 [4]. So far, to meet this demand, fossil fuels have played a major role and their burning has contributed to a rise in carbon dioxide (CO_2) emissions. CO_2 is a greenhouse gas and its emissions will continue to increase atmospheric concentrations leading to further increases in the temperature of the Earth by the end of the century [5]. This could lead to significant changes in the climate. Despite the negative impact that would arise from climate change, it has been estimated that, by 2030, fossil fuels will still provide 73% of the global energy demand even with a notable increase in the use of renewable energy, such as solar photovoltaic (PV) and onshore wind [6]. Since fossil fuels will still be used in the future to generate energy, technologies to mitigate CO_2 emissions, such as carbon capture [7], direct air capture [8], and methane decarbonization [9], will be required. While these methods

[1]Parts of this chapter are reproduced from the following published, under-review, and in preparation articles:

1. A Punia *et al.*, "Analysis of methane pyrolysis experiments at high pressure using available reactor models," *Chemical Engineering Journal*, p. 144 183, 2023.
2. J. Tatum *et al.*, "Dataset of methane pyrolysis products in a batch reactor as a function of time at high temperatures and pressures," *Data in Brief*, vol. 47, p. 108 953, 2023.
3. A. Punia *et al.*, "A reduced methane pyrolysis mechanism for above-atmospheric pressure conditions," *Chemical Engineering Journal*, vol. (Under review),

Author contributions are detailed in the Preface of this thesis.

can be used to capture carbon, some of them have economic and environmental constraints preventing their further utilization. For example, low-cost direct air capture technology is not expected to be economically viable in the near future [10]. The existing technologies for capturing, transporting, and storing CO_2 emissions need to be integrated and scaled up to an industrial level and proven to be economically feasible with current greenhouse gas emission taxation schemes [10].

Methane decarbonization through pyrolysis is considered a promising technique for CO_2 mitigation, as methane can be decomposed into hydrogen (H_2) while carbon black is captured in solid form. Hydrogen is a promising fuel candidate with the advantage of gross calorific value of around 142 kJ/kg [11] and zero carbon emissions, as its combustion generates only water vapor, heat, and oxides of nitrogen. Additionally, hydrogen can be used for other applications, such as in fuel cells [12], that can achieve much higher electric conversion efficiency, and many industrial applications, such as petroleum refining and ammonia synthesis [13], direct reduction of iron [14], or in residential building heating in cold climates [15–17]. The carbon can be used in different industrial applications, such as a pigment in inks [18], or as an ingredient to manufacture tires [19].

H_2 global annual demand grew by a factor of four between 1975 and 2018 [6]. That demand, however, has been met, primarily, by steam methane reforming (SMR) [20]. SMR is a two-stage process where hydrogen formation takes places via the steam reforming and the water gas shift reactions. In addition to the energy supplied to decompose methane during the reforming process, a quarter mole of CO_2 is released into the atmosphere to generate one mole of hydrogen [21]. Although the demand for natural gas, in which the major constituent is methane, is projected to flatten by 2040, however, it is still expected to play a vital role in meeting the energy demands, in the form of hydrogen production [4], in near future. Replacing natural gas reforming with pyrolysis can help meet the increasing hydrogen demand while curbing CO_2 emissions.

Methane pyrolysis has been academically studied since 1950's [22]. Higher operating temperature condition (above 1300 K) leads to increased plant operating cost, whereas, incomplete conversions are obtained if lower operating temperature is selected. Choosing the intermediate temperature range allows for the selectivity of the intermediate species produced. Further, this gives a provision to implement a catalyst in future which can be helpful in lowering the temperature requirements. The industrial scale-up of the process has not been possible so far due to a number of challenges. A key challenge is the lack of understanding of methane pyrolysis reaction kinetics under the high-pressure conditions at which industrial-scale reactors, ideally, should operate for obtaining higher conversions and a compact reactor system.

The overall objective of this research is to develop a kinetic model to understand the formation of hydrogen and solid carbon from methane pyrolysis in the temperature range of 892–1292 K and at a pressure of 398.8 kPa. To achieve this goal, first a detailed multi-step methane pyrolysis mechanism, suitable for high-temperature and high-pressure, must be developed. Then, the kinetic model will have to be implemented in a reactor model. As will be discussed below, a detailed methane pyrolysis mechanism does not currently exist for industrially relevant conditions. Therefore, a literature review in available kinetic models and intermediates observed, available experimental data, and, methods to estimate kinetic model parameters was performed to select an appropriate methodology for the thesis. Then, a reactor model had to be implemented. Therefore, a reactor model, including soot formation and reactor design, literature review is provided to justify software and soot model selection. Overall, the implications of the present research will be: a) better understanding of methane pyrolysis and its products under high-pressure conditions; b) the development of a mechanism reduction and rate parameter optimization framework and proposing the optimal rate parameters for high-pressure conditions; and c) the availability of a soot formation model for quantification of the amount of solids generated.

1.2 Literature Review

1.2.1 Background

Methane (CH_4) is a thermodynamically stable molecule and requires some energy to break its bonds. This dissociation of bonds is endothermic [23] and starts at around 803 K [24]. The overall reaction of methane decomposition can be given as [23]

$$\mathrm{CH_4(g)} \longrightarrow 2\,\mathrm{H_2(g)} + \mathrm{C(s)}, \qquad \Delta h_\mathrm{f}^\circ = 74.85 \ \mathrm{kJ/mol} \tag{1.2.1}$$

where $\Delta h_\mathrm{f}^\circ$ is the enthalpy of formation of CH_4. In literature [25], single-step is commonly assumed to describe the elementary reaction as given by Equation (1.2.1). Then, the reaction rate is assumed to be directly proportional to the rate constant given by the Arrhenius equation:

$$k = A \exp\left(-\frac{E_a}{\mathrm{R_u}T}\right) \tag{1.2.2}$$

where A is the pre-exponential factor (1/s) and denotes the frequency of collisions between the molecules, E_a is the activation energy (J/mol) representing the energy needed by the reactants to successfully convert into products, $\mathrm{R_u}$ is the universal gas constant (8.314 J/mol·K), and T is the temperature (K).

Unfortunately, although hydrogen and carbon black, assumed to be graphitic carbon, are the two principal products observed during methane pyrolysis, the decomposition must be described by a set of multi-step reactions [26] as a variety of intermediates are formed during the reaction in stages. In the primary stage, the decomposition takes place due to the initiation reaction leading to the breaking of C-H bond and forming radicals, such as methyl radical (CH_3). In the secondary or the propagation stage, the radicals formed recombine to form newer radicals or generate secondary species, such as ethane. Finally, in the tertiary or termination stage, heavier hydrocarbons that are stable in nature are generated, such as acetylene or benzene. A multi-step reaction mechanism provides an insight into the intermediate formation

at different temperatures, pressures, and reaction times, and is, therefore, needed to accurately predict the major and minor decomposition products.

Studying intermediates during a chemical reactions is necessary because: a) it helps in identifying the rate-determining step (the slowest elementary reaction path) that is critical in dictating the decomposition process; b) it helps in understanding the reaction paths through which methane dissociates and forms different intermediate species; and c) it helps in controlling the reaction process based on the requirement of a particular intermediate species. The formation of intermediates depends on the experimental conditions such as temperature, pressure, and residence time [27]. In fact, some of these intermediates, such as acetylene (C_2H_2), benzene (C_6H_6), naphthalene ($C_{10}H_8$), or pyrene ($C_{16}H_{10}$), are also assumed to be responsible for the amount of soot generated during the reaction. Therefore, an accurate understanding of methane pyrolysis requires a multi-step reaction mechanism consisting of pathways for the intermediates formation.

1.2.1.1 Importance of pressure

The decomposition chemistry of any fuel during combustion or pyrolysis is highly complex and depends on several important factors. One of those factors is pressure and can change the way a particular reaction behaves based on its magnitude. Large and small sized molecules generated during the decomposition process exhibit pressure-dependence. It can be in the form of generation of a particular species or a species undergoing isomerization [28, 29]. Green et al. [30] emphasized the importance of pressure-dependent reactions and mentioned that at times, half of the reactions in a mechanism can be pressure-dependent. Pressure effects can be much more pronounced at lower temperatures where temperature is not the primary driving force. Pressure dependent reactions can be classified as: a) fall-off; b) three-body; and c) pressure-dependent Arrhenius type reactions. Accurate estimation of products, hence, requires that the elementary reactions be considered pressure-dependent.

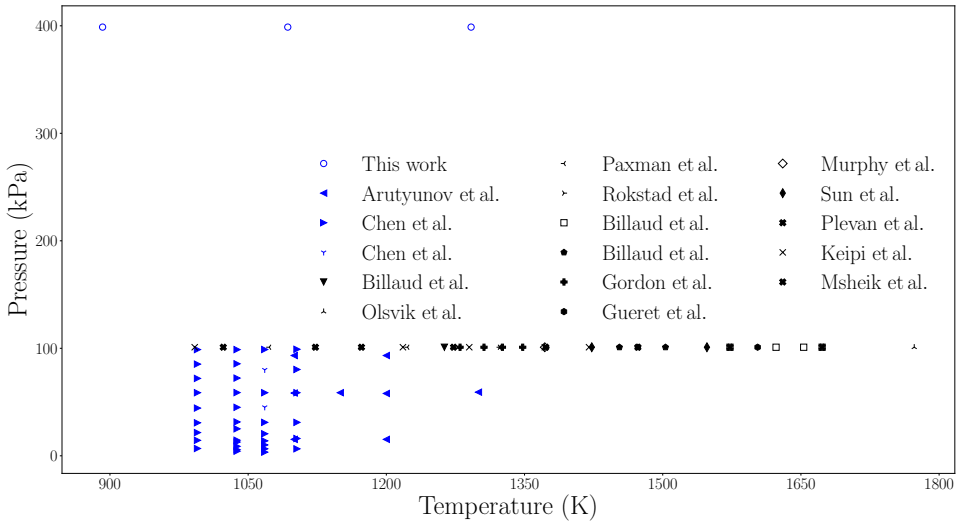

Figure 1.1: Experimental work conducted on methane pyrolysis using the batch (blue) and tube (black) reactors. Literature data are from references [22, 25, 31–43].

Therefore, a reaction mechanism should include reaction rate parameters accounting for the pressure-dependent reactions. This becomes even more pertinent when the reactor is required to be operated at conditions from low to high-pressures.

1.2.2 Experimental studies

In the literature, methane pyrolysis has been studied under shock tubes [44] involving very short residence times, flow reactors, and batch reactors. Except for the batch reactor experiments performed by two groups (Chen et al. [31, 32] and Arutyunov et al. [33, 45]) the majority of the studies have focused on either shock tubes [46–48] or flow reactors [34, 49]. Shock tubes represent homogeneous decomposition conditions and have been extensively used to study methane pyrolysis. Khan and Crynes [50] provided a summary on methane pyrolysis studies using shock tubes from 1960–1970's. However, the experiments performed in shock tubes are for a very short duration, and limits their applicability for industrial scale-up. Hence, shock tube studies were not considered a part of this work. The batch and flow reactor methane pyrolysis studies have been performed in the temperature and pressure range of 995–

1700 K and 0.1–1 atm [22, 25, 31–43], respectively. Figure 1.1 shows an overview of the studies performed and their range of temperatures and pressures.

Initial methane dissociation Determining the initial path of methane dissociation is paramount in the development of a methane pyrolysis mechanism. Based on the literature, methane can primarily decompose via two paths: a) disintegration into a methylene radical (CH_2) and a hydrogen molecule via Reaction 1:

$$CH_4 \longrightarrow CH_2 + H_2, \qquad (R_1)$$

or b) dissociation of methane to a methyl radical (CH_3) and a hydrogen atom via Reaction 2:

$$CH_4 \longrightarrow CH_3 + H, \qquad (R_2).$$

The dominating path is determined based on the rate constant of the respective reactions, i.e., the reaction with a larger value of the rate constant will dominate. Table 1.1 lists the reported rate parameters for the two reactions given. Using the data from the table, the values of the rate constants were plotted on a $\log(k)$ vs T over a temperature range of 1000–2000 K as shown in Figure 1.2. In the majority of the publications [33, 44, 51, 52], except for the study by Palmer and Hirt [53], the rate constant for the latter reaction, R_2, was reported to be considerably larger than that for former reaction (R_1). Therefore, it is likely that the second reaction dominates the initial methane dissociation and has been accepted as the initial dissociation reaction for methane decomposition.

Table 1.1: Summary of initial methane dissociation.

Reference	Experimental conditions	Reaction	Rate parameters
Kevorkian [46]	1656–1965 K & 6.8 atm	R_1	$k = 1.32 \times 10^{14} \exp\left(\frac{-93000}{RT}\right)$
Kozlov and Knorre [54]	1700–2200 K & 2–8 atm	R_1	$k = 4.5 \times 10^{13} \exp\left(\frac{-91000}{RT}\right)$
Skinner et. al. [55]	1200–1800 K & 5 atm	R_2	$k = 5.12 \times 10^{14} \exp\left(\frac{-100100}{RT}\right)$
Bowman [52]	1875–2240 K	R_2	$k = 2 \times 10^{17} \exp\left(\frac{-88427}{RT}\right)$
Palmer and Hirt [53]	1200–1800 K & 1 atm	R_2	$k = 10^{14.58} \exp\left(\frac{-103000}{RT}\right)$
Davidson et. al. [51]	1780–2320 K & 0.63–3.9 atm	R_2	$k = 1.04 \times 10^{18} \exp\left(\frac{-96319}{RT}\right)$
Arutyunov and Vedneev [33]	1100–1700 K & $<$ 1 atm	R_2	$k = 3.01 \times 10^{12} \exp\left(\frac{-81979}{RT}\right)$
Davidson et. al. [44]	1790-1325 K & 0.56-3.76 atm	R_2	$k = 8.17 \times 10^{16} \exp\left(\frac{-87488}{RT}\right)$

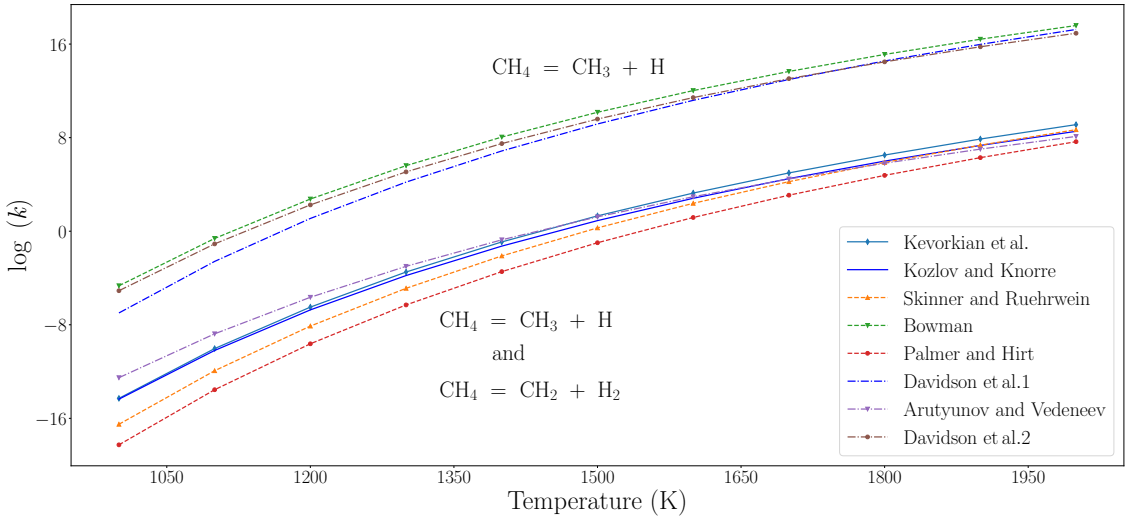

Figure 1.2: Comparison of the $\log(k)$ vs temperature (K) for the initial dissociation of methane. The legends denote the studies from where the kinetic data was obtained: Kevorkian et al. [46], Kozlov and Knorre [54], Skinner and Ruehrwein [55], Bowman [52], Palmer and Hirt [53], Davidson et al. [51](denoted "Davidson et al.1"), Arutyunov and Vedeneev [33] and Davidson et al. [44] (denoted "Davidson et al.2").

Analysis of intermediates Chen et al. [31, 32] studied methane thermal decomposition at low conversions ($< 1\%$) in a batch reactor in the temperature range of 995–1103 K and at sub-atmospheric pressures. Species containing carbon atoms up to C_3 were observed. Under those conditions, the initial rate of methane decomposition was found to be proportional to the formation of hydrogen and ethane. An increase in ethane concentration was observed during the tertiary stage of the reaction and was termed as autocatalysis. The homogeneous reactions were found to be responsible for this autocatalysis and the possibility of surface reactions catalysing ethane's concentration was discarded. Olsvik and Billaud [56] did not observe any autocatalysis during their experiments in a flow reactor at 1273 K and 1 atm. It was hypothesized that increased ethane kinetics led to an equal rate of ethane production and consumption at the higher temperatures. Arutyunov et al. [45] studied methane pyrolysis in a static reactor at 1100–1400 K and sub-atmospheric pressures. It was observed that with increase in temperature, the secondary species conversion, i.e. species contain-

ing double bonded hydrocarbons, such as ethylene, to tertiary species, i.e. species containing triple bonded hydrocarbons, such as acetylene, increased. In addition, different values of rate constant for the initial dissociation reaction of methane were observed at various pressures and the reaction was treated as a pressure-dependent reaction.

Flow reactor experimental studies are more common to study methane pyrolysis due to easy capturing of the intermediates and simplified conditions for the reactor modelling. Gordon [22] studied methane pyrolysis inside a quartz tube in the temperature range of 1280–1348 K and at a pressure of 1 atm and observed hydrogen, ethane, ethylene, acetylene, propene, propyne, and benzene as the principal products. The author observed that acetylene acted as a catalyst within the system and led to an increase in methane decomposition. Palmer et al. [57] performed methane pyrolysis inside a porcelain tube flow reactor in the temperature range of 1323–1523 K and observed ethane, ethylene, and acetylene with a first-order decomposition rate in methane. A chain reaction process was proposed by the following reactions

$CH_4 \longrightarrow CH_3 + H$, (initiation)

$CH_4 + CH_3 \longrightarrow C_2H_6 + H$, (propagation)

$H + CH_4 \longrightarrow CH_3 + H_2$, (propagation)

$2\,CH_3 \longrightarrow C_2H_6$, (termination)

$H + CH_3 \longrightarrow CH_4$, (termination)

It was hypothesized that carbon generated from the gas-phase would accelerate the decomposition rate, therefore, small concentration (around 1%) of naphthalene ($C_{10}H_8$) was added to the inlet gas. The added naphthalene acted as a soot precursor and the decomposition was found to increase to 37.2% compared to 1.2% without it. The

decomposition process has also been controlled by targetting a particular intermediate species. For example, targeting acetylene, Holmen et al. [58] pyrolyzed a mixture of methane and hydrogen in a graphitic tubular reactor at elevated temperatures of 1773–2273 K and 1 atm for short residence times. Acetylene yields, defined as the molar flow rate of acetylene to feed methane flow rate, in the range of 85-90% were obtained. The type of carbon formed inside the reactor was found to be dependent on the amount of methane decomposed. At low-conversions, carbon in the form of graphite was observed, whereas at high-conversions, the carbon deposited on the wall looked more like a soot with less compact nature. A step-wise model for methane decomposition to carbon was proposed and was given as $2CH_4 \longrightarrow C_2H_6 + H_2 \longrightarrow C_2H_4 + H_2 \longrightarrow C_2H_2 + H_2 \longrightarrow 2C + H_2$. Murphy et al. [42] pyrolyzed methane at 1372 K inside a flow reactor at 1 atm. Acetylene was the principal gas-phase product whereas benzene, followed by naphthalene, was the main constituent among the aromatic compounds observed. The path to carbon formation was hypothesized to be starting from acetylene as an intermediate, and the heavier hydrocarbons were considered as co-products instead of intermediates. Sun et al. [37] used a tubular quartz system and pyrolyzed methane in the temperature range of 1273–1583 K and at 1 atm. At 1583 K, methane conversion was around 20% of which 32% was carbon, and the rest as C_2's and heavier hydrocarbons. With a decrease in the flow rate, methane conversion was found to increase, whereas the selectivity of the secondary hydrocarbons decreased. Serban et al. [59] performed another study on methane pyrolysis by passing the feed gas through either a blank reactor or a molten metal reactor in the temperature range of 873–1173 K and at 1 atm. Under such conditions, only methane conversion was reported and was found to be proportional to the gas bubble diameter and the time of contact between the gas and the surrounding molten media. Information on the intermediates formed was missing.

Hydrogen dilution Flow reactor experiments have also studied methane pyrolysis with hydrogen in the inlet mixtures. Due to the use of hydrogen, the intermediates concentrations change as the decomposition chemistry changes. Rokstad et al. [60] observed the evolution of ethylene, acetylene, and benzene during methane pyrolysis in the temperature range of 1273–1473 K and at 1 bar pressure inside a flow reactor. To increase the yield of ethylene and acetylene, different initial feed ratios of hydrogen and methane were used and carbon formation was suppressed. At such temperatures, ethylene and acetylene concentrations were found to approach theoretical equilibrium values, while the obtained benzene concentration was lesser than the equilibrium value. Hydrogen dilution was also found to be more effective in suppressing carbon formation and reducing methane conversion, similar to the observations in other studies [39, 61]. Billaud et al. [40] continued this research in the temperature range 1573–1673 K and 1 atm and found that with an increase in temperature, the addition of hydrogen in the inlet for short residence times leads to larger amounts of C_2 hydrocarbons. Hydrogen dilution suppressing carbon formation and resulting in higher selectivity of C_2 hydrocarbons was also observed in parametric studies in references [38, 41, 43] and theoretically in the study by Gueret et al. [24]. It can be concluded that with the inclusion of hydrogen in the inlet fuel mixture, the formation of intermediates increases and carbon formation gets suppressed.

From the literature review on the experimental studies, the following can be concluded: a) methane pyrolysis involves primary, secondary, and tertiary intermediate species ranging from C_2–C_{10} and a kinetic model should account for these species; and b) most of the pyrolysis studies have been performed under atmospheric pressure conditions. Some of the recent methane pyrolysis studies have also focused on conducting experiments at atmospheric pressure or below [9, 22, 25, 31–43, 49, 62, 63]. Table 1.2.2 contains a summary of gas-phase experimental studies. Davis et al. [64] mentioned that the majority of the foundational research on methane pyrolysis has been conducted at sub-atmospheric pressures. Without the availability of

high-pressure methane pyrolysis data, our understanding of methane thermal decomposition under these conditions has been limited so far as intermediate concentrations cannot be predicted. Hence, there is a need for high-pressure methane pyrolysis experiments.

Table 1.2: Experimental studies performed for understanding the kinetics of methane thermal decomposition

Author	Press, Temp	Species Observed	Reaction mechanism	Reactor type	Remarks
Chen et. al.[31]	995–1103 K, 59–71 kPa	H_2, C_2H_2, C_2H_4, and C_2H_6	**Experimental** and proposed mechanism	Inside a batch reactor for 20–40 min	Investigated the initial rate of methane decomposition. Paths were proposed for the reactions occuring inside the reactor, and autocatalysis (sudden rise) in concentration of ethane was observed in the tertiary stage of the reaction.
Billaud et. al. [40]	1263 K, 1 atm	H_2, C_2H_2, C_2H_4, C_2H_6, C_3H_6, C_3H_4, C_5H_6, C_4H_6, and C_6H_6	**Experimental** and modified a base mechanism and added some more reactions.	Inside a flow reactor for 0–6 s	Modified Roscoe and Thompson's [65] mechanism and validated the model with in-house flow reactor experimental results. However, the modified mechanism was validated only for half of the experimental residence time and the results start to diverge afterwards. Did not observe any auto-catalysis phenomenon at higher temperature as proposed by Chen et. al. [31]. The full experimental dataset is used for validating the numerical model in the current study.
Olsvik and Billaud [38]	1273 K, 1 bar	C_2H_2, C_2H_4, C_6H_6 and C_2H_6	**Experimental** and a reaction mechanism proposed	Inside a flow reactor for 0–2.3 s	Methane was pyrolysed at 1273 K and 1 bar. Simulations were carried out at 30 K below the maximum experimental temperature. The data has been used in the current study for comparison.

Olsvik et. al. [38]	1473–1773 K, 1 atm	Major: H_2, C_2H_2, C_2H_4, C_6H_6 and carbon Minor: C_2H_6	Both and a reaction mechanism proposed	Inside a flow reactor for 0–0.6 s	Methane was pyrolysed in the presence of hydrogen as diluent and it was found that methane conversion decreases with increase in hydrogen-to-methane ratio. Also, ethylene was found to be independent of H_2 to CH_4 ratio, whereas the concentration of acetylene increases with an increase in the above ratio. A mechanistic model including 36 reactions for up to C_6 species was proposed for methane pyrolysis for hydrogen diluted conditions. A sensitivity analysis was done to account for the discrepancies in the simulation and experimental results.
Murphy et. al. [42]	1372 K	Mainly higher hydrocarbons (Benzene, pyrene etc.) and CH_4, C_2H_4 and C_2H_2	**Experimental**	Based on flowrate	Analyzed the volatile products from the pyrolysis of methane. Acetylene was found to be the major gas phase species at the exit of the reactor ($\approx$ 0.48 mol %) and a close relationship was observed between the solid carbon and acetylene. Overall, the conversion of the hydrocarbons was very low ($\approx$ 1-7%). At such temperatures, heavier hydrocarbons dominated the percentage of liquid products observed.
Arutyunov [33]	1000–1400 K, 15–100 kPa	H_2, C_2H_2, C_2H_4, C_2H_6	**Experimental** and Proposed mechanism	Inside a batch reactor for 30 min	Pyrolysed methane using a quartz static reactor. Carbon formation was observed at around 1100 K and a decrease in the concentration of C_2 was seen as an indication. A 22% increase in the final pressure was observed when the experiments were done at 1200 K. The experimental data has been used to validate the model in the current study.

Gordon [22]	1280, 1306, 1326, and 1348 K, 1 atm	H_2, C_2H_2, C_2H_4, C_2H_6, C_3H_6, C_3H_4 and C_6H_6	**Experimental**	Inside a flow reactor for 0–15 s	Studied the effects of acetylene and hydrogen addition with methane as the inlet mixture on methane decomposition. Acetylene was found to accelerate methane decomposition. Addition of hydrogen increased the reaction rate and more ethylene and acetylene were observed for the same amount of methane decomposition. This was in contradiction to the hydrogen inhibition effect observed in [66]. Additionally, increase in methane decomposition was observed with increase in surface to volume ratio of the reactor.
Davidson [44]	1790–2325 K, 0.56–3.76 atm	CH_4	**Experimental**	Inside a shock tube for 0–300 μs	Pyrolysed methane in a shock tube and determined the rate coefficient expression for the reaction given below. $$CH_4 + Ar \rightarrow CH_3 + H + Ar \quad (1.2.3)$$
Sun et. al. [37]	1548 K, 1 atm	C_1-C_5 alkane, alkene and benzene along with solid carbon.	**Experimental**	Inside a flow reactor for 100 μs	Investigated methane pyrolysis in a hot filament (platinum based) reactor. Carbon build up on the filament lowered the reaction temperature and altered the conversions.

Kevorkian [46]	1656–1965 K	CH_4	**Experimental**.	Shock	Investigated methane pyrolysis in a shock tube reactor and determined the initial rate of methane decomposition. The rate parameters for methane decomposing to methylene radical (CH_2) is given by: $k = 1.32 \times 10^{14} \exp\left(\frac{-93000}{RT}\right) \mathrm{s}^{-1}$
Rokstad et. al. [67]	1273–1473 K, 1 atm	Major: H_2, C_2H_2, C_2H_4, C_6H_6 and carbon. Minor: C_2H_6, C_3H_8, C_3H_6 and other	**Experimental**	Inside a flow reactor for 0–0.36 s	Hydrogen (added to inlet methane) was found to suppress carbon formation and led to a higher selectivity of C_2 hydrocarbons. Further, increasing the surface-to-volume ratio of the reactor, while diluting methane with helium, played no role in methane conversion as opposed to reference [22]. A small increase in methane conversion was observed when hydrogen was used as a diluent.

1.2.3 Numerical studies

The thermal decomposition of methane is complex and capturing all the species at the time scale of the decomposition chemistry is difficult as thousands of species can generate for a fraction of seconds. Numerical research on methane pyrolysis have either focused on thermodynamic modeling or kinetic studies aiming at accurately predicting the decomposition products. Kinetic models vary in complexity and can be further classified as single-step or multi-step reaction mechanisms. The first subsection aim at the equilibrium modeling work performed in the literature and estimating different species concentrations. The second subsection is about the use of single-step kinetic models. Single-step kinetic models lack the detailed knowledge about the intermediates and are useful only if methane conversion is of interest. The last subsection focus on the multi-step kinetic modeling and provides the literature review on the intermediate quantification, path to soot formation. Below, the different approaches are reviewed.

1.2.3.1 Equilibrium modelling

Chemical equilibrium is obtained when the Gibbs energy of the system is at its minimum. Therefore, state properties, such as temperature and pressure, the choice of species dictates the amount of methane decomposed and the reaction pathway does not affect the results.

A number of studies have performed numerical simulations targeting equilibrium compositions under different temperatures and pressures. Davis et al. [64] performed equilibrium simulations for methane pyrolysis at temperatures ranging from 1000–2200 K and at pressures from 6.7–34 atm. The species considered were hydrogen, methyl radical, methane, acetylene, ethylene, ethane, diacetylene, and vinylacetylene. Methane conversion was different when the equilibrium simulations were performed with or without solid carbon. Therefore, carbon is critical and should be accounted for in the equilibrium modeling. Gueret et al [24] considered methane,

ethylene, acetylene, hydrogen, and benzene in the system, and identified the dominant species across the temperature range 773–2503 K and at pressures of 0.1 atm, 1 atm, and 20 atm. Sinaki et al. [68] used the species in the reaction mechanism by Appel et al. [69] and performed equilibrium calculations for methane at 473–1873 K and 0.1–10 atm. The results were found to be consistent with LeChatelier's principle [70] where lower pressure leads to higher conversion values. Larkins and Khan [71] performed equilibrium analysis of methane thermal decomposition across the temperature range 800–1500 K and 0.1–3 MPa. It was found that the aromatic formation reduces the Gibbs free energy of the system with an increase in temperature, and the species formed were, thus, stable. The trends indicate that the equilibrium composition depends on the number of species considered and experimental species can be taken into account while performing the evaluation. Based on the review, it can be concluded that most of the thermodynamic equilibrium studies have been performed at both low and high-pressures. Hence, the available equilibrium studies can be used to test the predictions of the kinetic models in this work whether they are below the equilibrium concentrations or not.

1.2.3.2 Single-step kinetic modelling

A single-step kinetic model, i.e., Equation (1.2.1), has been used in various studies to estimate CH_4 conversions [25, 36]. The key reaction parameters while evaluating methane conversion are: a) pre-exponential factor (A (1/s)); b) temperature exponent (n); and c) activation energy (E_a (J/mol)). The equation for the change in methane concentration is given by the law of mass action:

$$\frac{dC_{\mathrm{CH_4}}}{dt} = -AT^n \exp\left(\frac{-E_a}{R_u T}\right) C_{\mathrm{CH_4}}^m \tag{1.2.4}$$

where $C_{\mathrm{CH_4}}$ is the concentration of methane ((mol/m^3)), and m is the reaction order. Olsvik and Billaud [56] proposed the kinetic rate parameters for the overall single-step reaction at 1273 K and 1 bar to accurately track methane conversions. Due

to an uncertainty in the residence time, two different sets of rate parameters were proposed. Steinberg [72] proposed kinetic rate parameters for methane pyrolysis in a perfectly mixed reactor in the temperature range of 973–1173 K and 2.83–5.67 MPa. Assuming a first order reaction rate, the activation energy for the methane decomposition to hydrogen and carbon was significantly lower than the values reported in the literature [25]. Dahl et al. [73] studied methane pyrolysis inside a flow reactor model assuming plug flow reactor conditions. Kinetic rate parameters for the global reaction were proposed assuming a reaction order of 4.4 in methane. Wyss et al. [74] developed a vertically oriented plug flow reactor model to study methane pyrolysis in the temperature range of 1700-2135 K. The authors proposed single-step rate parameters assuming a reaction order of 7.2 $\pm$ 6.9 in methane. The reaction order values were significantly higher in the studies by Dahl et al. [73] and Wyss et al. [74] than the reported values in the literature that usually have a reaction order of 1 and could have lead to a lower methane conversion if the literature values were used. Trommer et al. [75] proposed reaction rate parameters for the overall methane thermal decomposition with carbon particles in the feed. Around 90% methane conversion was obtained at a temperature of 1500 K and for a residence time of 0.3 s. Abanades and Flamant [76] used the activation energy from Trommers single-step rate kinetics and modified the pre-exponential factor in a numerical study at 1563–1813 K and 101 kPa. Higher conversions of methane (around 97%) and hydrogen yields (around 90%) were obtained. The modelling results showed that the decomposition was dependent on reactor wall temperature, heat transfer across the reactor wall, and the surface area for the reaction. Abanades and Flamant [77], in another study, studied methane pyrolysis in the temperature range of 1500–2000 K and 1 atm. Three different set of kinetic parameters were proposed for the single-step reaction assuming first order decomposition in methane. Rodat et al. [78] studied methane pyrolysis under the temperature range of 1500–2300 K and sub-atmospheric pressures (25–40 kPa) and estimated the single-step reaction rate parameters based on non-catalytic reac-

tions inside a plug-flow reactor. Homayonifar et al. [79] studied methane pyrolysis in the range 880–1644 K and 101 kPa and proposed single step reaction rate parameters. Paxman et al. [25] modelled vertically oriented plug flow, perfectly mixed, and perfectly mixed with bypass type reactors for methane pyrolysis in the temperature range of 1023–1373 K and 33–224 ccm and proposed kinetic parameters for each of those configurations. The kinetics for latter reactor model agreed with values available in the literature and depended on the buoyancy effects. Other studies in the literature have also used single-step reaction chemistry [79–81]

Table 1.3: Rate parameters proposed for single-step kinetic modeling.

Reference	Temperature	Pressure	Pre-exponential factor (A)	Temperature exponent (n)	Activation energy (E_a)
Khan and Crynes [50]			1.3×10^{14}	-	151–422 kJ/mol
Steinberg [72]	973-1173 K	2.8–5.6 kPa	5.4×10^{3}	-	131 kJ/mol
Dahl et al. [73]	1533–2144 K	101.325 kPa	6×10^{11}	-	208 kJ/mol
Paxman et al. [25]	1023–1373 K	101.325 kPa	1.3×10^{14}	-	151–422 kJ/mol
Rodat et al. [78]	1670–1770 K	101.325 kPa	6.6×10^{13}	-	370 kJ/mol
Abanades et al. [77]	1563–1810 K	101.325 kPa	2.5×10^{7}–4.5×10^{7}	-	147 kJ/mol
Keipi et al. [36]	1070–1450 K	1 atm	Forward: 8.5708×10^{12}, backward: 1.119×10^{7}	Forward: 1.123, backward: 0.9296	Forward: 337.12 kJ/mol, backward: 243.16 kJ/mol

Based on the review and the kinetic rate parameters proposed, it can concluded that kinetic rate parameters vary by orders of magnitude and there is no clear consensus between the studies on the actual value of the decomposition parameters. Table 1.3 gives the data on the range of kinetic rate parameters proposed for the single-step reaction. It is hypothesized that the rate determining step/pathway might change with conditions and therefore such a simple model is not suitable for a large reactor operating range leading to the observed discrepancy in the rate values. Single-step kinetic models are useful only if the yield of final products is of interest within a very narrow range of operating conditions. Although these studies were not a part of this work, the experimental data may be valuable to validate a detailed chemical kinetic model in the future. With a slight change in the reactor operating conditions, such as dilution of methane with an inert gas, accurately predicting methane and hydrogen formation will require newer set of rate parameters. Additionally, with the availability of the experimental data under different reactor conditions and improvement in our understanding of the reaction chemistry these one-step models are quickly being replaced by models that include multiple elementary reactions [69, 82–86] accounting for the pressure effects.

1.2.3.3 Detailed kinetic modelling

Multi-step reaction mechanisms are used to describe the reaction process by a combination of different parallel paths consuming and forming multiple species at the same time. In a multi-step mechanism, the formation rate of each species depends on the contribution from the different elementary reaction rates and is governed by the law of mass action. As multi-step reaction mechanisms can provide in-depth kinetic details about methane pyrolysis, such as determination of the rate-determining step, they represent a detailed chemical process.

Mechanisms proposed A number of the kinetic mechanisms for methane pyrolysis have originated from combustion mechanisms, from which the reaction steps containing oxygen are removed and the filtered mechanism is used to model pyrolysis conditions [26]. Fau et al. [26] performed a comparison of different combustion and pyrolysis mechanisms available in the literature against the sub-atmospheric data available in the literature [31, 32]. Smith et al. [82] proposed a methane combustion reaction mechanism containing 325 reactions and 53 species (key species methane, hydrogen, ethane, ethylene, and acetylene). That mechanism is by far the most accepted for methane combustion and has been validated against a wide range of combustion conditions. However, when converted to a pyrolysis model by simply removing all oxygen-involving reactions and species, the kinetic model results in large deviations from the intermediate species profiles reported by Chen et al. [31]. Furthermore, this mechanism is restricted to lower hydrocarbons (up to C_2), and thus its applicability is limited in terms of high-pressure conditions as a lot of heavier hydrocarbons are generated. Even highly detailed combustion mechanisms [87–90] containing thousands of reactions and hundreds of species struggle while tracking the gas-phase products of methane pyrolysis [26]. Implementation of combustion mechanisms for the pyrolysis conditions is based on the rationale that pyrolysis is a part of combustion process. However, there is a significant difference between the kinetics of a pyrolysis process and its combustion counterpart. For example, the fuel dissociation path in a pyrolytic process can be different from the one observed during combustion experiments. Additionally, because combustion typically takes place at higher temperatures and shorter time scales than pyrolysis, the combustion mechanisms [82, 87–89] and their rate constants may not be valid for the methane pyrolysis conditions. Sinaki et al. [91] used the mechanism proposed by Appel et al. [69] to model methane pyrolysis and observed significant differences in the species profiles until the kinetic parameters were modified to reflect the pyrolytic conditions as opposed to rich combustion pyrolysis where a small amount of oxygen is present.

Initial dissociation of methane to CH_3 and H was used by Chen et al. [31] in proposing a methane pyrolysis mechanism consisting of around 20 reactions for sub-atmospheric conditions. The mechanism, however, was not able to capture and explain the sudden rise in ethane concentration during the tertiary stage (> 1500 s) of the reaction when the reactions responsible for acetylene formation were dominant. This sudden rise in ethane concentration was termed as autocatalysis. To address the autocatalysis, Roscoe and Thompson [65] adjusted the mechanism by Chen et al. [31] by adding reactions of isomerization, propagation, and termination, and fitting some of the rate parameters based on sensitivity analysis for species upto C_3. The mechanism proposed consisted of 64 elementary reactions and was validated against the experimentally observed autocatalysis phenomenon in ethane concentration by Chen et al. [31]. As the model proposed contained lighter hydrocarbons, Billaud et al. [35] extended the mechanism by adding species up to C_6, e.g., C_6H_6, resulting in a 119- elementary step reaction mechanism. The model was able to predict species containing one to six carbon atoms at a temperature and pressure of 1263 K and 1 atm for short residence times up to 3 s. The mechanism of Roscoe and Thompson [65] was not able to predict the autocatalysis phenomenon when the elementary reactions were treated as reversible. Dean [92] observed this discrepancy in the mechanism by Roscoe and Thompson [65], and proposed an updated mechanism consisting of 44 reactions and 25 species. Additional reactions containing cyclopentadiene formation were attributed to the autocatalysis phenomenon and added in the mechanism. This mechanism was capable of capturing the experimental conditions of Chen et al. [31] at 1038 K and 59 kPa. However, large deviations were observed when the same mechanism was used to model experiments at 995 K and 1103 K, and 59 kPa. Matheu et al. [29] argued that the value of the enthalpy of formation of cyclopentadienyl radical in Dean's proposed mechanism had a discrepancy of 4 kcal/-mol compared to recent data [93]. The results of the model changed drastically once the enthalpy of formation was replaced by the most recent values. This conclusion

led the authors to propose a new mechanism containing more than 100 species and 1000 reactions to track the experiments of Chen et al. [31]. The new mechanism can reproduce the experimental conditions of Chen et al. [31] with errors up to 35% while tracking Chen et al. [32] data at 1038 K and 13 kPa. The mechanism was designed to specifically track Chen et al.'s conditions and dealing with such a large mechanism hinders its usage in multi-dimensional computational fluid dynamics simulation software. It is for this reason that it was not used in this thesis.

The applicability of the multi-step reaction mechanisms proposed in references [29, 31, 32, 35, 56, 65, 78, 79, 85, 91, 92] reflected only a particular experimental condition and might not be valid under other operating conditions, especially at higher pressures. The list of all relevant species and their reactions in a mechanism are unknown a priori and can only be inferred. To the best of the authors knowledge, no reaction mechanism exists that can be used to model methane pyrolysis over the range of the pyrolytic conditions presently studied (900–1400 K and 0.1–4 atm). It is hypothesized that the inaccurate predictions from the proposed models across the range of temperature and pressure are due to the inaccuracy of reaction pre-exponential factors and the activation energies.

Additionally, the lack of experimental data at high-pressure further adds to the problem of obtaining a reliable methane pyrolysis mechanism. Therefore, one aim of this research is to test the reactor models available in the literature for high-pressure methane pyrolysis conditions.

1.2.4 Mechanism reduction

Progress in the understanding of reaction pathways over the last few decades has resulted in a multifold increase in the size of the reaction mechanisms. The size of fuel determines complexity and subsequently the size of the reduced mechanism. For example, for methane combustion, the reaction mechanism now contains upto 10000 reactions and 1000 species [82, 83, 90]. Matheu et al. [29] focused on the development of

C_1 fuel chemistry for low-pressure conditions and a mechanism consisting of around 1000 reactions to capture Chen et al. [31, 32]'s experimental data was proposed. The authors concluded that the mechanism might give deviations if implemented outside the conditions for which it was proposed. Some of the combustion problems require coupling a reactor model with computational fluid dynamics (CFD) simulations. It is known that CFD alone can be computationally expensive, and numerically solving such a complex system can impose a tremendous computational load, especially if the reactor model is multi-dimensional. Even the commercial CFD codes can generally handle a maximum of 50 species using fine mesher [94]. Additionally, it is to be noted that complex mechanism will have many fitting parameters making the optimization problem difficult to converge [1]. Fitting rate parameters of a detailed mechanism is desirable to reproduce the experimental data. However, using detailed mechanisms in multi-dimensional simulations, coupled with a solid-phase model, makes the system of governing equations stiff due to fast gas-phase chemistry. To solve such a system, solver step-sizes of the order of micro-seconds are required that pose a significant computational load. Reducing a mechanism, i.e., removing unwanted reactions and species, to an acceptable level while maintaining the accuracy of the gas-phase chemistry for the target species can help make the fitting process easier. In fact, some of the reaction pathways are so fast that excluding them from the detailed model induces negligible error in model's accuracy but significantly reduces the computational cost. One of the ways to reduce the computational expense of reactor simulations is to reduce the size of the mechanism while preserving its accuracy within an error range with respect to the quantities of interest, such as species concentrations, ignition delay time, and flame velocities [95–97]. In the context of methane pyrolysis the quantities of interest would be species concentrations.

Generally, a mechanism reduction method works on the principle of the identification of species and reactions that are redundant in terms of accurately predicting the target quantities. To identify the unimportant species and reactions, a number

of methods have been proposed in the literature, such as the calculation of reaction rates, jacobian analysis [98], sensitivity analysis [65], and graph-based methods [96].

Method of reaction rates [98] In this method, the unimportant or redundant species are removed from the detailed mechanism one at a time and the reduced model is obtained for each species removal. Each reduced model is required to be validated against the detailed model and the mechanism giving the best agreement is then selected. The reduction approach is easy, however, only for small mechanisms. For the case where thousands of species are present, it can impose a tremendous computational load as each time a species is removed, the reduced mechanism needs to be tested against the original mechanism predictions and will need a lot of iterations. Additionally, at times there is a set of species which should either be kept in the mechanism or be removed altogether [96]. Hence, in this case, removing one species at a time from the mechanism might not work.

Method of jacobian analysis [98] is based on the analysis of the jacobian. If the rate of production of the target species is not affected by a change in the concentration of a particular species, the species is considered as unimportant, as its removal does not produce a significant error in the target species concentration. The jacobian used to analyze the condition was given as:

$$J_i = \sum_{x=1}^{X} \left(\frac{\partial \log \omega_x}{\partial \log C_i} \right)^2 \tag{1.2.5}$$

where J_i is the jacobian, X is the number of target species, ω_x is the production or consumption rate of species x, C_i is the concentration of species other than x. In each iteration, the method identifies the coupling of target species with other species in the mechanism and the sets of strongly coupled species are kept in the reduced mechanism. The process is repeated until the specified error is reached.

Sensitivity-based mechanism reduction [65, 98] A small perturbation in the rate coefficient is done to analyse the change in the target species concentration and the unimportant species are removed similar to the method of jacobian analysis.

Method of detailed reduction [86] was used to reduce a detailed mechanism for flame modelling simulations. The reaction rate for each reaction was compared with the rate of a pre-selected reaction (i.e., rate-limiting step), and the reactions having a significantly lower value than the rate-limiting step were considered unimportant. The application of this method, however, poses a challenge as, in a large mechanism, the rate-limiting step can change over the course of the reaction.

Graph-based methods have also been used to perform mechanism reduction. In this method, a number of target species are selected to remove in the detailed mechanism that have less importance. The importance is quantified using an importance coefficient calculated using the species production rates and their impact on the target species depending on the method used. Examples of graph-based methods are Directed relation graph (DRG) [96], DRG with error propagation (DRGEP) [97], DRG-aided sensitivity analysis (DRGASA) [99, 100], Directed relation graph with error propagation and sensitivity analysis (DRGEPASA) [95, 101].

Out of the above, graph-based methods have gained significant attention as they are fast and generate significantly reduced mechanisms. For example, Lu and Law [96] proposed DRG method and reduced a kinetic model consisting of 70 species and 463 elementary reactions to a skeletal model consisting of 33 species and 205 reactions. The importance coefficient quantifying the dependence of the target species A on other species B in the mechanism was calculated using the following equation:

$$r_{AB} = \frac{|\sum_{j=1}^{J} \upsilon_{\mathrm{A},j} r_j \delta_{\mathrm{B}}^{j}|}{|\sum_{j=1}^{J} \upsilon_{\mathrm{A},j} r_j|} \tag{1.2.6}$$

where r_j is the reaction rate for the j^{th} elementary reaction, J is the number of

reactions, and $\upsilon_{\mathrm{A},j}$ is the stoichiometric coefficient of target species A in the j^{th} elementary reaction.

$$\delta_{\mathrm{B}}^{j} = \begin{cases} 1 & \text{if the } j\text{th elementary reaction} \\ & \text{involves species B,} \\ 0 & \text{otherwise.} \end{cases}$$

Similarly, Sarathy et al. [102] proposed a skeletal mechanism for 2-methylheptane using DRG method and a detailed mechanism consisting of 714 species and 3397 reactions was reduced to a mechanism consisting of 151 species and 989 reactions. Yao et al. [103] reduced a detailed mechanism proposed by You et al. [104] consisting of 60 species and 522 reactions to a skeletal mechanism consisting of 54 species and 269 reactions.

DRG method, however, has limitations as it considers equal importance for every species included in the mechanism. This consideration is not necessarily true as some species might have more impact on the target species compared to others in the mechanism. The limitation was identified by Pepiot et al. [97] and the authors presented an modified version of DRG called DRGEP. The method established the error propagated down the reaction paths in the graph based on a modified importance coefficient as given below:

$$r_{\mathrm{AB}} = \frac{|\sum_{j=1}^{J} \upsilon_{\mathrm{A},j} r_j \delta_{\mathrm{B}}^{j}|}{\max(Q_{\mathrm{A}}, L_{\mathrm{A}})} \tag{1.2.7}$$

where

$$Q_{\mathrm{A}} = \sum_{j=1}^{J} \max(0, \upsilon_{\mathrm{A},j} r_j) \tag{1.2.8}$$

$$L_{\mathrm{A}} = \sum_{j=1}^{J} \max(0, -\upsilon_{\mathrm{A},j} r_j) \tag{1.2.9}$$

A number of studies have performed mechanism reduction [105] for pyrolysis and combustion cases. However, most of the mechanism reduction studies [96, 97] have focused on reducing the fuel chemistry for application-specific combustion cases, such

as n-heptane and iso-octane fuels, that can otherwise contain more than 10,000 reactions and hundreds of species. A limited number of studies have attempted mechanism reduction for methane pyrolysis applications. Dean [92] performed a sensitivity analysis-based mechanism reduction for methane pyrolysis at 995–1103 K and 10–59 kPa. The original mechanism consisting of 438 reactions and 122 species was reduced to a skeletal mechanism containing 44 reactions and 25 species. The reduced mechanism had good agreement with the experimental data [31, 32] under sub-atmospheric conditions. However, the mechanism failed to accurately predict the decomposition products at other experimental conditions [45]. The most recent mechanism reduction study for methane pyrolysis was performed by Shinde et al. [94] using DRG method. The authors reduced a detailed reaction mechanism generated consisting of 318 reactions and 37 species to a skeletal mechanism consisting of 29 reactions and 13 species targeting sub-atmospheric chemical vapor deposition/infiltration processes involving methane pyrolysis. The sampling condition were the partial pressure of methane in the range of 10–100 kPa and a temperature range of 1173–1373 K. The target species chosen were CH_4, H_2, C_2H_2, C_2H_4, and C_6H_6. To date, mechanism reduction for methane pyrolysis has only been performed at sub-atmospheric pressures [92, 94, 106–109].

Based on the literature review on mechanism reduction, a number of methods, such as method of reaction rate, method of jacobian, and graph-based methods are available to perform mechanism reduction. The non graph-based methods are slow and might take a lot of iterations to reduce the mechanism and have not been used in the present thesis. Among the graph-based methods, DRGEP method was selected to perform the mechanism reduction as it quickly removes the species and reactions and generates a compact mechanism for the same level of accuracy.

1.2.5 Mechanism optimization

Once the mechanism is reduced, it must be verified to accurately track the species of interest. The initial fuel decomposition chemistry changes due to the removal of species and reactions from the original mechanism. Fitting the reduced mechanism rate parameters against the available experimental data can help minimize the observed deviation in the reduced mechanism. Several studies have been performed where the rate parameters, such as the pre-exponential factors, temperature exponents, and activation energies, have been optimized to work for the application-specific combustion-based reactor operating conditions [110–115].

Some simple methane pyrolysis reaction optimization studies have been performed in the literature. Paxman et al. [25] proposed a set of rate parameters for a global reaction for methane decomposition through a flow reactor with and without molten metal. Roscoe and Thompson [65] used sensitivity analysis to modify the reaction rate parameters of the most sensitive reactions and accurately predicted autocatalysis in ethane during Chen et al. [31]'s experiments. Sinaki et al. [91] modified the most sensitive reactions in the original mechanism proposed by Appel et al. [69] using the data available for the elementary reactions in the literature and proposed an updated mechanism for low-pressure methane pyrolysis. Keipi et al. [36] used a simplified one-step kinetic mechanism to analyze methane pyrolysis products obtained in a flow reactor in the temperature range of 1070–1450 K. The forward and the backward rate parameters for the global reaction were optimized using 'fminsearch' method in MATLAB [116] to track the experimental data. Furthermore, the authors compared the predictions of a 37-step kinetic model proposed by Ozalp et al. [81] with the optimized mechanism predictions and found discrepancies in the detailed model [81]. The kinetic model predictions were further improved by adjusting the rate parameters of the most sensitive reaction. The detailed model, however, was limited in terms of predicting heavier hydrocarbons. An issue with the single-step model equation pro-

posed by Keipi et al. [36] was that it was thermodynamically inconsistent. Hence, the model overpredicted the equilibrium conversion of methane at high-pressures. This was identified in a recent study by Catalan and Rezai [21]. To deal with the issue, the authors modified the single-step kinetic model of Keipi et al. [36] and made the expression for methane decomposition a function of the forward rate constant and the equilibrium constant. Keeping the equilibrium constant the same, the authors optimized the pre-exponential factor, activation energy, and the forward reaction order against the experimental data in reference [36] using MATLAB [116]'s 'lsqnonlin' function. Becker et al. [117] examined different flow reactors to understand their impact on methane pyrolysis. The collision factor and the activation energy for the one-step reaction were fitted against the experimental data collected for different reactor material types. Different values of optimized pre-exponential factor and activation energy were obtained for different reactor materials. Single-step kinetic optimization is easy but find limited applicability when applied to high-pressure methane decomposition inside a batch reactor as a lot of pressure-dependent intermediates are generated.

Sensitivity analysis and optimization can be used as a tool to obtain optimal reaction rate parameters for detailed mechanisms. For example, Sinaki et al. [91] used a sensitivity analysis approach to update the values of the rate parameters of a previously published combustion mechanism by Appel et al. [69] to reflect the pyrolytic conditions of Chen et al. [31]. The most significant rate parameters were identified. Some of those parameters were updated with the values from the NIST database [118], and the rest were fitted to experimental data to track the experimental species profiles of Chen et al. [31] for residence time up to the secondary stage. Large deviations, however, were observed in the tertiary stage of the reaction. Frenklach et al. [110] found the methane combustion rate parameters at a range of experimental conditions using a combination of sensitivity analysis and a quasi-Newton based optimization algorithm. Sensitivity analysis was used to first identify the most critical elementary reactions, and their rate parameters were used as design variables in a response

surface based optimization. Cai and Pitsch [119] provide another example of using optimization for parameter fitting. These optimization approaches coupled with sensitivity analysis, to the best of the author's knowledge, have not been used to perform methane pyrolysis-specific reaction mechanism optimization. To the best of the author's' knowledge, none of the existing mechanisms are capable of accurately predicting batch reactor data obtained from methane pyrolysis at low-high temperature and high pressure. Hence, another objective of this thesis is to develop a mechanism reduction framework to reduce a kinetic model and obtain optimal set of kinetic rate parameters by least square optimization of the experimental data.

1.2.6 Reaction mechanism and reactor design software

To develop a framework for parameter estimation, an appropriate reaction mechanism software and optimization algorithm are needed. The proposed kinetic models above include the solution of tens or hundreds of transient mass conservation equations. Therefore, many of them have been implemented in specialized softwares. For example, Fincke et al. [85] used CHEMKIN-PRO [120] to model plasma pyrolysis of methane in a flow reactor. COSILAB [121] was used by Franzelli et al. [122] to model kerosene–air premixed flames. The package is, however, limited to simpler reactor types or combustion geometries. CHEMKIN-PRO and COSILAB are commercial softwares in which it is difficult to implement model specific changes. For example, Langer et al. [123] reported that relative and absolute tolerances for a 0D homogeneous reactor model cannot be implemented in CHEMKIN-PRO. Open source packages, on the other hand, can be easily adjusted. Cantera [124] is a recently developed open-source software package that has been used for modeling combustion and pyrolysis conditions [125, 126]. OpenSmoke++ [127] has also been used in different studies [128, 129]. Cantera is widely used due to its easier implementation across a wide range of platforms, such as MATLAB, Python and Fortran. Additionally, Cantera allows interfacing with other open–source platforms, such as OpenFOAM, as

shown by Yang et al. [130]. Hence, Cantera [124] has been used in the present work.

1.2.7 Solid phase

Soot are carbonaceous particles, mainly consisting of carbon, formed during the incomplete combustion or pyrolysis of hydrocarbon fuels. Carbon black, on the other hand, is composed of pure carbon atoms and is a valuable product. Soot and carbon black have the same formation process, however, the majority of the literature is based on soot formation in combustion rather than carbon black production. Hence, in the present context of methane pyrolysis, solid carbon is defined by a soot formation model. Formation of solid carbon occurs in several stages. Initially, methane decomposes into light hydrocarbons, such as acetylene (C_2H_2), ethylene (C_2H_4), ethane (C_2H_6) and propane (C_3H_8). As the reaction proceeds, heavier aromatic hydrocarbons form. These hydrocarbons, called PAHs (polycyclic aromatic hydrocarbons) are thermodynamically stable and are believed to be soot precursors [131]. The first soot particle (dimer of two PAH molecules) then nucleates by the collision of two PAH molecules. This process is called soot nucleation or inception. Once a soot particle is formed, other processes, such as coagulation, surface growth and PAH condensation, also play an important role in the formation of solid carbon. Thus, an understanding of all stages of the solid phase formation is required in order to correctly describe the thermal decomposition of methane and fine tune the process to produce carbon black with the desired characteristics (i.e. surface area, electrical conductivity, pore size) for a commercial product. Understanding soot formation during methane pyrolysis is of paramount importance and it takes place via the following mechanisms: a) precursor formation, b) soot nucleation, c) soot coagulation, d) soot aggregation; and e) soot surface growth. These mechanisms are discussed below, and their interaction is shown in Figure 1.3.

Soot precursor

The solid phase formation mechanism starts with the decomposition of gaseous fuel to form aromatics, such as benzene (C_6H_6) with a single aromatic ring given by the notation - A1. These aromatics then combine to form heavier hydrocarbons called soot precursors. Soot precursors are mostly polycyclic aromatic hydrocarbons (PAH's) with naphthalene ($C_{10}H_8$) as the simplest PAH having two rings (A2). Estimating the concentration of soot precursors is vital in order to predict the inception or nucleation of soot as the path leading to the soot particle is defined by the precursors. Josephson et al. [132] considered pyrene (A4 : $C_{16}H_{10}$) to be the only soot precursor while modeling soot formation during burning of solid fuels. Agafonov et al. [133] used coronene ($C_{24}H_{12}$) as the soot precursor while modeling methane pyrolysis behind reflected shock waves. Jain and Xuan [134] considered a range of species starting from naphthalene to cyclopenta[cd]pyrene ($C_{18}H_{10}$) as soot precursors. Other studies conducted in references [135, 136] also used naphthalene as the soot presursor. Usually, species in the range of 10–30 carbon atoms are considered as PAH's. Matsukawa et al. [137] experimentally observed that a minimum of 24 carbon atoms constitute a soot precursor in the temperature range 1150–1730 K. Similarly, Oktem et al. [138] experimentally found that PAH's containing 16–30 carbon atoms dominate the soot chemical composition. Selection of soot precursor also depends on the species in the gas phase chemistry employed.

Soot nucleation

Nucleation is the process of reactions that form new particles. Particle nucleation is a result of collisions between two PAH molecules of sufficient size as proposed by Frenklach and Wang [139]. The nucleation rate mainly depends on the concentration number density ($\#/m^3$) of the soot precursors and the collision frequency between the two precursors. The collision frequency usually is a function of the gas regime, namely, free–molecular, transition or continuum regime, and is decided by the Knudsen number which is a ratio of the molecular mean free path to the particle radius,

however, for nucleation the regime remains free–molecular. References [85, 132, 140] proposed that soot nucleation occurs by collision of two PAH molecules and the nucleation rate is given by [132]

$$R_{\text{nucleation}} = \sum_{i=1}^{i=I_{\text{bins}}} \sum_{k=1}^{k=K_{\text{bins}}} \beta_{i,k}^{\text{PAH}} N_i^{\text{PAH}} N_k^{\text{PAH}} \tag{1.2.10}$$

where $\beta_{i,k}^{\text{PAH}}$ is the collision frequency between the two sectional molecules having concentration N_i and N_k.

Another theory proposed for soot nucleation is the reactions of acetylene with PAH's leading to the first soot particle. Mckinnon and Howard [141], however, discarded the possibility of soot nucleation through the acetylene route. Additionally, Wang [142] found that the rate of an acetylene-induced particle nucleation was too slow to dominate the process and that PAH's majorly contribute to the primary particle. A simplified model by Lindstedt et al. [143] proposed that soot nucleation can be assumed to occur via the decomposition of acetylene to carbon. Other complex mechanisms for nucleation are also available, however they require heavier hydrocarbons for which the gas-phase chemistry needs to be accurate resulting in a detailed mechanism. Based on the above discussion, the model propsed by Lindstedt et al. [143] will be used in the present study to model soot nucleation.

Freshly nucleated soot particles can increase in size through different growth mechanisms, such as coagulation, aggregation and surface growth [132]. Coagulation and aggregation result in an increase in particle size due to the collision of soot particles. Surface growth increases the particle size by reactions of soot particle with acetylene. Figure 1.3 presents an overall scheme of soot produced during methane pyrolysis. Individual soot growth mechanisms are discussed next.

Soot coagulation

Soot coagulation can be defined as the collision of two particles, thereby forming a larger particle. The coagulation rate depends on the soot concentration number

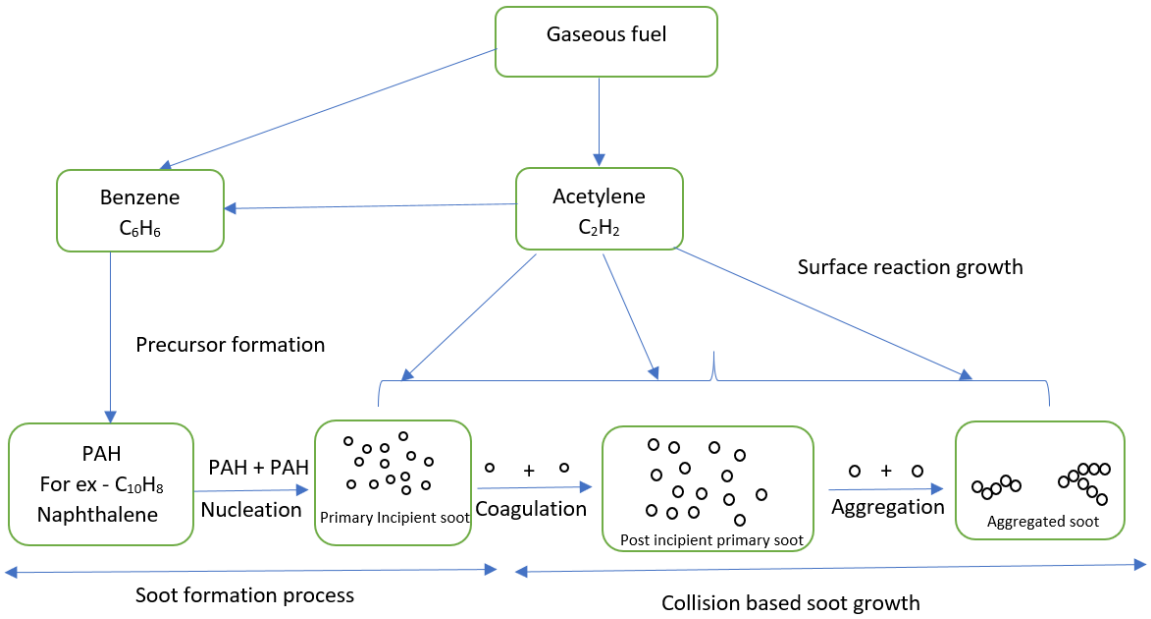

Figure 1.3: Schematic of soot formation.

density and the collision frequency describing the rate of collisions between the soot particles. Due to coagulation, the soot particle number density decreases, whereas the particle size distribution broadens.

Soot particle growth due to coagulation can occur via different collision mechanisms. For example, two soot particles can collide to form a larger particle. Additionally, a soot particle and a PAH molecule or a soot particle and a PAH radical can also contribute to the soot growth. Josephson et al. [132] studied the amount of soot produced while burning solid fuels and implemented the above-mentioned coagulation sub-models.

Evaluation of coagulation rate depends on accurate prediction of the collision frequency. Collision frequency is a function of the type of particle regime which is decided by the Knudsen number given in equation (1.2.11).

$$\mathrm{Kn} = \frac{2\lambda}{d} \tag{1.2.11}$$

where λ is the mean free path of the gas and d is the particle diameter [144]. The Knudsen number determines the degree of deviation from the continuum regime.

Frenklach and Harris [145] assumed a free molecular approach while modeling soot coagulation. However, Rogak and Flagan [146] found that the coagulation behaviour is quite different in the transition regime as compared to free molecular or continuum regime as the collision frequency attains a different value. Later, Kazakov and Frenklach [147] extended their previous work [145] to include the continuum and transition regimes for modeling soot coagulation and aggregation, and proposed a single expression for calculating the collision frequency for all the regimes. The model was validated against the data for laminar premixed ethylene–air flames.

Soot aggregation

Following coagulation, further growth of soot particles is governed by soot aggregation. In soot aggregation, particles collide and stick, and lead to the formation of chain-like fractal structures. The spherical shape of the colliding primary particles remains preserved during aggregation [132].

Determining the transition of soot growth from coagulation to aggregation is paramount to achieve accurate model predictions as soot growth due to coagulation is limited up to a certain size [148] and particles below that size are considered as single spheres. Some studies assumed a minimum particle size, above which agglomeration was expected to occur [137, 149]. Sirigano et al. [150] observed that the aggregation rate beyond a soot size of 20 nm dominated over other soot growth phenomena, such as soot coagulation. The authors used the same values of kinetic parameters as proposed for molecular growth and particle inception to model particle aggregation. Saggase et al. [149] assumed a reference particle size of 13 nm to model the soot growth due to aggregation. Recently, Kholghy et al. [151] proposed a monodisperse population balance model to characterize soot particles with just four governing equations, i.e., the aggregate number density (N), the carbon molar (C_{tot}), total aggregate surface area (A_{tot}), and the aggregate mass (m_{ag}). In this way, the particle can be charaterized in terms of the primary particle diameter, the number

of primary particles in an aggregate, particle mobility diameter, and particle gyration diameter, and saves a lot of time as the number of equations to be solved are reduced compared to sectional or method of moments. Hence, the soot aggregation in this study will be assumed to take place starting from a primary particle diameter of 2 nm [151].

The mechanism of soot aggregation is similar to coagulation as both the processes are due to the Brownian collision of the particles. Hence, soot aggregation rates are also determined using the collision theory applied for coagulation, however, with collision frequencies reflecting the aggregation phenomenon [132]. The fractal soot structure is usually analyzed by a fractal dimension. Kazakov and Frenklach [147] proposed a collision-based soot aggregation model similar to coagulation, however with collision frequencies reflecting the fractal structures. A fractal dimension, representing particle morphology, of 1.8 was assumed by the authors in their study. Generall, a fractal dimension of 1 represents chain type particles, whereas a value of 3 corresponds to a densely packed structure. Saggase et al. [149] used a similar approach to model soot aggregation using a soot fractal dimension of 1.8. The values of the frequency factor implemented were similar to the values proposed by Sirignano et al. [150]. The model implemented in reference [151] will be used to quantify soot aggregation in the present study.

Soot surface growth

The dynamics of soot growth are also impacted by surface reactions, where the soot particles react with the gas phase species and grow in size. The hydrogen abstraction and carbon addition (HACA) model is generally used to mimic the interaction between the solid and gas phase [131, 152]. The continuous attack of acetylene molecules on the surface of soot particles leads to a formation of an adjacent aromatic ring and an increase in the overall size of the particles. The surface growth rate is highly dependent on the number of active sites available for acetylene to attack and the acetylene

concentration. The number of active sites were found to be dependent on the chemical environment by Frenklach and Wang [152]. On the other hand, the dependence of surface growth rate on the acetylene concentration has been observed [153]. In references [143, 154], the reaction responsible for surface growth was assumed to be first order and its implementation in a HACA model provided results that matched experiments. Another model representing the surface growth mechanism, similar to HACA, was proposed by Zhang et al. [155, 156]. The authors used density functional theory to predict surface growth and concluded that surface growth happens through carbon addition and hydrogen migration (CAHM) at temperatures below 1500 K. This claim, however, was recently questioned by Frenklach et al. [157]. He used the post-flame conditions studied by Oktem et al. [138] and compared the growth rates from CAHM and HACA. The growth rate obtained from the HACA model was found to dominate at the low temperature range of 1000–1500 K. Hence, the HACA assisted surface growth model will be used in the present study.

Numerical models

The above-mentioned submodels can be combined to develop a comprehensive soot formation model as shown in Figure 1.3. Particle number and size distribution are important aspects of quantifying soot formation. The size distribution plays an important role in determining the type of industry it can be used in. Experimentally understanding this is tiring and expensive. However, numerically it is less costly and can provide much detailed information about the different phenomena contributing to the size growth of particles. So, this is why it is important to understand the particle size distribution and number density. A limited number of models have implemented these soot sub-mechanisms while investigating soot formation during methane pyrolysis. Fincke et al. [85] studied soot formation during plasma pyrolysis of methane at 3450 K and proposed a soot formation mechanism. A simplified first order single nucleation step was used where benzene decomposes to solid carbon and

hydrogen. Due to this assumption, only solid carbon was modeled which does not reflect the actual case during characterization of a soot particle. Some amount of hydrogen is always present in the soot particles which the model was not able to account for. A simplified mechanism cannot predict the particle size distribution of soot particles.

Patrianakos et al. [80] developed an in-house one dimensional model to study soot formation during methane pyrolysis in a flow reactor. The model solved for soot nucleation, coagulation and surface growth to track particle size distribution and was validated against the experimental data from a prototype reactor used in references [78, 158]. However, soot aggregation was not addressed and a single step reaction for methane decomposition was assumed by the authors.

Keramiotis et al. [159] used a flow reactor in the temperature range 1250–1500 K to study the formation of soot for different initial methane mixtures. Residence time of 3–3.6 s was used and experiments were performed for nearly 1–3 h in order to collect considerable amount of soot at the reactor outlet. The amount of soot collected was found to be proportional to fuel consumption. The authors used two different reaction mechanisms to numerically predict the intermediates and found considerable discrepancies in hydrogen prediction (up to 30%) at higher temperatures. The discrepancies were attributed to the absence of the paths in the mechanism leading to the formation of additional hydrogen.

Agafonov et al. [133] used a kinetic scheme containing 260 species and 2500 elementary reactions to track the time–dependent soot yield and particle temperature. PAH formation and growth through different reactions up to coronene ($C_{24}H_{12}$) were included in the model. A mechanism of soot formation, surface growth, coagulation, oxidation and transformation of soot precursor and soot particle was proposed. The authors found discrepancies in the surface growth mechanism and concluded that further studies are required to address it. In another study, Agafonov et al. [160] proposed a kinetic model of soot formation and tested it for different inlet fuels, including

methane, in the temperature and pressure range of 1852–2212 K and 3–5.44 bar, respectively. However, the model did not include soot growth due to aggregation which plays a vital role beyond a certain size.

Based on the discussion above, it can be concluded that none of the studies have included all the aspects of soot formation, such as soot aggregation, while specifically modeling methane pyrolysis in the temperature range of 1000–1400 K. The most detailed models [133, 160] simulated soot formation in shock tubes at higher temperatures (> 1500 K) and short residence times (< 1 s). Low temperature methane pyrolysis forms more intermediates as compared to higher temperatures. Hence, it is hypothesized that accurate predictions of soot formation during methane pyrolysis needs a more detailed soot model. The third objective of this thesis is to develop a soot formation model to track the soot formation during low temperature methane pyrolysis. A framework implementing all the sub-models, such as soot nucleation, soot aggregation, and soot surface growth, given in reference [151] will be developed. The proposed model will be used to understand different pathways, if any, through which soot can nucleate at low temperature conditions. Additionally, the proposed soot model will be used to quantify the amount of soot produced during the process and the particle size distribution.

1.2.8 Reactor design

Detailed understanding of methane pyrolysis kinetics is not sufficient to provide recommendations for reactor design unless a reactor model is available that can cumulatively describe the important elements of the process, and identify those hindering its optimal performance over time and/or space under varying operating conditions. These elements have been addressed by the use of two main reactors stated in the literature: batch reactors [31–33] and plug flow reactors (PFR) [35, 56, 76]. A batch reactor is a closed system where reactants breakdown under the influence of heat and convert to products. Continuous conversion of reactants is not favourable in a batch

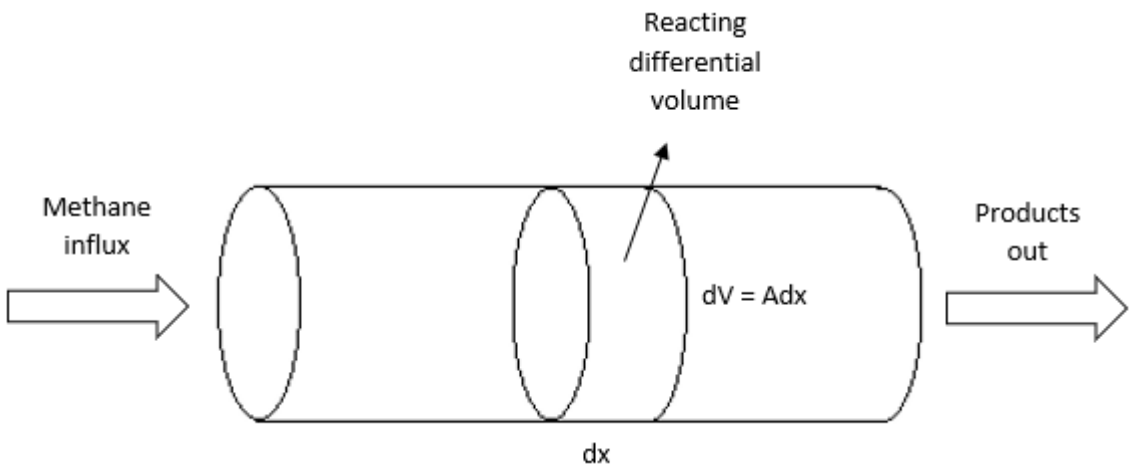

Figure 1.4: Basic outline of a plug flow reactor.

reactor, thus limiting its industrial application. A PFR, on the other hand, is an open system allowing for continuous flow of reactants converting to products and is thus preferred over a batch reactor for industrial use. A basic schematic of a PFR used in the present study for a methane pyrolysis process is shown in Figure 1.4. During the process, gaseous methane enters the heated reactor, decomposes to different products, such as H_2, C_2H_2, C_2H_4, C_2H_6, and soot, and these are then collected at the outlet. An accurate reactor model should be capable of predicting the amount of these species at a given reactor temperature, pressure, gas flow rate, and for a defined geometry. In a pyrolysis reactor, the following physical processes take place: a) gas mass and momentum conservation and reaction; b) energy conservation and reaction; and c) soot formation and evolution, coupled with gas phase. An accurate model ideally would describe all these processes at the same time. These processes are, hence, reviewed in the following paragraphs in the form of kinetic, thermal, and fluid flow effects and the important phenomena critical to the reactor design are identified.

A number of kinetic reactor models have been proposed in references [25, 34, 62, 72, 75, 158]. The reaction kinetics in these studies were solved using a single–step reaction mechanism. Therefore, these reactor models cannot predict the intermediate species formation and consumption during a reaction. This is important in the temperature

range of 1000–1400 K when the intermediates formation is favourable. The formation of soot in solid phase has been addressed assuming a single carbon black species, whereas, it has been observed in different studies [25, 78, 133] that soot particles of varied size are generated in a fuel rich condition [161]. Hence, the application of simple kinetic reactor models will not provide accurate results and detailed models explaining intermediates in gas and solid phase are required.

Some reactor model studies have looked at complex kinetic details of methane pyrolysis. For example, Rodat et al. [78] developed a 1D tubular solar reactor model using Dsmoke software in the temperature range 1500–2300 K to quantify methane conversion. The model over-predicted methane conversion when validated against the experimental data. This discrepancy was attributed to the shortcomings in the software model where heterogeneous reactions due to the carbon particles were not accounted for. In addition to the gas phase reactor models, some detailed solid phase models have also been implemented [80, 162]. However, some aspects of soot modeling were kept simple, such as assuming a spherical particle shape of a soot aggregate [80]. The validity of this assumption is not justified considering the chain-like shape of the soot aggregates and thus may lead to discrepancies in the soot predictions [161]. It can be seen that none of the proposed reactor models are capable of explicitly providing detailed insights into the inherent kinetic phenomenon of a methane pyrolysis process both in gas and solid phase. The current study will address this issue and a detailed kinetic reactor model will be developed coupling both gas and solid phase.

A thermal model solves for the energy equation and affects the reactor kinetics, by altering the residence time, depending on the temperature, and thus can amend the model predictions. Reactor models have been either considered isothermal [25, 38, 56, 78] or non-isothermal [73, 74, 76, 80]. In non-isothermal models, thermal effects are implemented with the help of the energy equation consisting of different heat transfer mechanisms, such as energy from the reaction, conduction, convection and radiation heat transfer between the reactor wall, gas and solid particles. Dahl

et al. [73] developed a 1D aerosol flow reactor model which solved for the energy consumed by the reaction, convection from reactor walls to gas, radiation heat transfer from reactor walls to particles and energy transfer between the gas and solid particles in the temperature span of 1533–2144 K for short residence times (0.9–1.5 s). At low flow rates, methane conversion was mainly observed around the inlet of the reactor where the temperature was the highest. At higher flow rates, a more uniform temperature profile was observed and the conversion of methane occurred over the whole length of the reactor. Abanades and Flamant [76] developed a 1D reactor model using the methodology adopted by Dahl et al. [73] in the temperature range 1563–1813 K. Methane conversion was found to depend on the endothermicity of the reaction when the percentage of methane in the inlet mixture was more than 20%. Additionally, due to the variable temperature profile at the inlet and outlet in their case, only a narrow part around the centre of the reactor length remained at the working temperature and the majority of the methane decomposition was observed around that region. Wyss et al. [74] considered a number of thermal effects, such as energy consumed by the reaction, radiation absorbed by the carbon particle and convection heat transfer in a 1D model of a PFR at 2000 K and 10 ms residence time. As the convection and radiation heat transfer rates were increased in the model, a shift in methane decomposition towards the entrance of the reactor was observed. Patrianakos et al. [80] developed a 1D flow reactor model accounting for wall–gas convection, wall–particle radiation, gas–particle convection and heat released from the reaction. Their reactor model showed that thermal entry lengths were negligible compared to the whole reactor length. The main goal of this thesis is to develop an accurate methane pyrolysis kinetics model and the physical reactor will be designed in the in-house facility at the University of Alberta. To simplify the requirements for the model, the reactant gas will be diluted with a noble gas to reduce the temperature change due to endothermicity of the reaction. Secondly, the reactor will be horizontally oriented to avoid the temperature-induced buoyancy and will remain inside a furnace so that the gases

are at the operating temperature. This will also minimize the thermal entry lengths observed by Patrianakos et al. [80]. Based on these assumptions, an isothermal reactor condition will be considered in the present study and energy equation will not be solved.

Inclusion of a fluid flow equation in the model allows for the prediction of the fluid flow profile in the reactor and any additional effects, such as temperature–induced buoyancy. Fluid flow in the reactor is usually modeled by solving a Navier–Stokes equation along with the kinetics. Homayonifar et al. [79] observed acceleration in fluid velocity near the walls in a vertically oriented reactor due to strong buoyancy effects. Additionally, the model predicted that the mean velocity of the gas mixture at the reactor outlet was 4 times the mean velocity at the inlet due to the generation of 2 moles of product gas per mole of reactant decomposed. Caliot et al. [162] developed a laminar 2D tubular flow reactor model solving for flow dynamics using the Navier-Stokes equation, heat transport in the combined gas and particle flow and radiative heat transfer between the methane and the carbon particles using the energy conservation, and species transport using advection–diffusion equation in a cylindrical geometry. A reaction boundary layer was observed in the reactor which resulted in the change in the local particle size distribution across the reactor. The model validation against the experimental data was not performed. Abanades and Flamant [77] developed a laminar 2D reactor model to address the fluid flow characteristics, heat and mass transfer during methane decomposition using the CFD Fluent software. Gas velocity and temperature profiles were found to inherently depend on the gas axial and radial positions inside the reactor. A large variation in the radial and axial temperature led to an underprediction in methane conversions and hydrogen yield compared to the experimental data. Additionally, neglecting heterogeneous reactions due to carbon particles further contributed to the variations in the model and the experimental observations.

From the discussion, it can be seen that the thermal and fluid flow sub-models

affect methane decomposition kinetics. However, except in references [77, 79, 162], the majority of the reactor models [25, 34, 62, 72, 73, 75, 76, 78, 158] did not include a detailed fluid flow sub-model as the operating conditions reflected homogeneous conditions across the section of a reactor and, therefore, a plug flow reactor was considered.

Based on the literature review, NUIGMech 1.1 [90] will be used for further analysis at relevant experimental conditions. Then, DRGEP method will be used to develop a skeletal mechanism. The rate parameters of the reduced/skeletal mechanism will then be fitted to experimental data for methane and hydrogen in the temperature range 892–1292 K and 398.8 kPa as given in reference [1], as these contain all critical features at low and high temperature and high pressure, using coliny pattern search method [163]. The optimized mechanism will be implemented in batch and plug flow reactor models in Cantera [124]. Finally, to analyze soot formation, the model from reference [151] will be integrated into Cantera [124] and the particle morphology will be predicted. Additionally, a steady state isothermal 1D PFR model with detailed methane pyrolysis kinetics will be developed that takes both gas and solid phase products into account in the temperature range 1000–1400 K. The detailed reactor model can then be used to determine the optimum conditions, such as temperature and pressure, for an industrial specific methane pyrolysis application, such as hydrogen production, or size-specific soot production as described in Section 1.2.7.

1.3 Thesis Objectives

- To test the kinetic models available in the literature and compare the model predictions against the data available in the literature at high-pressures.
- To develop a mechanism reduction framework for pyrolysis conditions and obtain a skeletal model suitable for low and high-pressure methane pyrolysis.
- To optimize the reduced kinetic model, based on a proposed mechanism from

literature with kinetic parameters obtained by least-square optimization of experimental data and study the change in the reaction pathways responsible for driving up methane decomposition.

- To implement a monodisperse population balance soot model based on the model proposed in the literature, couple it with the gas-phase model, and predict the transient evolution of the soot generated and its morphology.

- To develop a 1D plug flow reactor model with coupled gas and solid phase, and to use it to obtain the optimum conditions, such as temperature, pressure and residence time, for the production of hydrogen and soot.

Chapter 2

Methodology[1]

The present chapter discusses the methodology for the models implemented and their requirement for methane pyrolysis. Section 2.1.1 discusses the methodology for the gas-phase model to quantify the amount of methane converted to other products and helps in identifying the critical rate-determining step by quantifying the reaction rate for each elementary reaction. As the current study's aim was high-pressure methane pyrolysis where a lot of carbon black was generated, a sink term accounting for carbon formation was needed in the gas-phase model and is described in Section 2.1.2. A kinetic model selection study was performed to identify a mechanism that can closely track the high-pressure decomposition data while incorporating the pressure dependency and the selection criteria is given in Section 2.2. Once the model was selected, the model predictions for the amount of methane, hydrogen, and solid carbon formation were tested against the equilibrium calculations to make sure the values are below the theoretically possible. Hence, an equilibrium model was used to identify the product compositions considering methane, hydrogen, and carbon in

[1]Parts of this chapter are reproduced from the following publications:

1. A Punia *et al.*, "Analysis of methane pyrolysis experiments at high pressure using available reactor models," *Chemical Engineering Journal*, p. 144 183, 2023.
2. J. Tatum *et al.*, "Dataset of methane pyrolysis products in a batch reactor as a function of time at high temperatures and pressures," *Data in Brief*, vol. 47, p. 108 953, 2023.
3. A. Punia *et al.*, "A reduced methane pyrolysis mechanism for above-atmospheric pressure conditions," *Chemical Engineering Journal*, vol. (Under review),

Author contributions are detailed in the Preface of this thesis.

the system. The methodology for the equilibrium theory and implementation are discussed in Section 2.2.1. As the model selected contained a large number of species and reactions, using such a model for optimization required dealing with a large number of design variables. Additionally, using such a mechanism for CFD simulations or for soot formation requiring significantly small step-sizes would have imposed a tremendous computational load. Hence, a kinetic model reduction framework was developed, as discussed in Section 2.2.2 and the detailed kinetic model was reduced to an acceptable level. The reduced model had inaccuracies associated with it due to removal of species and reactions from the mechanism. Hence, a parameter estimation framework was developed and the kinetic rate parameters of the reduced model were fitted against the high-pressure data available in the literature. Section 2.2.3 discusses the methodology behind the optimization framework. To investigate how additional reaction pathways become active and to understand the role of different species for their contribution to driving up methane decomposition before and after the rate parameter optimization, a reaction pathway analysis was performed. The methodology for the reaction pathway analysis is discussed in Section 2.2.4. The initial assumption of acetylene decomposition to carbon black was not accurate as the other particle physics, such as soot aggregation and surface growth, play an important role in particle evolution over time. Hence, a monodisperse soot formation model was needed and implemented using the model proposed by Kholghy et al [151] to predict the particle characteristics over time and described in Section 2.2.5.

2.1 Pyrolysis reactor model

2.1.1 Gas-phase model

The experimental reactor was simulated using a constant-volume batch reactor. The reaction mechanisms considered were introduced in a zero-dimensional, closed, isochoric, homogeneous gas-phase model, to mimic the conditions in the batch reactor

type used in the experimental work in references [1, 2, 31, 33]. The reactor model is governed by the following mass conservation equation,

$$\frac{\mathrm{d}(mY_i)}{\mathrm{d}t} = VS_iM_i \tag{2.1.1}$$

where Y_i is the mass fraction of the i^{th} gaseous species inside the reactor, V is the reactor volume (m^3), M_i is the molar mass of species i (kg/mol), m is the total mass inside the reactor (kg), and S_i is the production or consumption rate of species i (mol/(m^3 s)), which depends on the kinetic mechanism and is given by

$$S_i = \sum_{j=1}^{J} \upsilon_{ij} r_j \tag{2.1.2}$$

where r_j is the kinetic reaction rate for the j^{th} elementary reaction and υ_{ij} is the stoichiometric coefficient of the i^{th} species in the j^{th} elementary reaction.

The kinetic reaction rate for the j^{th} elementary reaction, r_j, is estimated using

$$r_j = k_{\mathrm{f},j} \prod_{r=1}^{R} C_r^{\upsilon_{rj}} - k_{\mathrm{b},j} \prod_{p=1}^{P} C_p^{\upsilon_{pj}} \tag{2.1.3}$$

where R and P are the total number of reactant and product species in the j^{th} elementary reaction, respectively, C_i is the i^{th} species concentration (in mol/m^3) given by $C_i = \frac{mY_i}{VM_i}$, $k_{\mathrm{f},j}$ is the forward reaction rate constant for the j^{th} elementary reaction and is given by

$$k_{\mathrm{f},j} = A_j T^{n_j} \exp\left(\frac{-E_{\mathrm{a},j}}{R_{\mathrm{u}} T}\right) \tag{2.1.4}$$

and the backward reaction rate constant, $k_{\mathrm{b},j}$, is computed using the expression

$$k_{\mathrm{b},j} = \frac{k_{\mathrm{f},j}}{K_{\mathrm{eq},j}} \tag{2.1.5}$$

where A_j, n_j and $E_{\mathrm{a},j}$ are the pre-exponential factor, temperature exponent and the activation energy, respectively, for the j^{th} forward elementary reaction and are expressed by the Arrhenius equation, and $K_{\mathrm{eq},j}$ is the equilibrium constant for the j^{th} elementary reaction and is calculated using the standard Gibbs free energy change

expression. To account for pressure dependence, the calculation of forward rates included a pressure dependency which was different depending on the type of reaction, e.g., fall-off, three-body, and pressure-dependent-Arrhenius reaction [124]. The rate constant for the fall-off reaction was given by Lindermann et al. [164]

$$k_{f,j} = \frac{k_0[M]}{1 + \frac{k_0[M]}{k_\infty}} \tag{2.1.6}$$

$$P_r = \frac{k_0[M]}{k_\infty} \tag{2.1.7}$$

where k_0 is the rate constant calculated using the low-pressure rate parameters, k_∞ is the rate constant calculated using the high-pressure rate parameters, $[M]$ is the concentration of the third body specified in the reaction mechanism input file, P_r is the reduced pressure. In the low-pressure limit, the concentration of the third body goes to zero, and the expression approaches $k_0[M]$, whereas, in the high-pressure limit, the concentration of the third body goes to infinity and the expression reduces to k_∞. The rate constant can be rewritten as

$$k_{f,j} = k_\infty \left(\frac{P_r}{1 + P_r} \right) \tag{2.1.8}$$

An improved version of the rate constant expression proposed by Gilbert et al. [165], called the Troe fall-off function, was used. In the Troe fall-off function, the Lindermann expression, given in equation (2.1.8), is multiplied by a fall-off function, $F(T,P_r)$ depending on the temperature and the reduced pressure

$$k_{f,j} = k_\infty \left(\frac{P_r}{1 + P_r} \right) F(T, P_r) \tag{2.1.9}$$

$$\log_{10} F(T, P_r) = \frac{\log_{10} F_{cent}(T)}{1 + f_1^2} \tag{2.1.10}$$

$$F_{cent}(T) = (1 - A_j) \exp(\frac{-T}{T_3}) + A_j \exp(\frac{-T}{T_1}) + \exp(\frac{-T_2}{T}) \tag{2.1.11}$$

$$\digamma_1 = \frac{\log_{10} P_r + \hat{C}}{N - 0.14(\log_{10} P_r + \hat{C})} \tag{2.1.12}$$

$$\hat{C} = -0.4 - 0.67 \log_{10} F_{cent} \tag{2.1.13}$$

$$N = 0.75 - 1.27 \log_{10} F_{cent} \tag{2.1.14}$$

The rate constant for the pressure-dependent is given by a logarithmic interpolation between the Arrhenius rate values at different pressures. For an intermediate pressure, P, such that $P_1 < P < P_2$, the rate will be calculated as

$$\log k_{f,j}^{P}(T) = \log k_{f,j}^{P_1}(T) + (\log k_{f,j}^{P_2}(T) - \log k_{f,j}^{P_1}(T)) \frac{\log P - \log P_1}{\log P_2 - \log P_1} \tag{2.1.15}$$

where $\log k_{f,j}^{P_1}(T)$ and $\log k_{f,j}^{P_2}(T)$ are the rate constant values for jth reaction at pressures, P_1 and P_2, respectively. If multiple rate parameters were available at the same pressure, the sum of all the rate constant values was obtained before performing the logarithmic interpolation. Finally, in the case of reactor operating pressure outside the specified range in the input file, the rate parameters corresponding to the nearest pressure were used.

Equation (2.1.1) for each species results in a set of ordinary differential equations. The system of equations was solved using the open-source software package Cantera [124]. The package calculates the thermodynamic properties of different species using a given reaction mechanism file. To solve the system of equations, a 5th-order backward differentiation formula (BDF–5) with a Newton solver was used. Relative and absolute error tolerances of 10^{-9} and 10^{-15}, respectively, are required to achieve solver convergence.

2.1.2 Carbon formation model

Solid carbon formation was accounted for by modifying the governing equations in the gas phase discussed in Section 2.1.1 to account for mass loss from the gas mixture [166]. To model solid carbon, acetylene converting to carbon and hydrogen was considered as the irreversible reaction as given in reference [1],

$$\mathrm{C_2H_2(g)} \longrightarrow \mathrm{H_2(g)} + 2\,\mathrm{C(s)}, \qquad [5e13\ 1/s, 0, 410\ \mathrm{kJ/mol}] \tag{2.1.16}$$

Due to the addition of the carbon-forming reaction in the mechanism, the production rates of acetylene and hydrogen were modified and were given by

$$\frac{\mathrm{d}(mY_{\mathrm{C_2H_2}})}{\mathrm{d}t} = (S_{\mathrm{C_2H_2}} - r_{j,c})VM_{\mathrm{C_2H_2}} \tag{2.1.17}$$

$$\frac{\mathrm{d}(mY_{\mathrm{H_2}})}{\mathrm{d}t} = (S_{\mathrm{H_2}} + r_{j,c})VM_{\mathrm{H_2}} \tag{2.1.18}$$

Finally, carbon formed from acetylene was given by the following equation:

$$\frac{\mathrm{d}(mY_{\mathrm{C}})}{\mathrm{d}t} = 2r_{j,c}VM_{\mathrm{C}} \tag{2.1.19}$$

where $r_{j,c}$ is the reaction rate for the carbon-forming reaction given in equation (2.1.16) and is given by

$$r_{j,c} = k_f C_{\mathrm{C_2H_2}} \tag{2.1.20}$$

where k_f is the forward rate constant for the reaction (1/s) evaluated using equation (2.1.4), and $[C_{\mathrm{C_2H_2}}]$ is acetylene concentration (mol/m^3).

The absolute pressure change due to hydrogen gas production from acetylene was accounted for by using the ideal gas law. A variable coefficient ordinary differential equation solver (VODE) was used with a 5th-order backward differentiation formulae

(BDF) method to solve the system of equations. The method-specific parameters were the same as discussed in the previous section.

The reaction models were tested for low-pressure operating conditions, i.e., 10–100 kPa without carbon formation, whereas for high-pressure conditions, i.e., at 398.8 kPa carbon formation model was included based on the batch reactor experiments done in references [1, 2, 31–33, 45].

2.2 Kinetic model analysis

Several reaction mechanisms proposed for methane pyrolysis were used to study the reaction kinetics at sub- and above-atmospheric pressure operating conditions. While selecting a reaction mechanism, special attention was paid to including reaction rate parameters to account for the change in the rate expressions due to pressure variations, such as fall-off reactions, three-body reactions, and pressure-dependent reactions. The following mechanisms were used in this study: a) GRIMECH 3.0 [82] mechanism (53 species and 325 reactions), b) AramcoMech 3.0 [83] mechanism (135 species and 532 reactions), c) NUIGMech 1.1 [90] mechanism (325 species and 1516 reactions), d) Ranzi et al. [87] mechanism (50 species and 652 reactions to track the major and minor decomposition products); and, e) Appel et al. [69] mechanism (75 species and 242 reactions aimed at tracking C_1–C_{16} species). Note that the reaction mechanisms proposed in references [36, 78, 91] were specifically focused to track hydrogen during methane pyrolysis and the ones proposed in references [29, 64] were not available. Hence, these mechanisms were not used in the present study.

2.2.1 Thermodynamic analysis

Chemical equilibrium is the state in which both the reactants and products are present in concentrations that do not change with time. The state is reached when the net forward reaction rate is equal to the net backward reaction rate. Under these circumstances, our goal is to find a composition that minimizes the total Gibbs free

Table 2.1: Reaction mechanisms used for MTD.

References	**Species**	**Reactions**	**Range**
NUIGMech 1.1 [90]	325	1516	C_1 – C_{16}
GRIMECH 3.0 [82]	16	45	C_1 – C_3
AramcoMech 3.0 [83]	135	532	C_1 – C_{16}
Ranzi et al. [87]	50	652	C_1 – C_{10}
Appel et al. [69]	75	242	C_1 – C_{16}

energy of the mixture, subject to element conservation constraints. We know that the Gibbs free energy can be written as a function of temperature, pressure and the mixture composition as follows:

$$G = G(T, P, N_i) \tag{2.2.1}$$

where G is the total Gibbs energy of the mixture, T is the temperature, P is the pressure, and, N_i is the number of moles for each species in the mixture. Taking a partial derivative of the total Gibbs energy function with respect to the independent variables, we get

$$\mathrm{d}G = \left(\frac{\partial G}{\partial T}\right)_{P,N_i} \mathrm{d}T + \left(\frac{\partial G}{\partial P}\right)_{T,N_i} \mathrm{d}P + \sum_{i=1}^{N_{\text{species}}} \left(\frac{\partial G}{\partial N_i}\right)_{T,P,N_{j\neq i}} \mathrm{d}N_i \tag{2.2.2}$$

where N_{species} is the total number of species in the system and j corresponds to the species other than i. Correlating the above partial differential terms with the state function sets, such as total internal energy U and total enthalpy H, we find that the above equation can be written in the following complete differential equation:

$$\mathrm{d}G = -S\mathrm{d}T + V\mathrm{d}T + \sum_{i=1}^{N_{\text{species}}} \mu_i \mathrm{d}N_i \tag{2.2.3}$$

where V is the volume, and μ_i the chemical potential of the ith species and is defined by

$$\mu_i = \left(\frac{\partial G}{\partial N_i}\right)_{T,P,N_{j\neq i}} \tag{2.2.4}$$

or, for an ideal gas,

$$\mu_i = \mu_i^{\circ} + RT \ln p_i \tag{2.2.5}$$

in which the pressure P is replaced by the partial pressure p_i, where, by definition,

$$p_i = \left(\frac{N_i}{N_t}\right) P \equiv X_i P \tag{2.2.6}$$

where X_i is the mole fraction of species i, and N_t is the total number of moles in the solution. Equation (2.2.5) for the chemical potential is valid for ideal-gas solution and can be further written as

$$\mu_i = \mu_i^{\circ} + RT \ln P + RT \ln X_i \tag{2.2.7}$$

Equation (2.2.7) may be used for an ideal solution, which may be gaseous, liquid, or solid. This is accomplished in part by replacing the first two terms on the right by an arbitrary function of T, P, and a standard compositional state X_i^*, $\mu_i(T, P, X_i^*)$, such that

$$\mu_i(T, P, X_i) = \mu_i(T, P, X_i^*) + RT \ln X_i \tag{2.2.8}$$

For a chemical reaction to be in equilibrium, the chemical potential of the products is equal to that of the reactants.

$$\mu_{\text{prod}} = \mu_{\text{reac}} \tag{2.2.9}$$

At equilibrium, the change in the total Gibbs energy is zero,

$$\mathrm{d}G|_{P,T} = 0 \tag{2.2.10}$$

If we take a case for multiple species in a mixture at a constant temperature and pressure, the first two terms on the RHS of Equation (2.2.3) become zero and the equation reduces to

$$\mathrm{d}G|_{P,T} = 0 = \sum_{i=1}^{N_{\text{species}}} \mu_i \mathrm{d}N_i = \sum_{i=1}^{N_{\text{species}}} \mu_i \nu_i \tag{2.2.11}$$

where ν_i is the reaction stoichiometry.

Given the equation above, together with the condition that the sum of the mole fractions is unity, and the known quantities of each atomic constituent in the system at the initial state, the mole fraction of each species can be obtained.

The final system of equations for an equilibrium mixture is numerically solved in Cantera using different solvers, such as the Villars-Cruise-Smith (VCS) algorithm. The solver is designed to be used to set a mixture containing one or more phases to a state of chemical equilibrium. For more information on the algorithm see Chapter 6 in 'Chemical reaction equilibrium analysis theory and algorithms' by Smith and Missen [167].

2.2.2 Model reduction

Once the model was selected, a reaction mechanism reduction was performed to simplify the decomposition chemistry while maintaining the pressure-dependent nature of the mechanism. The model derived reduces the computational requirements of the kinetic model making it easier to perform parameter estimation and to implement in CFD reactor models. Kinetic model reduction was performed using a modified directed-relation graph with error propagation (DRGEP) [168], a graph-based method, using pyMARS software [169]. The method establishes the dependence of the global or target quantities of interest, such as species mole fractions, flame velocity, or ignition delay times, on other species in the detailed mechanism by evaluating an importance coefficient. Figure 2.1 shows the algorithm of the DRGEP-based model reduction. The importance coefficient, f_{AB}, establishing the dependence of target

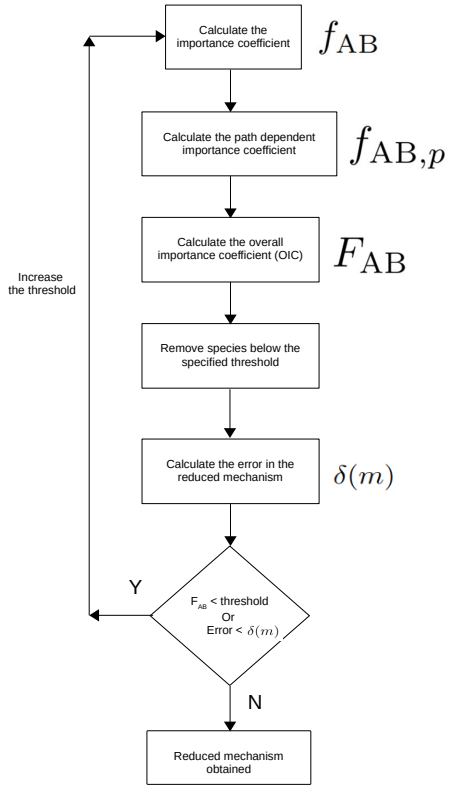

Figure 2.1: Schematic of the DRGEP-based model reduction.

species A on species B in the reaction mechanism is given by the following expression [169]

$$f_{\mathrm{AB}} = \frac{|\sum_{j=1}^{J} \upsilon_{\mathrm{A},j} r_j \delta_{\mathrm{B}}^{j}|}{\max(Q_{\mathrm{A}}, L_{\mathrm{A}})} \tag{2.2.12}$$

where

$$Q_{\mathrm{A}} = \sum_{j=1}^{J} \max(0, \upsilon_{\mathrm{A},j} r_j) \tag{2.2.13}$$

$$L_{\mathrm{A}} = \sum_{j=1}^{J} \max(0, -\upsilon_{\mathrm{A},j} r_j) \tag{2.2.14}$$

$$\delta_{\mathrm{B}}^{j} = \begin{cases} 1 & \text{if the } j\text{th elementary reaction} \\ & \text{involves species B,} \\ 0 & \text{otherwise.} \end{cases}$$

where $\upsilon_{\mathrm{A},j}$ is the stoichiometric coefficient of species A in the j^{th} elementary reaction, and r_j is given by equation (2.1.3). After evaluating the importance coefficient, f_{AB}, a modified form of Dijkstra's algorithm [170, 171] was used to identify the path-specific target species' dependency on the remaining species in the reaction mechanism. For each path p, the dependency of the target species A on species B was quantified based on a path-dependent importance coefficient, $f_{\mathrm{AB},p}$, that represented the error propagated due to the removal of species B and was given by

$$f_{\mathrm{AB},p} = \prod_{i=1}^{H-1} f_{U_i U_{i+1}} \tag{2.2.15}$$

where H is the number of species from A to B in the pathway p, and U is an intermediate species starting at A and ending at B. To take into account the error propagated from all the paths, a maximum overall importance coefficient (OIC) was defined as the maximum of all path-dependent importance coefficients between the target and other species in the reaction mechanism

$$F_{\mathrm{AB}} = \max_{\mathrm{p}}(f_{\mathrm{AB},p}) \tag{2.2.16}$$

The OIC for each target species pair was used such that the target species was assigned a single overall importance coefficient for the reactor thermodynamic condition (sample point) under consideration. For each sample point, an OIC value was obtained for the target species pair, and the maximum OIC value among all the sample points was selected. Species with maximum OICs below a user-specified threshold value of 0.2 were not considered to contribute significantly to the overall production/-consumption rates of the target species for the given sample points and; therefore, were removed from the reaction mechanism.

The reduced/skeletal mechanism predictions were tested against the original mechanism predictions, and a relative error bound of 30% or was set. If the error in the reduced mechanism or the OIC value reached the user-specified value of 30% or 0.2, respectively, the simulation was terminated. The error value was obtained by trial and error. A value bigger than 30% generated a mechanism where the accuracy in target species was compromised. If a smaller value than 30% was used, the chemistry became detailed and the reduction was redundant. The error, $\delta(g)$, in the reduced mechanism, was calculated using the global quantity of interest or the target species and was given by the expression

$$\delta(g) = 100 * \max_{i=1}^{I_{\mathrm{tar}}} \left\{ \sqrt{\frac{\sum_{g=1}^{G} \left(\frac{X_i^{\mathrm{original}} - X_i^{\mathrm{reduced}}}{X_i^{\mathrm{original}}} \right)_{g,i}^2}{G-1}} \right\} \tag{2.2.17}$$

where I_{tar} is the total number of target species, G is the number of equally spaced temporal points for each species (20 in this work), X_i^{original} is the target species concentration obtained using the original mechanism at the g^{th} temporal node, and X_i^{reduced} is the target species concentration obtained using the reduced mechanism at the g^{th} temporal node. The threshold value from the start of the reduction simulation was

iteratively increased with an initially low value of 0.01. If the error, given in equation (2.2.17), for the initially reduced mechanism, was above the user-specified limit, the threshold was decreased by a factor of 10 until a value of 10^{-6} was reached. If the error was below the user-specified error limit, the threshold was increased, until the error reached the specified limit or the threshold value reaches the user specified value. A threshold value of 0.2 was provided in the present study..

Since the aim of the DRGEP-based mechanism reduction is to retain the model at low-pressure and estimate parameters at high pressure that could be used in the detailed model, both conditions were used in the model reduction. A total of 25 sampling conditions, given in Table 2.2, were used to sample the thermochemical data covering the thermodynamic range of 1000–1400 K and 0.1–4 atm. The residence time for each sampling condition was based on the experimental operating conditions in the literature [31, 32]. Under the set of sample operating conditions chosen for the reduction, the global quantities of interest were CH_4, H_2, C_2H_4, C_2H_6, C_2H_2, α-C_3H_4, and p-C_3H_4 mole fractions. CH_4, H_2, C_2H_4, C_2H_6, and C_2H_2 were chosen based on the fact that these species were observed during the experiments. Additionally, α-C_3H_4, and p-C_3H_4 were selected as C_2's accuracy depends on them.

The pyMARS [169], a python based open-source package for automatic reduction of kinetic models was initially proposed to reduce combustion-based mechanisms. Pyrolysis functionality was added in this work. The framework takes in the reactor operating conditions, samples the thermochemical data, and runs the 0D isothermal, isochoric, and adiabatic batch reactor using Cantera [124] as described in Section 2.1.1. Then, it uses this information to remove the unnecessary species and reactions from the detailed mechanism. The error in the global quantities of interest is used as stoppage criteria. Once the mechanism reduction simulation is completed, species and reaction reduction ratios are obtained using the following equation

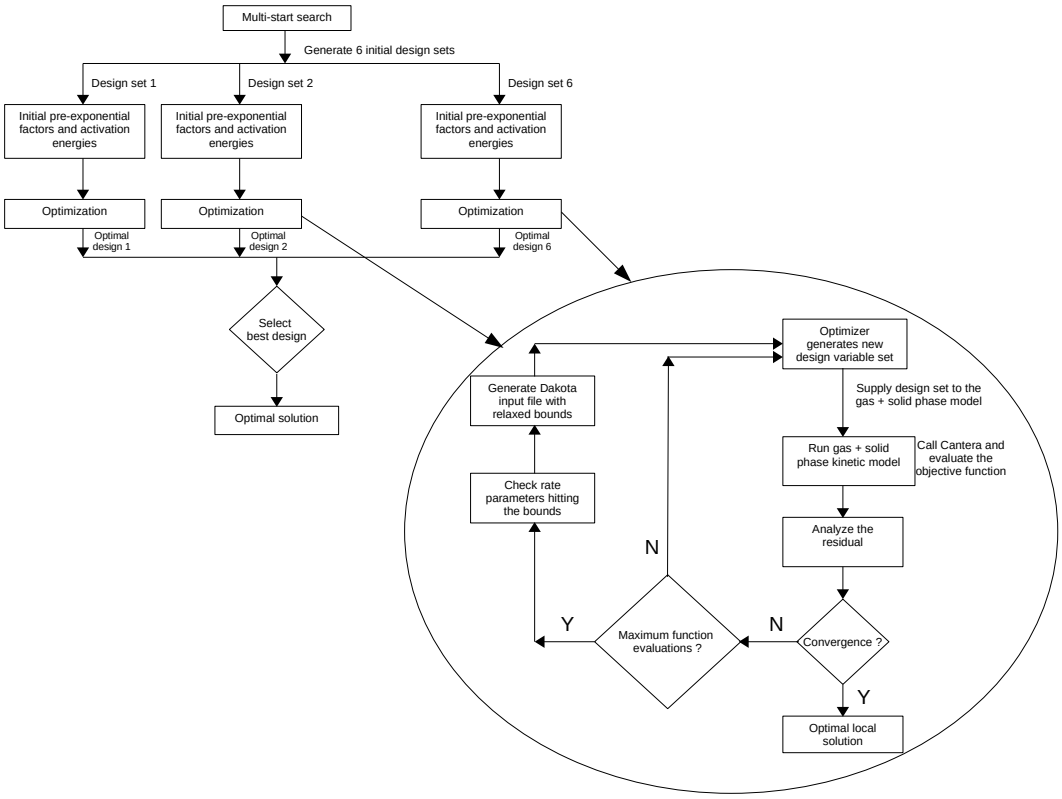

Figure 2.2: Schematic of the algorithm used to obtain the optimized values of the pre-exponential factors and the activation energies.

$$\text{Species reduction ratio (SRR)} = \frac{\text{Number of species in the original mechanism}}{\text{Number of species in the reduced mechanism}} \tag{2.2.18}$$

$$\text{Reaction reduction ratio (RRR)} = \frac{\text{Number of reactions in the original mechanism}}{\text{Number of reactions in the reduced mechanism}} \tag{2.2.19}$$

2.2.3 Parameter estimation framework

2.2.3.1 Problem definition

A least-square optimization problem was formulated to estimate the optimal pre-exponential factors and the activation energies of the reactions within a given set

Table 2.2: Sampling conditions for reducing the kinetic model using DRGEP at low and high pressures.

Temperature (K)	**Pressure (atm)**	**Simulation time (s)**
1000	0.15	4000
1100	0.15	4000
1200	0.15	1500
1300	0.15	3000
1400	0.15	1000
1000	0.5	4000
1100	0.5	4000
1200	0.5	1500
1300	0.5	3000
1400	0.5	1000
1000	1	4000
1100	1	4000
1200	1	1500
1300	1	3000
1400	1	1000
1000	2	4000
1100	2	4000
1200	2	1500
1300	2	3000
1400	2	1000
1000	4	4000
1100	4	4000
1200	4	1500
1300	4	3000
1400	4	1000

of bounds. The optimization problem objective was to minimize any discrepancy in the concentration of major species, i.e., methane and hydrogen, between the model and the experimental data at the high-pressure used by Tatum et al. [2]. Note that the reduced model predictions already gave good agreement at low pressures, hence, the data under those conditions was not included in the optimization. The objective function was given by

$$\begin{aligned} \min \quad & \sqrt{\sum_{e=1}^{E} w_e \sum_{b=1}^{B} \sum_{i=1}^{\kappa} \left[X_i^{\exp}(t_b) - X_i^{\text{num}}(t_b) \right]^2} \\ \text{w.r.t} \quad & A_1, E_{a_1}, A_2, E_{a_2}, ..., A_j, E_{a_j} \\ \text{s.t.} \quad & 10^{-10} \leq \frac{A_j^{\text{new}}}{A_j^{\text{old}}} \leq 10^{10} \\ \text{s.t.} \quad & 0.85 \leq \frac{E_{a_j}^{\text{new}}}{E_{a_j}^{\text{old}}} \leq 1.15 \end{aligned} \tag{2.2.20}$$

where index $X_i^{\exp}(t_b)$ is the experimental mole fraction of the i^{th} species at time t_b, $X_i^{\text{num}}(t_b)$ is the model predicted mole fraction of the i^{th} species at time t_b, J is the total number of reactions, κ is the total number of experimentally observed species [1], B is the total number of temporal data points, w_e is the residual weight assigned at each temperature (equal weights used in this work), E is the total number of temperatures at which the experimental data is available, A_j^{old} and A_j^{new} are the initial and new (guess) value of the pre-exponential factor for the j^{th} elementary reaction step, respectively, and $E_{a_j}^{\text{old}}$ and $E_{a_j}^{\text{new}}$ are the initial and new (guess) value of the activation energy for the j^{th} elementary reaction step, respectively. The potential pre-exponential factors were varied by ten orders of magnitude, in each direction, whereas the activation energies were varied by 15% due to the high sensitivity of the reaction to temperature variations.

2.2.3.2 Implementation

The minimization problem in equation (2.2.20) was solved using the Coliny pattern search method within the open source optimization toolbox Dakota [163]. At each

iteration, a maximum of 2ζ potential design sets were created using a coordinate pattern, where ζ is the total number of design variables, and the residual was calculated using Cantera [124]. The lowest residual among all function evaluations at each iteration was compared against the lowest residual of the previous iteration. This process continued until one of the following criteria was met: i) the least-square residual or solution target was ≤ 0.1; ii) the maximum number of function evaluations was reached; or, iii) the convergence tolerance was reached. Table 2.3 gives the parameters used for the fitting process.

Figure 2.2 shows a schematic of the optimization algorithm used. First, Dakota [163] was initialized using the pre-exponential factors and the activation energies of the mechanism in reference [90] as the initial design variables. The framework invokes Cantera [124], runs the required gas phase simulations coupled with the carbon formation model, and returns the least-squared residual to Dakota [163]. The optimization algorithm analyses the residual and determines whether the optimal solution has been achieved. If the optimal solution is not obtained, the framework generates a new design variable set and runs the fitting simulations until the maximum function evaluations are reached.

After a complete optimization cycle, the set of rate parameters obtained after reaching the maximum number of function evaluations was analyzed to assess if there were any design variables that approached their bounds, i.e., within 85% of the bound value. If this is the case, for those variables, the upper and the lower bounds were further expanded by a factor of either 10^3 or 15% depending on the type of variable, i.e., the pre-exponential factor or activation energy, respectively. The best set of rate parameters obtained with modified upper and lower bounds were used as the initial design guess for the next optimization cycle. In the present work, a total of 40 fitting simulations/bound cycles were performed. The design set obtained after running all the fitting simulations was taken as the optimal local solution.

As a local method was used in the present study, the globality of the solution was

Table 2.3: Parameters used for minimizing the objective function.

Parameter name	**Value**
Method	Coliny pattern search
Maximum iterations	1000
Maximum function evaluations	15000
Solution target	10^{-1}
Convergence tolerance	10^{-4} (relative)
Variable tolerance	10^{-5}
Initial delta	10^{-1}
Scaling	None
Expand after success	5 improvements
Pattern basis	Coordinate

tested by generating four different initial search points using a multi-start method and an initial solution manually generated by perturbing the pre-exponential factors (by three orders) and activation energies (by 15%) for the first 30 reactions using the reduced model, in addition to the starting point from the base/reduced mechanism. For each of these starting points, a local minima was found and compared to the minima from the other starting points. The optimal set of parameters among the six starting points corresponding to the lowest residual value was considered as the best solution.

The values of the pre-exponential factor and activation energy for the carbon-forming reaction, as given in Equation (2.1.16), were kept constant during the optimization. For the case of the pressure-dependent reactions, the rate parameters corresponding to a pressure equal to or higher than the operating condition were included in the optimization problem. For example, if the pressure value was between 2 and 5 atm the rate parameters corresponding to pressure 5 atm were included in the fitting simulations. Similarly, for the fall-off reactions, the rate parameters in

the high-pressure limit were optimized. Once the optimization was complete, the modified rate parameters were merged into the original mechanism. As some of the elementary reactions were also modified during the optimization and exhibited pressure dependence due to a significant increase in the rate constant values, they were converted to pressure-dependent Arrhenius form in Cantera [124]. The optimization simulations were run on Cedar clusters that is a part of the Digital research alliance of Canada (previously Compute Canada) and a total of 2 nodes employing Intel E5-2683 v4 Broadwell @ 2.1 GHz CPUs were used for a simulation time of 120 hrs. As a large amount of RAM was needed during the optimization, the full memory of the nodes was utilised.

2.2.4 Reaction path analysis

A reaction path analysis was performed at 892 K, 1093 K, and 1292 K and at 0.5 atm and 4 atm to identify slow and fast reactions responsible for the elemental hydrogen flux at low and elevated pressure conditions. Since element atoms are conserved, the flux for hydrogen atoms in the j^{th} elementary reaction was computed using the expression given by Revel et al. [172], i.e.,

$$\dot{C}_{jik} = \frac{r_j \, {}^{j}N_{\text{H}i} \, {}^{j}N_{\text{H}k}}{{}^{j}\widehat{N}_{\text{H}}} \tag{2.2.21}$$

$$\dot{C}_{ik}(t) = \sum_{j=1}^{J} \dot{C}_{jik}(t) \tag{2.2.22}$$

where $\dot{C}_{jik}$ represents the element flux of, e.g., H atom, from i^{th} species to k^{th} species in j^{th} elementary reaction at a particular time t. J is the total number of elementary reactions, ${}^{j}N_{\text{H}i}$ and ${}^{j}N_{\text{H}k}$ are the number of H atoms for species i and k in the j^{th} reaction, and ${}^{j}\widehat{N}_{\text{H}}$ is the total number of H atoms in reaction j considering both the reactants and products. The summation of the H atom flux from each reaction, as given in equation (2.2.22), gives the total element flux $\dot{C}_{ik}$.

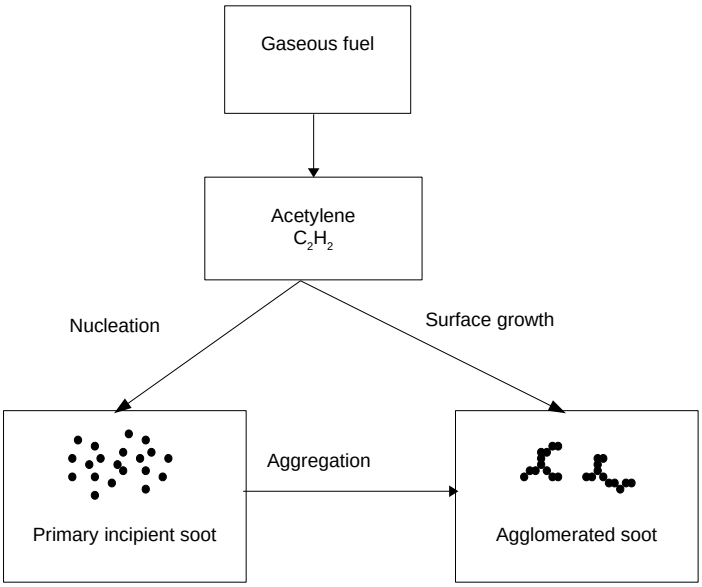

Figure 2.3: Schematic of the soot generated from the gas-phase in the present work.

The overall total element flux was evaluated using Cantera [124] by the summation of all the incoming and outgoing element fluxes for each reactive species in the kinetic mechanism, and the elementary reaction paths were constructed. Figures in Appendix A.2 show illustrations of the reaction path for atomic H for the three experimental conditions in this study. The vertex in the diagram denotes the species and the arrows represent the reactions. The thickness of the arrows is used to identify the major and minor reaction pathways and represent the H element flux. A user-defined threshold for the net element flux was set up to keep only the most important reactions in the reaction path diagram. For this study, a value of 3% of the maximum net element flux (unless stated in the figure caption) was taken as the threshold flux below which the reactions were not included in the analysis diagram.

2.2.5 Soot formation model for the pyrolysis reactor

Another objective of this research will focus on the development of a 0D transient soot formation model for methane pyrolysis under high-pressure. The model will be developed using a monodisperse population balance approach adopted by Kholghy et al. [151] in which, the particles evolve in time with similar morphological characteristics. The monodisperse population balance model is computationally affordable compared to other methods, such as the sectional model [173], where a large number of bins are needed to characterize the particle morphology. As the reaction progresses, these particles grow due to different underlying physics, such as surface growth, aggregation/agglomeration, thereby changing the particles size characterized by particle mobility and gyration diameters.

The soot model is based on the following assumptions:

- Particles nucleating due to acetylene decomposition purely consists of carbon.
- The first particle size is 2 nm.
- Each time-step constitutes particles of only a single size (monodisperse population balance);
- Particles are in point contact during aggregation/agglomeration; and,
- Soot particle density is constant with a value of 1800 kg/m^3 [132, 151].

In order to solve for these state variables, for governing equations are needed. As the model proposed by Kholghy et al. [151] was based on the assumption that particle nucleation happens for a very short period of time, and soot agglomeration and surface growth were mainly responsible for the change in the particle morphology, the particle nucleation in the present work has been assumed to happen till 5 s.

Figure 2.3 shows a schematic of the methodology used for the incipient soot particles and agglomerates generated during a fuel pyrolysis process. Incipient soot

particles are assumed to get generated from acetylene decomposition based on the model by Lindstedt et al. [143]. The carbon formation rate is then converted to the particle concentration rate.

To track the particle characteristics, four different variables were tracked [151], i.e., the total aggregate/agglomerate number, N (#/m^3), total carbon atoms, C_{tot} (mol/m^3), total surface area, A_{tot} (m^2/m^3), concentrations, and aggregate/agglomerate mass, m_{ag}. The governing equation solving for the number density of particles, N, due to collision was given as

$$\frac{\mathrm{d}N}{\mathrm{d}t} = -\frac{1}{2}\beta N^2 \tag{2.2.23}$$

where β is the collision frequency and was given as follows [151]:

$$\beta = 8\pi D d_m \left[\frac{d_m}{d_m + \sqrt{2}g} + \frac{8D}{\sqrt{2}\bar{c}d_m}\right]^{-1} \tag{2.2.24}$$

where D is the diffusion coefficient, g is the mean particle distance, $\bar{c}$ is the mean thermal particle velocity, and d_m is the mobility diameter of an agglomerate calculated using the scaling law given by Kelesidis et al. [174]

$$d_m = d_p \times n_p^{0.45} \tag{2.2.25}$$

where n_p is the number of primary particles in an aggregate, and was calculated using the primary particle diameter [174]

$$m_{\text{ag}} = \rho_{\text{soot}} n_p \pi \frac{d_p^3}{6} \tag{2.2.26}$$

or,

$$m_{\text{ag}} = \frac{m_{\text{tot}}}{N} \tag{2.2.27}$$

$$m_{\text{tot}} = C_{\text{tot}} \times M_{\text{C}} \tag{2.2.28}$$

where d_p is the primary particle diameter, m_{ag} is the mass of a single aggregate/agglomerate, ρ_{soot} is the particle density with a value of 1800 kg/m^3, m_{tot} is the total mass of the particles (kg), C_{tot} is the total carbon molar (mol/m^3), and M_{C} is the molecular weight of carbon (kg/mol). Next, $\bar{c}$ is calculated using

$$\bar{c} = \sqrt{\frac{8k_{\text{b}}T}{\pi m_{ag}}} \tag{2.2.29}$$

where k_{b} is the Boltzmann's constant with a value of 1.38065×10^{-23} J/K. The expression for the term g was given by

$$g = \frac{1}{3d_m\lambda_{\text{particle}}}\Big[(d_m + \lambda_{\text{particle}})^3 - (d_m^2 + \lambda_{\text{particle}}^2)^{3/2}\Big] - d_m \tag{2.2.30}$$

where $\lambda_{\text{particle}}$ is the particle mean free path and was calculated as per the following expression

$$\lambda_{\text{particle}} = \frac{8D}{\pi\bar{c}} \tag{2.2.31}$$

where D is the diffusion coefficient (m^2/s) and was calculated using the Stokes-Einstein expression [175]

$$D = \frac{k_{\text{b}}T}{f} \tag{2.2.32}$$

where f is the particle friction coefficient and was given by

$$f = \frac{3\pi\mu d_m}{\mathbb{C}} \tag{2.2.33}$$

where μ is the viscosity and calculated using an empirical expression given as

$$\mu = 1.425 \times 10^{-6}\Big(\frac{T^{0.5039}}{1 + \frac{108.3}{T}}\Big) \tag{2.2.34}$$

and $\mathbb{C}$ is the Cunningham slip correction factor, and is given by

$$\mathbb{C} = 1 + \frac{2\lambda_{\text{gas}}}{d_m}\Big(A_1 + A_2 \exp\frac{-A_3 d_m}{\lambda_{\text{gas}}}\Big) \tag{2.2.35}$$

where A_1, A_2, and A_3 are constants with a value of 1.21, 0.4, and 0.78, respectively. The mean free path of the gas, λ_{gas}, is given by

$$\lambda_{\text{gas}} = \frac{\mu}{\rho}\sqrt{\frac{\pi M_{\text{gas}}}{2k_b T}} \tag{2.2.36}$$

where M_{gas} is the molecular weight of the gas (taken as CH_4 in this work). The gas density was given by:

$$\rho = M_{\text{gas}}\frac{P}{\text{R}_\text{u} T} \tag{2.2.37}$$

The governing equation for the number of carbon atoms is given by a mass balance based on hydrogen abstraction and acetylene addition (HACA) mechanism [69], and the total rate of change of carbon atoms due to surface growth from acetylene was given by:

$$\Big(\frac{dC_{\text{tot}}}{dt}\Big)^{\text{Sg,HACA}} = 2\gamma\beta_{\text{soot,C}_2\text{H}_2} C_{\text{C}_2\text{H}_2} N n_p \tag{2.2.38}$$

where $\beta_{\text{soot,C}_2\text{H}_2}$ represents the collision frequency between the particle and an acetylene molecule

$$\beta_{\text{soot,C}_2\text{H}_2} = \pi(d_m + d_{\text{C}_2\text{H}_2})^2\sqrt{\frac{k_\text{b} T}{2\pi}\Big(\frac{1}{m_{\text{ag}}} + \frac{1}{m_{\text{C}_2\text{H}_2}}\Big)} \tag{2.2.39}$$

where

$$d_{\text{C}_2\text{H}_2} = \Big(\frac{6M_{\text{C}_2\text{H}_2}}{\rho_{\text{soot}}\pi N_{\text{av}}}\Big)^{1/3} \tag{2.2.40}$$

$$m_{\text{C}_2\text{H}_2} = \frac{M_{\text{C}_2\text{H}_2}}{N_{\text{av}}} \tag{2.2.41}$$

where γ represents the collisions between a particle and molecule [174], $m_{\text{C}_2\text{H}_2}$ is the mass of a single acetylene molecule (kg), α represents the active sites [69], N_{av} is the Avagadro's number with a value of 6.022×10^{23} (#/mol), and $M_{\text{C}_2\text{H}_2}$ is the molecular weight of an acetylene molecule (kg/mol). The value of γ was calculated as

$$\gamma = \frac{\alpha K_s \dot{\chi}_{\text{soot}} A_{\text{ag}}}{\beta_{\text{soot},C_2H_2} N_{\text{av}}} \tag{2.2.42}$$

where A_{ag} is the surface area of a single aggregate given as $(\frac{A_{\text{tot}}}{N})$, K_s represents the reaction rate constant for adding an acetylene molecule to the surface of a soot particle [69] and is calculated using

$$K_s = 80T^{1.56} \exp\Big(-\frac{1912.4}{T}\Big) \tag{2.2.43}$$

$\dot{\chi}_{\text{soot}}$ is the radical site density on the surface of soot particles based on the nucleation and surface growth study by Appel et al. [69]

$$\dot{\chi}_{\text{soot}} = 2.3 \times 10^{19} \tag{2.2.44}$$

The governing equation describing the total surface area is given by noting that the change in area is due to the addition of carbon molar rate. The total surface area of the particles is given by

$$A_{\text{tot}} = \pi d_p^2 n_p N \tag{2.2.45}$$

Taking the differential of A_{tot} and d_p with respect to t on both sides, we get

$$\frac{dA_{\text{tot}}}{dt} = 2\pi d_p n_p N \frac{dd_p}{dt} \tag{2.2.46}$$

Additionally, the total volume of the particles can be calculated as

$$V_{\text{tot}} = \frac{\pi}{6} d_p^3 n_p N \tag{2.2.47}$$

Taking the differential of V_{tot} and d_p with respect to t on both sides, we get

$$\frac{dV_{\text{tot}}}{dt} = \frac{\pi}{2} d_p^2 n_p N \frac{dd_p}{dt} \tag{2.2.48}$$

Implementing the expression obtained for $\frac{dd_p}{dt}$ from Equation (2.2.48) into Equation (2.2.46), we obtain

$$\frac{dA_{\text{tot}}}{dt} = \frac{4}{d_p}\frac{dV_{\text{tot}}}{dt} \tag{2.2.49}$$

where $\frac{dV_{\text{tot}}}{dt}$ can be substituted with

$$\frac{dV_{\text{tot}}}{dt} = \frac{1}{\rho_{\text{soot}}}\frac{dm_{\text{tot}}}{dt} \tag{2.2.50}$$

and $\frac{dm_{\text{tot}}}{dt}$ can be substituted in terms of total carbon molar rate. Thus, the change in the total surface area of the particles was given as

$$\frac{dA_{\text{tot}}}{dt} = \frac{4}{\rho d_p}\Big(\Big(\frac{dC_{\text{tot}}}{dt}\Big)^{\text{Sg,HACA}} M_{\text{C}}\Big) \tag{2.2.51}$$

and the primary particle diameter was calculated as

$$d_p = \frac{6V_{\text{tot}}}{A_{\text{tot}}} \tag{2.2.52}$$

$$V_{\text{tot}} = \frac{m_{\text{tot}}}{\rho_{\text{soot}}} \tag{2.2.53}$$

$$n_p = \frac{V_{\text{ag}}}{36\pi(\frac{V_{\text{tot}}}{A_{\text{tot}}})^3} \tag{2.2.54}$$

The final equation for the mass conservation was derived based on the rate of change of aggregate mass changing due to the coagulation and surface growth phenomena. Equation (2.2.27) can be differentiated with respect to time on both sides and the contributions due to the surface growth and coagulation can be categorised into the following equation

$$\frac{dm_{\text{ag}}}{dt} = \frac{dm_{\text{ag}}}{dt}\bigg|_{\text{sg}} + \frac{dm_{\text{ag}}}{dt}\bigg|_{\text{coagulation}} \tag{2.2.55}$$

The first term in the RHS of Equation (2.2.55) can be written as

$$\frac{dm_{\text{ag}}}{dt}\bigg|_{\text{sg}} = \frac{1}{N}\frac{dm_{\text{tot}}}{dt} \tag{2.2.56}$$

Implementing Equation (2.2.28) in the equation above, we get

$$\left.\frac{dm_{\mathrm{ag}}}{dt}\right|_{\mathrm{sg}} = \left(\left(\frac{dC_{\mathrm{tot}}}{dt}\right)^{\mathrm{Sg,HACA}} \frac{M_{\mathrm{C}}}{N}\right) \tag{2.2.57}$$

The second term in the RHS of Equation (2.2.55) can be written as

$$\left.\frac{dm_{\mathrm{ag}}}{dt}\right|_{\mathrm{coagulation}} = \frac{d(\frac{m_{\mathrm{tot}}}{N})}{dt} \tag{2.2.58}$$

$$\left.\frac{dm_{\mathrm{ag}}}{dt}\right|_{\mathrm{coagulation}} = -\frac{m_{\mathrm{tot}}}{N^2}\frac{dN}{dt} \tag{2.2.59}$$

or,

$$\left.\frac{dm_{\mathrm{ag}}}{dt}\right|_{\mathrm{coagulation}} = -\frac{m_{\mathrm{ag}}}{N}\frac{dN}{dt} \tag{2.2.60}$$

Finally, adding Equations (2.2.57) and (2.2.60), and substituting in Equation (2.2.55), the rate of change of aggregate mass will be calculated as

$$\frac{dm_{\mathrm{ag}}}{dt} = \frac{dC_{\mathrm{tot}}}{dt}\frac{M_{\mathrm{C}}}{N} - \frac{dN}{dt}\frac{m_{\mathrm{ag}}}{N} \tag{2.2.61}$$

A primary particle diameter of 2 nm was assumed that was a result of nucleation from acetylene decomposition. The soot model coupling with the gas-phase was done in a way that nucleation was assumed to occur only till 5 s residence time. Hence, upto 5 s residence time, the amount of carbon generated from acetylene decomposition was converted to 2 nm particles. For the whole of the residence time, the following source terms were used:

$$\frac{dN}{dt} = \begin{cases} \frac{6 r_{j,c} V M_C}{\rho_{\mathrm{soot}} \pi d_p^3} & \text{if } t < 5.0; \\ -\frac{1}{2}\beta N^2 & \text{otherwise.} \end{cases} \tag{2.2.62}$$

where $r_{j,c}$ is the reaction rate for the carbon forming reaction given in Equation (2.1.20) and M_c is the molar mass of carbon. To obtain the particle generation rate, the rate of carbon formation was divided by the mass of a 2 nm particle. Note

that the primary particle diameter does not change during the nucleation, hence, the other dependent variables, i.e, C_{tot}, A_{tot}, and m_{ag}, were converted using the $\frac{dN}{dt}$ from Equation (2.2.62) and given as

$$\frac{dC_{\text{tot}}}{dt} = \begin{cases} \frac{\rho\pi d_p^3}{6M_c}\frac{dN}{dt} & \text{if } t < 5.0; \\ 2\gamma\beta_{\text{soot},C_2H_2}C_{C_2H_2}Nn_p & \text{otherwise.} \end{cases} \tag{2.2.63}$$

$$\frac{dA_{\text{tot}}}{dt} = \begin{cases} \pi d_p^2\frac{dN}{dt} & \text{if } t < 5.0; \\ \frac{4}{\rho d_p}\left(\left(\frac{dC_{\text{tot}}}{dt}\right)^{\text{Sg,HACA}}M_{\text{C}}\right) & \text{otherwise.} \end{cases} \tag{2.2.64}$$

$$\frac{dm_{\text{ag}}}{dt} = \begin{cases} 0 & \text{if } t < 5.0; \\ \frac{dC_{\text{tot}}}{dt}\frac{M_{\text{C}}}{N} - \frac{dN}{dt}\frac{m_{\text{ag}}}{N} & \text{otherwise.} \end{cases} \tag{2.2.65}$$

As the primary particle size does not change during the nucleation period, m_{ag} has a constant value till 5 s. The particle concentration obtained at the end of the nucleation period acted as an initial condition for the aggregation and surface growth terms and solved using Equations (2.2.23), (2.2.38), (2.2.51), and (2.2.61) in time.

Equation (2.1.1) from the gas-phase was coupled to the soot model and the gas-phase model accounted for the changes in H and C_2H_2 concentrations due to HACA mechanism. The change in the total number of carbon results in the modification of the number of hydrogen atoms, H, due to the following reaction from the hydrogen abstraction acetylene addition (HACA) based surface growth mechanism

$$\text{C}_{\text{sooto}} + \text{C}_2\text{H}_2\text{(g)} \longrightarrow \text{C}_{\text{soot–H}} + \text{H}, \qquad [80\ 1/\text{s}, 1.56, 1912.4\ \text{K}] \tag{2.2.66}$$

The overall rate of change of hydrogen consisted of two terms: a) net production or consumption rate in the gas-phase; and b) rate change due to C_{tot}. The change of H with respect to time was calculated via the following equation

$$\frac{d(mY_{\text{H}})}{dt} = \left(S_{\text{H}} + \frac{1}{2}\left(\frac{dC_{\text{tot}}}{dt}\right)^{\text{Sg,HACA}}\right)VM_{\text{H}} \tag{2.2.67}$$

where S_H is the the production or consumption rate of H (mol/(m^3·s)) given by Equation (2.1.2), m is the total mass inside the reactor (kg), and Y_H is the hydrogen atom mass fraction. Similarly, due to the consumption of acetylene on the surface of the soot particles as given in Equation (2.2.38), the net rate of change of acetylene was given as

$$\frac{\mathrm{d}(mY_{\mathrm{C_2H_2}})}{\mathrm{d}t} = \left(S_{\mathrm{C_2H_2}} - \left(\frac{dC_{\mathrm{tot}}}{dt}\right)^{\mathrm{Sg,HACA}} V M_{\mathrm{C_2H_2}} \right) \tag{2.2.68}$$

where $S_{\mathrm{C_2H_2}}$ is the the production or consumption rate of $\mathrm{C_2H_2}$ (mol/(m^3·s)) given by Equation (2.1.2).

2.2.5.1 Coupling with the gas-phase model

The independent transient soot formation model was coupled with the 0D isothermal and isochoric batch reactor gas-phase model in Cantera [124] and implemented in python. The four state variables responsible for tracking soot, i.e., the particle number concentration (N), the total carbon atoms (C_{tot}), the total particle surface area (A_{tot}), and the aggregate mass (m_{ag}), were added to the state variables in the gas-phase. The model in section 2.1.2 was replaced by the soot model by solving four additional governing equations. Hence, the total number of state variables solved, were $I + 4$, where I is the total number of gas-phase species.

Figure 2.4 shows a schematic of the model implementation in the gas and solid phase to obtain particle morphology. The initial reactor conditions, such as temperature, pressure, and methane initial mole fraction, are defined using a given reaction mechanism file. The net rate of change of gaseous species concentrations are then obtained using Cantera. Afterwards, a conditional loop establishes which of the particle sub-models dominate, such as soot nucleation, or agglomeration and surface growth. Finally, Equation (2.1.1) for each gaseous species and Equations (2.2.23), (2.2.38), (2.2.51), and (2.2.61) are merged resulting in a set of ordinary differential equations. The system of equations was solved using the open-source software package Can-

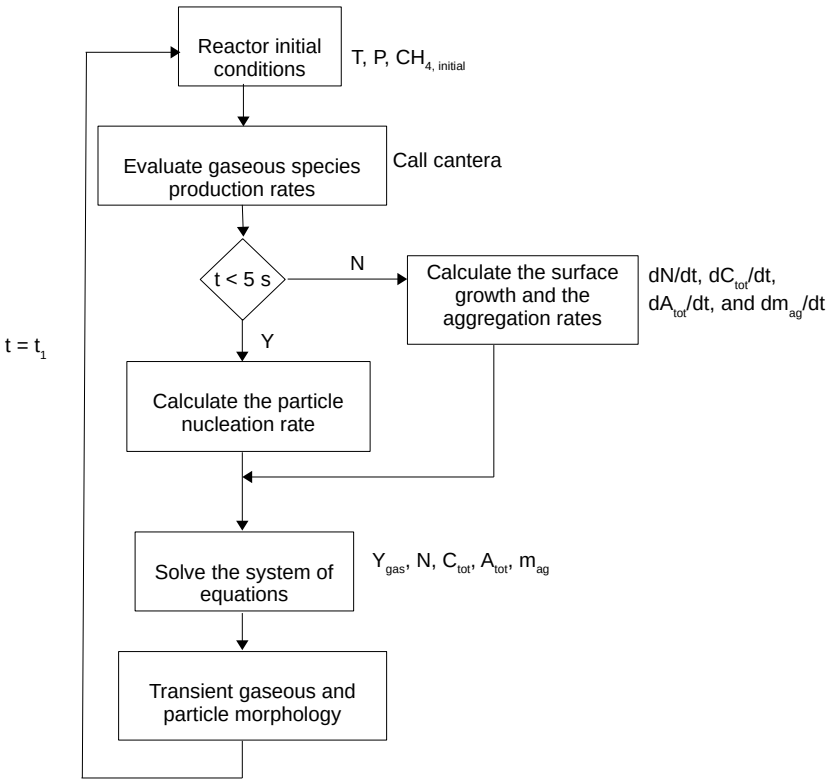

Figure 2.4: Implementation of the soot model and coupling with the gas-phase model to obtain the particle morphology.

tera [124] implemented in python. To solve the system of equations, a 5th-order backward differentiation formula (BDF–5) with a Newton solver was used. Relative and absolute error tolerances of 10^{-9} and 10^{-15}, respectively, are required to achieve solver convergence.

The overall soot model will be implemented as a separate module in Python in conjunction with Cantera [124]. This means that, at each time step, the gas and solid phase equations will be solved simultaneously.

Chapter 3

Mechanism selection[1]

3.1 Results and discussion

3.1.1 Sub-atmospheric pressure operation

Since the majority of batch reactor experiments in the literature were performed under low pressure conditions, these results were first used to evaluate the kinetic models above. Hydrogen and intermediate species concentrations were obtained from the implemented reaction mechanisms and compared to experimental data.

Figure 3.1 shows numerical and experimental results [31, 32] at 1038 K and 59 kPa. Experimental and numerical hydrogen concentration profiles were in good agreement for most of the mechanisms, except for GRIMECH 3.0 [82] and Ranzi et al. [87]'s mechanism. Acetylene's concentration profile was accurately predicted by NUIG-Mech 1.1 [90] and GRIMECH 3.0 [82] mechanisms, but the other mechanisms are only in agreement with the experimental data up to a residence time of around 2000 s. The ethylene concentration profile was accurately predicted by almost all the mechanisms, except GRIMECH 3.0 [82] and Ranzi et al. [87]'s mechanism which over-predicted the ethylene concentration after a residence time of 1500 s. Finally,

[1]Parts of this chapter are reproduced from the following publications:

1. A Punia *et al.*, "Analysis of methane pyrolysis experiments at high pressure using available reactor models," *Chemical Engineering Journal*, p. 144 183, 2023.
2. J. Tatum *et al.*, "Dataset of methane pyrolysis products in a batch reactor as a function of time at high temperatures and pressures," *Data in Brief*, vol. 47, p. 108 953, 2023.

Author contributions are detailed in the Preface of this thesis.

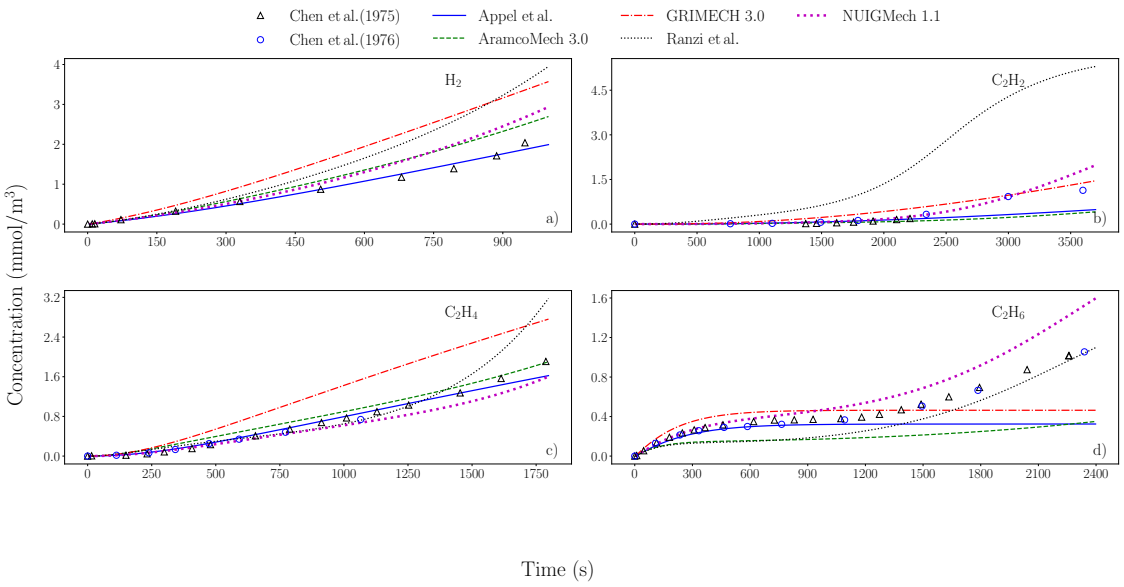

Figure 3.1: Experimental and numerical concentration of a) hydrogen; b) acetylene; c) ethylene; and d) ethane at 1038 K and 59 kPa. Markers represent the experimental data obtained from references [31, 32]. Lines represent the reaction mechanisms used, namely GRIMECH 3.0 [82], NUIGMech 1.1 [90], Ranzi et al. [87], Appel et al. [69], and AramcoMech 3.0 [83]. Data for H_2 was not available in reference [32].

none of the reaction mechanisms, except NUIGMech 1.1 [90] mechanism, was able to track the ethane concentration profile. Ranzi et al. [87]'s mechanism showed a trend similar to the experimental ethane concentration profile, however, a significant under-prediction was observed during the primary (< 300 s) and the secondary (300 s to 1200 s) decomposition stages.

The reaction models were further analyzed at low pressures against the experimental data from references [31, 32] at 995 K and 59 kPa, and 1038 K and 13 kPa, respectively. Figure 3.2 shows the predicted and experimentally obtained ethylene and ethane concentrations at 995 K and 59 kPa. The experiments under these conditions reached only the secondary decomposition stage forming C_2 species. Note that experimental hydrogen and acetylene concentrations were not available in reference [31] and the discussion at 995 K and 59 kPa is limited to ethane and ethylene. The reaction models proposed by NUIGMech 1.1 [90] and Appel et al. [69] accurately predicted the ethylene concentration evolution over the experimental residence time. On the other

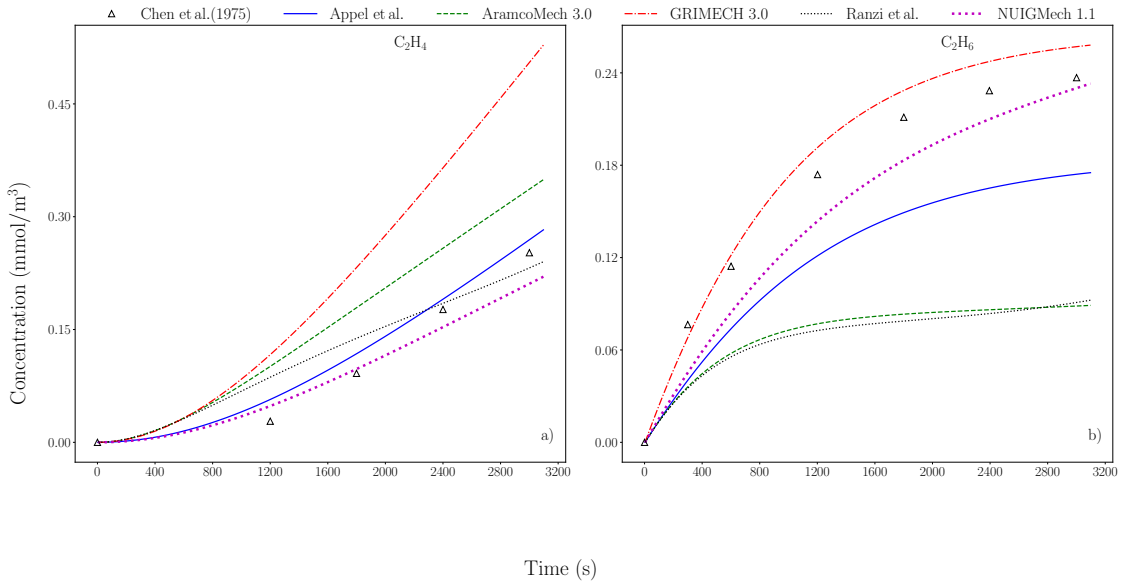

Figure 3.2: Experimental and numerical concentration of a) ethylene; and b) ethane at 995 K and 59 kPa. Markers represent the experimental data obtained from reference [31]. Lines represent the reaction mechanisms used, namely GRIMECH 3.0 [82], NUIGMech 1.1 [90], Ranzi et al. [87], Appel et al. [69], and AramcoMech 3.0 [83].

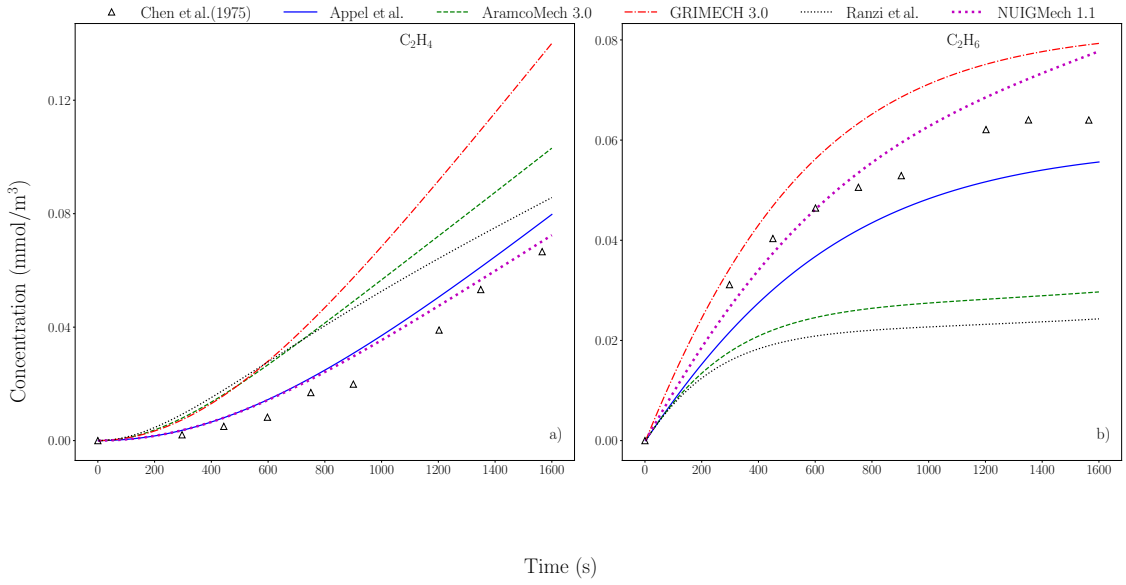

Figure 3.3: Experimental and numerical concentration of a) ethylene; and b) ethane at 1038 K and 13 kPa. Markers represent the experimental data obtained from references [32]. Lines represent the reaction mechanisms used, namely GRIMECH 3.0 [82], NUIGMech 1.1 [90], Ranzi et al. [87], Appel et al. [69], and AramcoMech 3.0 [83].

hand, ethylene concentration is over-predicted by GRIMECH 3.0 [82] and AramcoMech 3.0 [83] mechanisms. Similarly, ethane concentration is accurately predicted by the mechanisms proposed by NUIGMech 1.1 [90] and GRIMECH 3.0 [82], whereas the remaining mechanisms show significant under-prediction. The under-prediction, most likely, will be amplified once the tertiary stage decomposition reactions start and low-pressure ethane autocatalysis is observed.

Figure 3.3 shows the comparison of the model predictions with the experimental data from reference [32] at 1038 K and 13 kPa. The reaction mechanisms by NUIGMech 1.1 [90] and Appel et al. [69] accurately captured the ethylene concentration profile while only the two mechanisms in references [82, 90] agreed well with the ethane experimental data.

Although most of the reaction mechanisms had pressure-dependent rate parameters, only GRIMECH 3.0 [82] and NUIGMech 1.1 [90] mechanisms were able to provide accurate predictions for the intermediate species. Overall, it was found that NUIGMech 1.1 [90] mechanism showed the best agreement with the literature experimental data at low-pressure operating conditions.

3.1.2 Above-atmospheric pressure operation

The results obtained at elevated pressure have been organized in terms of temperature, and for this work, 892 K is referred to as low temperature, 1093 K as medium temperature, and 1292 K as high temperature.

3.1.2.1 Low temperature

Figure 3.4 shows the experimental and numerically predicted molar concentration of MTD products obtained in our reactor at an average temperature of 892 ± 5 K and an initial pressure of 398.8 ± 4 kPa (for this and all other figures the uncertainties represent 95% confidence intervals of the total uncertainty including bias and precision uncertainty). The molar concentration of methane in the products (Figure 3.4a)

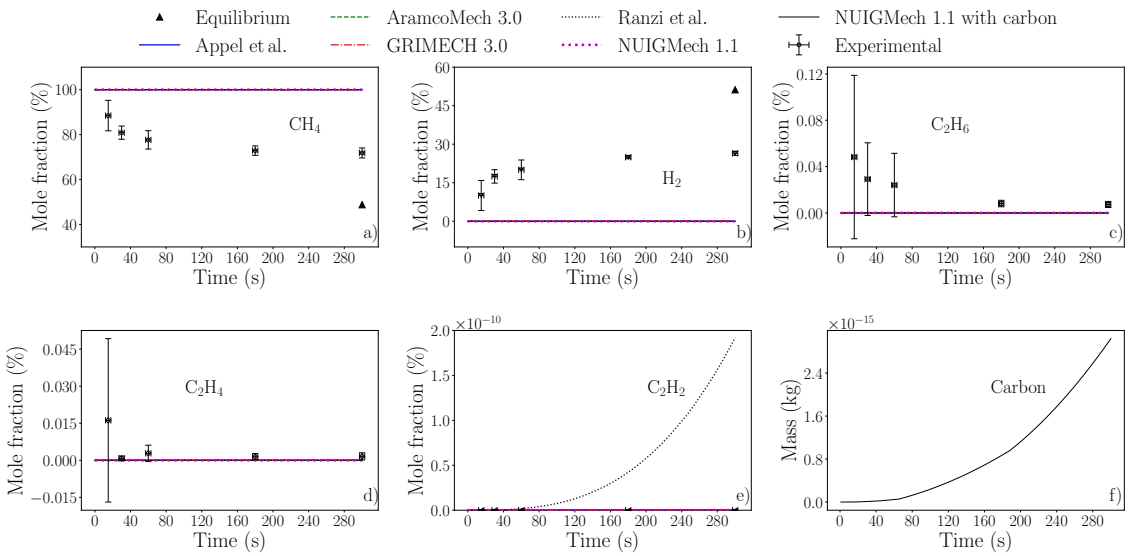

Figure 3.4: Comparison of the model predictions against the in-house experimental data at 892 K and 398.8 kPa for a) methane; b) hydrogen; c) ethane; d) ethylene; e) acetylene; and f) carbon mass. Markers represent the experimental data obtained in this study. Lines represent the reaction mechanisms used, namely GRIMECH 3.0 [82], NUIGMech 1.1 [90], Ranzi et al. [87], Appel et al. [69], and AramcoMech 3.0 [83].

shows that close to 30% of methane decomposed over a residence time of 300 s. During this time period, the decrease in methane mole fraction percentage resulted in the formation of hydrogen up to a mole fraction of 0.25. Other products, such as ethane, ethylene, and acetylene, were found only in very small quantities. During the experiments, carbon formation was observed on the walls of the vessel at all temperatures even at the shortest reaction times (see Appendix A.1). The timing of the carbon formation was in contrast to the observation made by Chen et al. [31] where carbon was observed inside the reactor walls after a residence time of around 240 s at an operating temperature and pressure of 1103 K and 59 kPa.

Model predictions in Figure 3.4 largely deviated from the experimental results with most models showing negligible methane conversion. Thermodynamic analysis shows that at equilibrium (see Appendix A.3) approximately 50% of methane should decompose reaching a hydrogen mole fraction of 0.5 in the products. Based on the equilibrium values, the experimental data appears realistic and kinetically limited.

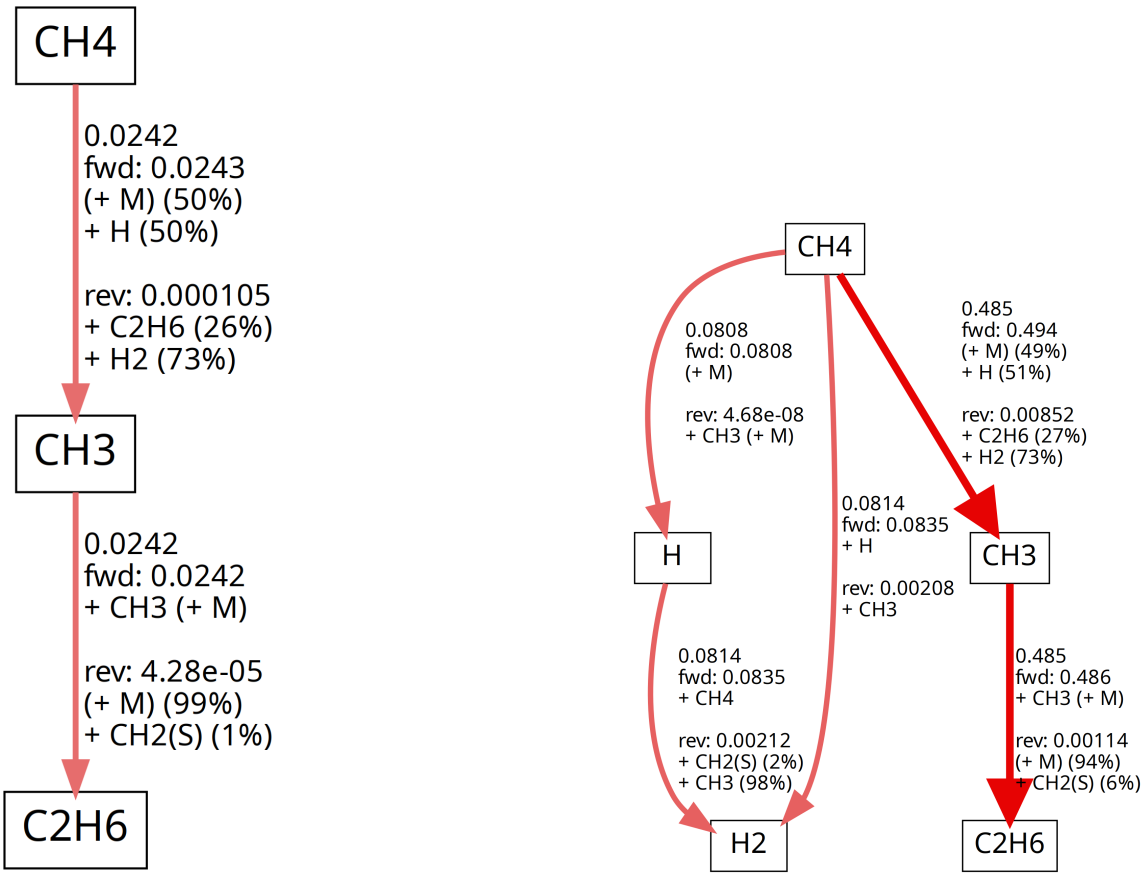

Figure 3.5: Reaction flux diagram for hydrogen element at 0.5 atm (left) and 4 atm (right), 892 K and 300 s using a flux limit of 0.01. NUIGMech 1.1 [90]'s reaction mechanism was used to generate the flux diagram. 'fwd' and 'rev' are the net forward and reverse hydrogen element fluxes, respectively. The number above the 'fwd' flux represents the net flux as given by equation (2.2.22).

Additionally, although intermediate species were found to be present in very small quantities inside the reactor, the model predictions largely deviated from the experimental values. In fact, experimental ethane and ethylene mole fraction percentages attained a peak in the very initial stages of the reaction and gradually decreased over time. Considering that around 30% of methane decomposed to products and carbon formation was evident, it can be said that the intermediate species formation and consumption is fast at elevated pressures which was not the case at sub-atmospheric pressures as observed during the experiments by Chen et al. [31, 32] (slow formation of intermediate species as shown in Figure 3.2). Hence, the lack of agreement with the numerical models is not likely due to experimental error but to an under-prediction of the rate of the reactions at these conditions where the models were not calibrated.

Figure 3.4 shows the model predictions obtained with carbon formation. Methane and hydrogen mole fraction profiles with and without carbon overlap each other. At low temperatures, high pressure decomposition does not accelerate with the inclusion of a solid phase model, especially in the initial reaction stage. This can be attributed to the slow reaction rate for the initial decomposition step where methane decomposes to a methyl radical and a hydrogen atom. Note that the activation energy for the reaction where acetylene goes to carbon and hydrogen was taken as zero to observe faster decomposition. Figure 3.4f shows the mass of carbon generated during the decomposition process. Even without an activation energy, the model does not generate carbon because only a very small amount of methane decomposition was observed in the model. Therefore, it can be said that the results with a gas-phase model do not show carbon removal to have a significant effect on methane decomposition. Since carbon is not formed in the model, its possible impact on accelerating the rate of the reactions would also be negligible.

Considering that the available reaction mechanisms accurately predict methane decomposition products at sub-atmospheric pressures, a gas-phase reaction path flux analysis was performed at below- and above-atmospheric pressure. Figure 3.5 shows

part of the detailed reaction path diagram for H element flux at 300 s (see Appendix Figures A.2 and A.5 for a detailed flux diagram). It can be seen that during the initial decomposition stage (at 30 s), the fall-off reaction CH_4 (+M) $\Longleftrightarrow$ CH_3 + H and the elementary reaction CH_4 + H $\Longleftrightarrow$ CH_3 + H_2 were responsible for the majority of the H element flux transfer. Note that 'M' is a third body collider in the above fall-off reaction. The most important reaction pathways and their flux values do not change until 300 s, at both low- and high-pressure, implying that the reactions responsible for H_2 formation are kinetically slow and do not contribute further to the decomposition process, i.e. the reaction rate parameters are not accurate. As the initial decomposition step was slow, the reaction pathways leading to secondary and tertiary species do not become active. The reaction path diagram also does not show any signs of heavier hydrocarbon formation even though experiments depicted the formation of carbon black. With the inclusion of a carbon black model, the model does not show any methane decomposition and still underpredicts the experimental data at 892 K as seen in Figure 3.4. Based on these observations, it can be concluded that the rate parameters of the reaction mechanism proposed in reference [90] do not reflect homogeneous decomposition conditions at low temperature and elevated pressure and are responsible for the observed under-prediction. Furthermore, tuning the rate parameters of the pressure-dependent reactions in the high-pressure limit, i.e. the fall-off reaction CH_4 (+M) $\Longleftrightarrow$ CH_3 + H and the elementary reaction CH_4 + H $\Longleftrightarrow$ CH_3 + H_2, might help compensate for the delayed H_2 formation.

3.1.2.2 Medium temperature

Figure 3.6 shows the experimentally measured and numerically predicted mole fraction percentages for methane, hydrogen, ethane, ethylene, acetylene, and carbon mass at 1093 K and 398.8 kPa. The increase in temperature results in improved reaction kinetics with approximately 55% of methane decomposing to achieve a 0.52 hydrogen mole fraction. Within the first 15 s, close to 25% of initial methane decomposed

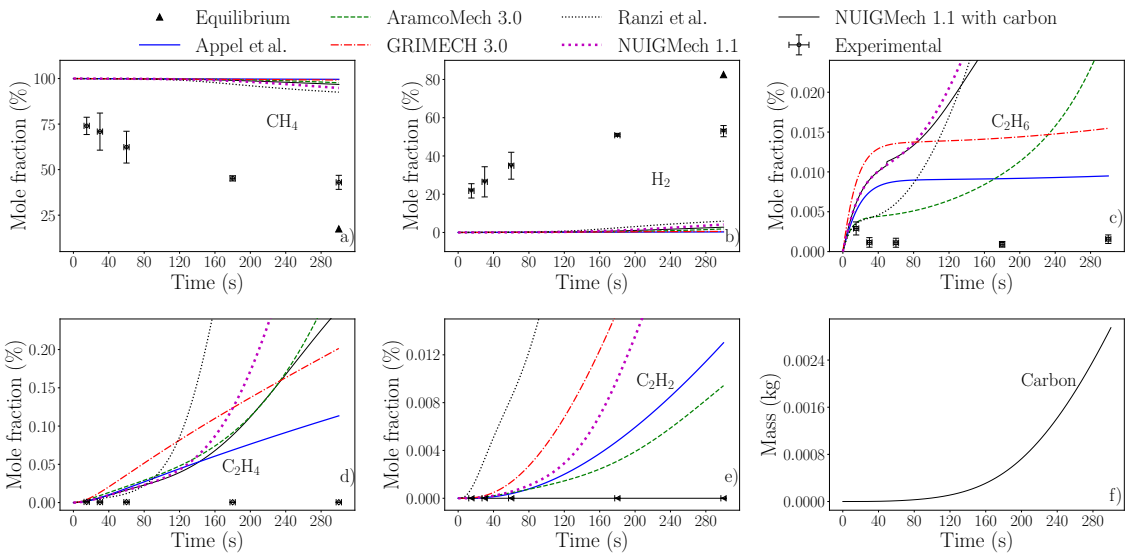

Figure 3.6: Comparison of the model predictions against experimental data at 1093 K and 398.8 kPa for a) methane; b) hydrogen; c) ethane; d) ethylene; e) acetylene; and f) carbon mass. Markers represent the experimental data obtained from this study. Lines represent the reaction mechanisms used, namely GRIMECH 3.0 [82], NUIGMech 1.1 [90], Ranzi et al. [87], Appel et al. [69], and AramcoMech 3.0 [83].

to yield a hydrogen mole fraction of 0.21. The mole fraction percentage profile for methane and hydrogen decreased and increased, respectively, for the first 150 s, after which the secondary and tertiary reactions started contributing to methane formation, leading to equal methane consumption and formation rates [31, 32]. Due to a net zero formation rate, the amount of methane and hydrogen do not change with an increase in the residence time.

The numerical models in Figure 3.6 still under-predict methane ($\approx$ 6% decomposition from NUIGMech 1.1 [90] mechanism) and hydrogen mole fraction percentages. The equilibrium analysis shows that close to 82% of methane should decompose to a product mixture containing a hydrogen mole fraction of 0.83. The equilibrium values of methane and hydrogen show that the experimental data is well within the maximum possible decomposition value. Numerically, the reaction models implemented in the gas phase are not able to accelerate the decomposition rate and accurately follow the high-pressure data. Figure 3.7 shows the refined reaction path diagram for

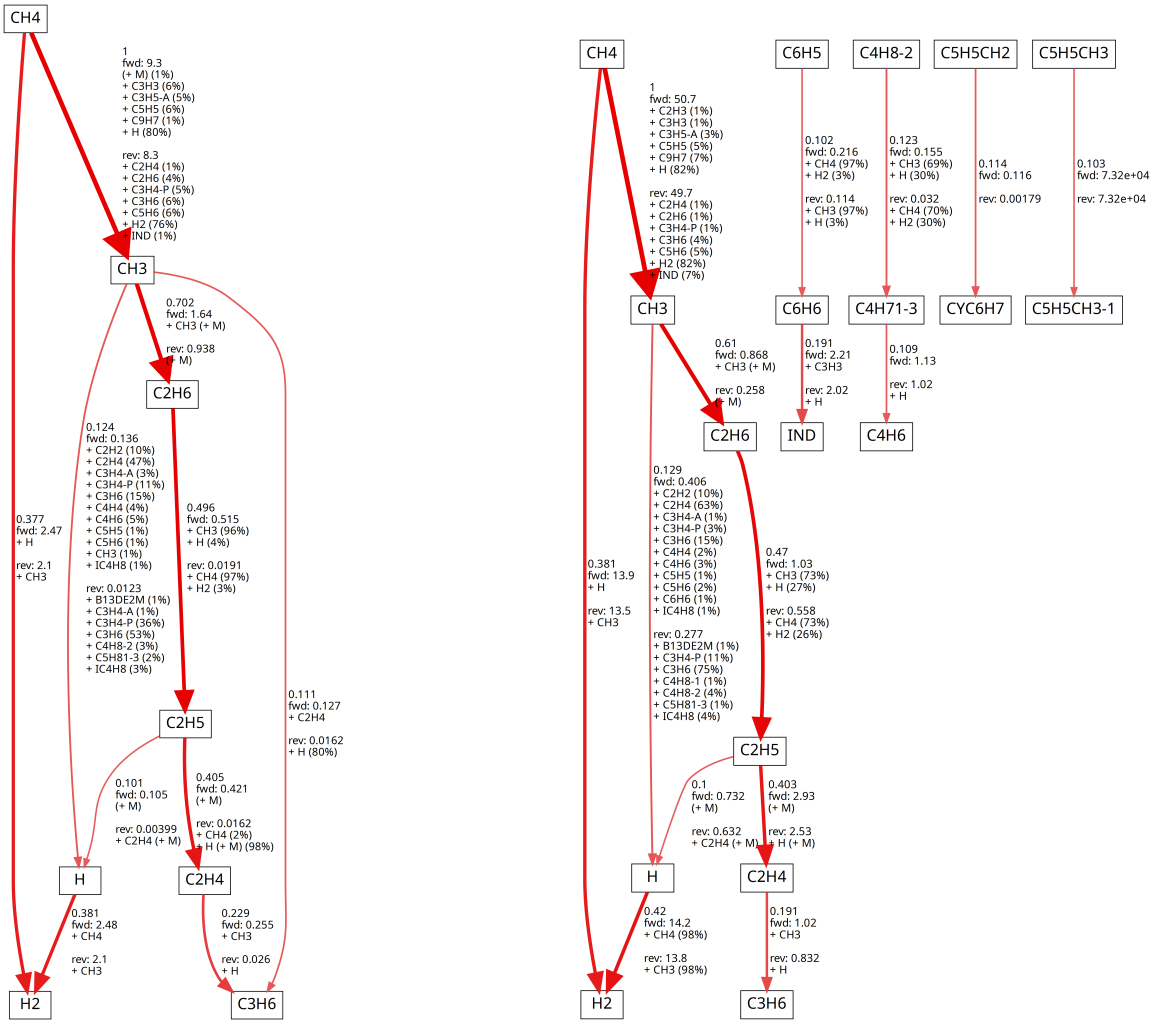

Figure 3.7: Reaction flux diagram for hydrogen element at 0.5 atm (left) and 4 atm (right), 1093 K and 300 s using a flux limit of 0.1. A flux threshold was used to filter the reactions below the value provided in the sub-caption. NUIGMech 1.1 [90] reaction mechanism was used to generate the flux diagram. 'fwd' and 'rev' are the net forward and reverse hydrogen element fluxes, respectively. The number above the 'fwd' flux represents the net flux as given by equation (2.2.22). 'IND' in subfigure b refers to indene (C_9H_8).

H element flux (see Appendix Figures A.3 and A.6 for a detailed flux diagram). The reactions, such as $2CH_3$ (+M) $\Longleftrightarrow$ C_2H_6, C_2H_6 + CH_3 $\Longleftrightarrow$ C_2H_5 + CH_4, C_2H_6 + H $\Longleftrightarrow$ C_2H_5 + H_2 and C_2H_5 (+M) $\Longleftrightarrow$ C_2H_4 + H, were found to have a lower flux value at high pressure (4 atm) as compared to low pressure (0.5 atm) at a residence time of 300 s. The other major pathways, such as CH_4 + H $\Longleftrightarrow$ CH_3 + H_2 and reactions involving the CH_3 radical leading to the formation of the reactive H atom, were found to have a marginally higher H element flux value at high pressure (4 atm) as compared to low pressure (0.5 atm) at a residence time of 300 s. Due to a lower flux value, the contribution to hydrogen formation at high pressure is hindered and the reaction model under-predicts hydrogen mole fraction percentage. While tracking the transient hydrogen evolution, a lower element flux value at elevated pressure shows inconsistency in the reaction rate parameters, especially for the fall-off reactions in the high-pressure limit. The elementary reactions involving the CH_3 radical and leading to hydrogen formation via ethane and ethyl reaction pathway might be responsible for the observed under-prediction at high pressure and medium temperature conditions.

The intermediate species mole fraction profiles, as shown in Figure 3.6, for ethylene, ethane, and acetylene, are over-predicted by NUIGMech 1.1 [90], Ranzi et al. [87], and AramcoMech 3.0 [83] mechanisms. Figure 3.8 shows a comparison of ethane concentration profile at sub-atmospheric and above-atmospheric pressure and at approximately the same temperature ($\approx$ 1103 K), that allows us to compare the difference in the pressure-dependent decomposition chemistry and the related model accuracy. The sub-atmospheric experiments (at 59 kPa) performed by Chen et al. [32] showed autocatalysis in ethane concentration profile at 1103 K which the model in reference [90] accurately tracked, whereas during the in-house experiments at 1093 K, ethane autocatalysis was absent and the model predictions (showing autocatalysis) were offset by a large margin. Instead, the intermediate species attained a peak in the initial stages of the decomposition and gradually reduced with time. The intermediate species predictions by the kinetic model show that the rate parameters for the

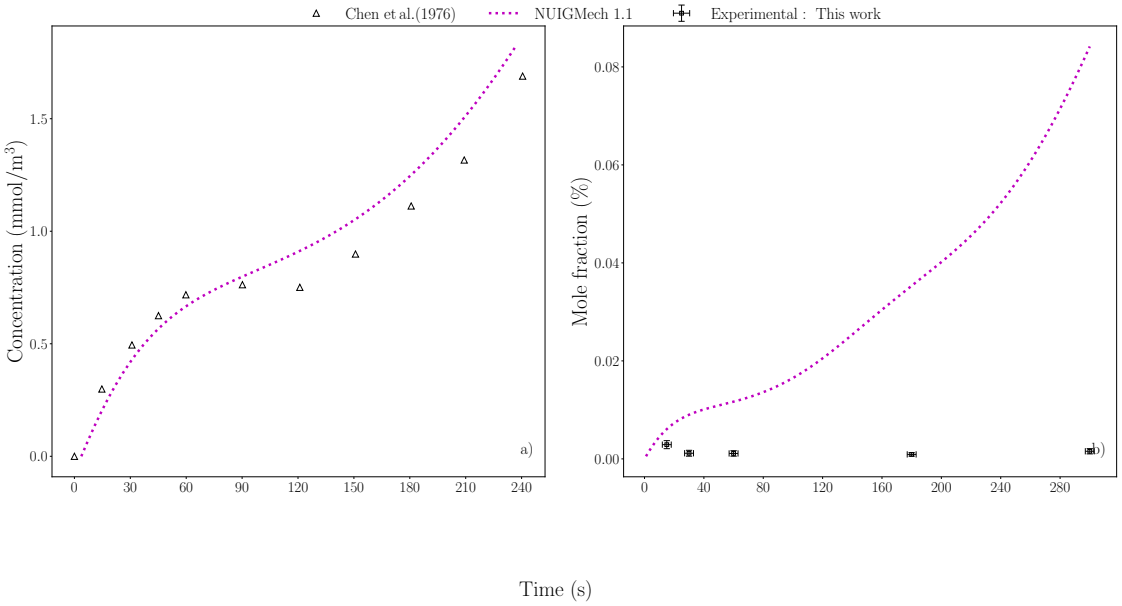

Figure 3.8: Comparison of the model predictions for ethane at sub- and above-atmospheric pressure conditions. Markers in sub-figure a) represent the sub-atmospheric pressure experimental data obtained from reference [32] at 1103 K and 59 kPa, whereas the markers in sub-figure b) represent the high pressure experimental data obtained from the experimental facility at 1093 K and 398.8 kPa. Line represent the reaction mechanism used, namely NUIGMech 1.1 [90]. Note that y-axis data in sub-figure a) was available in concentration units and hence taken as it is from the article [32].

elevated pressure condition are not fast enough and need to be properly estimated.

Chen et al. [32] did not observe soot formation on the reactor walls until a residence time of 240 s. This means that the decomposition remained slow under low pressure conditions. On the other hand, in the present work, soot formation was visible in the initial stages of methane decomposition. The early decomposition of the intermediate species to carbon at elevated pressure could be another reason for the over-prediction which none of the available reaction models account for.

Figure 3.6 also shows the decomposition results obtained with carbon formation at 1093 K and 398.8 kPa. At these conditions, the model still underpredicts the experimental mole fraction percentages for methane and hydrogen. Although the model shows signs of decomposition after 120 s, it is far below the experimental observations. The mass transfer from gas to the solid-phase is negligible. Figure 3.6f shows the transient evolution of carbon mass generated inside the reactor. A negligible amount of carbon formed at 1093 K and 398.8 kPa shows that methane decomposition has not yet been initiated. The intermediate species profile is overpredicted with or without solid carbon. The mole fraction percentage of acetylene is always zero in the carbon model, which confirms that acetylene in the gas-phase is decomposed to solid carbon and hydrogen, and the latter returns back to the gas-phase. The observed discrepancy at 1093 K with the experimental results can be attributed to the slow kinetic rate parameters of the initial methane decomposition reaction.

3.1.2.3 High temperature

Figure 3.9 shows the comparison of the experimental and numerical mole fraction profiles of methane, hydrogen, ethane, ethylene, acetylene, and the numerical carbon mass at 1292 K and 398.8 kPa. A 55% decomposition in methane was observed and hydrogen mole fraction was found to be around 0.53. Most of the decomposition occurred in the first 60 s, after which methane decomposition and hydrogen formation attained a steady-state value. The gas pressure inside the reactor rose by a factor of

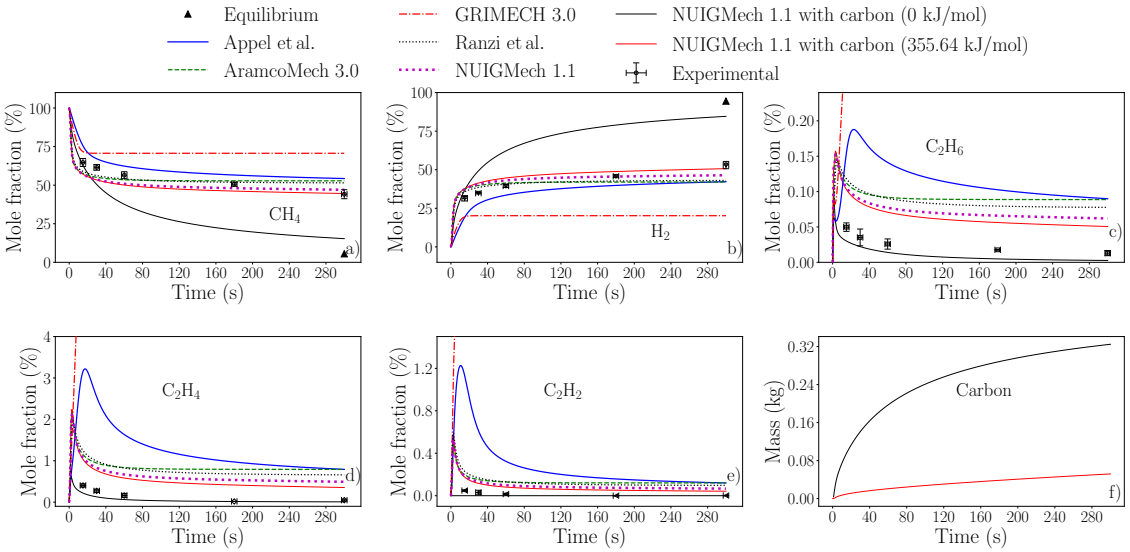

Figure 3.9: Comparison of the model predictions against experimental data at 1292 K and 398.8 kPa for a) methane; b) hydrogen; c) ethane; d) ethylene; e) acetylene; and f) carbon mass. Markers represent the experimental data obtained from this study. Lines represent the reaction mechanisms used, namely GRIMECH 3.0 [82], NUIGMech 1.1 [90], Ranzi et al. [87], Appel et al. [69], and AramcoMech 3.0 [83]. Note that the results for the legend 'NUIGMech 1.1 with carbon' were obtained using a reduced NUIGMech 1.1 mechanism at 1292 K and 398.8 kPa.

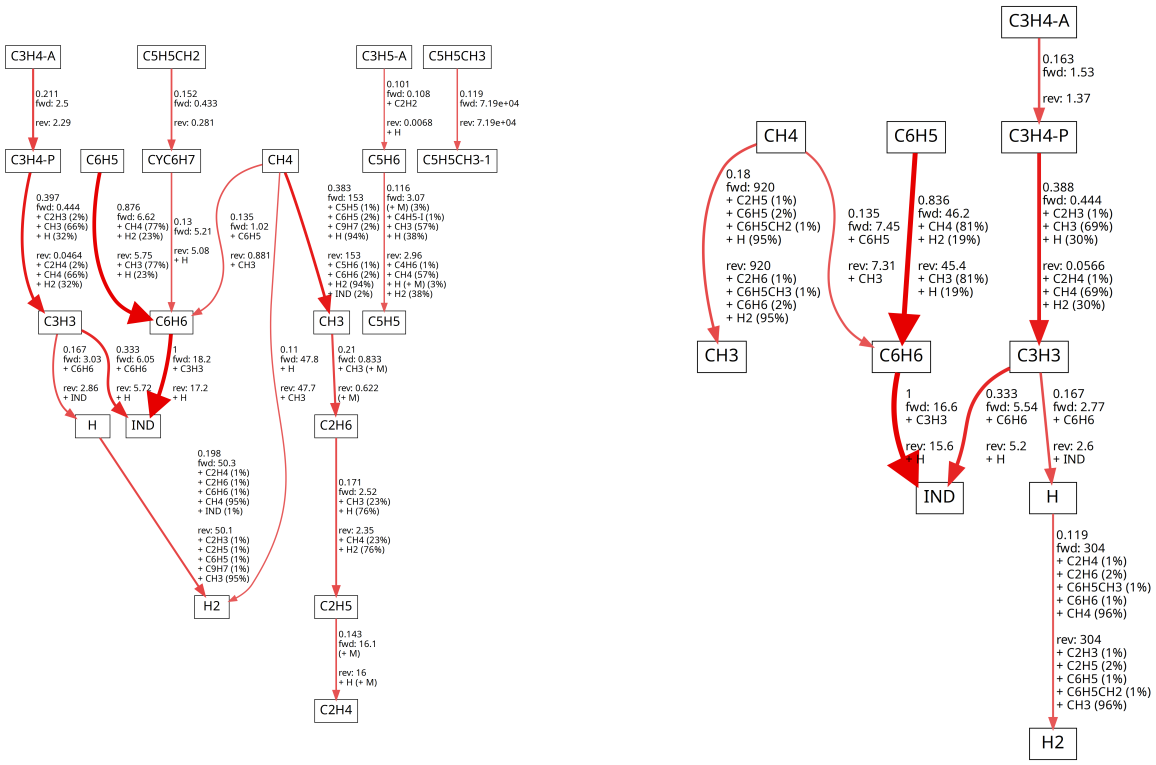

Figure 3.10: Reaction flux diagram for hydrogen element at 0.5 atm (left) and 4 atm (right), 1292 K and 300 s using a flux limit of 0.1. A flux threshold was used to filter the reactions below the value provided in the sub-caption. NUIGMech 1.1 [90] reaction mechanism was used to generate the flux diagram. 'fwd' and 'rev' are the net forward and reverse hydrogen element fluxes, respectively. The number above the 'fwd' flux represents the net flux as given by equation (2.2.22). 'IND' in subfigures a and b refers to indene (C_9H_8).

1.3 during the course of the overall decomposition.

Except for GRIMECH 3.0 [82] mechanism, the rest of the kinetic models closely followed methane and hydrogen mole fraction percentage trends at 1292 K and 398.8 kPa. Baighmohammadi et al. [90]'s reaction model showed the best agreement with the experimental data. The equilibrium analysis predicted methane and hydrogen mole fraction values of 0.05 and 0.94, respectively.

Figure 3.10 shows the subset of the detailed reaction path diagram for H element flux (see Appendix Figures A.4 and A.7 for a detailed flux diagram). It can be seen that the cumulative H element flux transferred from the initial decomposition fall-off reaction, CH_4 (+M) $\Longleftrightarrow$ CH_3 + H, and H $\Longleftrightarrow$ H_2 pathway, was lower at above-atmospheric pressure as compared to the flux values obtained at sub-atmospheric pressure. The fall-off reaction, $CH_4 \Longleftrightarrow CH_3$ + H, was still important for H_2 formation although the decomposition chemistry had shifted towards heavier hydrocarbons as discussed next.

A peak in the intermediate species mole fraction profiles, as shown in Figure 3.9, was observed in the first 20 s of the experiments, after which the species concentrations reduced gradually. The models over-predict the intermediate species, namely ethane, ethylene, and acetylene, until the first peak observed and thereafter. The closest agreement for the intermediate species is obtained from the reaction model by NUIGMech 1.1 [90]. The remaining models, except for GRIMECH 3.0 [82] mechanism, provide a similar mole fraction trend, although the deviation from the experimental data is large. Reaction path analysis for H in Figure 3.10 shows that at high pressure the decomposition chemistry is shifted towards reactions involving heavier hydrocarbons, such as C_6H_6 and IND (C_9H_8). The hydrogen element flux initially originating from the primary and the secondary species shifted towards the tertiary and C_6 hydrocarbons. The maximum hydrogen element flux after a residence time of 300 s originated from the reactions, $C_6H_5 + CH_4 \Longleftrightarrow C_6H_6 + CH_3$, $C_6H_5 + H_2 \Longleftrightarrow C_6H_6$ + H and $C_6H_6 + C_3H_3 \Longleftrightarrow C_9H_8$ + H. Hence, it can be seen that

methane decomposition reached a stage where the heavier hydrocarbons are leading the contribution to hydrogen formation. However, due to the lack of a solid-phase model, the decomposition pathway to solid carbon and hydrogen is unavailable and the reaction mechanisms over-predict the intermediate species profiles. The model results obtained with carbon formation are discussed in the next paragraph.

It is to be noted that methane decomposition at higher temperatures and pressures becomes complex and the chemistry associated with it is very fast. For this reason, with the inclusion of carbon, the system of equations is stiff and the ODE solver encountered numerical instability and failed to converge. When the detailed mechanism [90] is used at 1292 K and 398.8 kPa, the solver does not converge even after reducing the step size from 1 s to 10^{-4} s. Increasing the maximum number of steps taken internally from 500 to 1000 did not improve convergence. Further refining the step size would require a significant computational load, and it is uncertain whether the solver will converge. Therefore, to numerically predict the decomposition products at 1292 K and 398.8 kPa with carbon, the detailed model consisting of 1516 reactions and 325 species was first reduced using the methodology defined in reference [97]. The resulting mechanism consisted of 343 reactions and 60 species and the result obtained with carbon formation at 1292 K and 398.8 kPa is shown in Figure 3.9. At elevated temperatures, it can be seen that the model overpredicts the experimental methane decomposition and hydrogen mole fraction values at times greater than 15 s. Intermediate species formation is accurately tracked with the inclusion of a solid phase model. One reason for the overprediction is that no activation energy was used while transferring mass from the gas phase to the solid phase. Increasing the artificially low activation energy of acetylene converting to carbon and hydrogen would decrease methane conversion. When the activation energy of the sink reaction was increased to 355.64 kJ/mol, the model predictions were significantly improved. The former value of 0 kJ/mol is used to illustrate the largest possible conversion to carbon while the latter value of 355.64 kJ/mol is obtained empirically to be able to

achieve good agreement with experimental data. Figure 3.9f shows the increase in the mass of carbon formed inside the reactor with time. It can be seen that the carbon growth profile is directly proportional to the methane decomposition trend due to faster kinetics. These results show that including the formation of solid carbon in the reaction mechanism for methane pyrolysis is necessary to improve the agreement with the experimental data. Future work will focus on calibrating the gas and solid phase kinetic rate parameters so that the experimental data could be reproduced.

3.1.3 Discussion

The comparison between the experimental data obtained from the literature [31] and in the present study to gas phase numerical model predictions show that the available reaction models only provide accurate predictions at sub-atmospheric pressure, and above-atmospheric pressure and high temperature but not at above-atmospheric pressure and low temperature. The H element reaction flux pathway analysis shows that hydrogen formation via different elementary pathways in the low temperature and elevated pressure regime is so slow that it becomes impossible for the current reaction models to accurately follow the evolution of the decomposition products. Fall-off reactions, such as methane dissociating to methyl radical and hydrogen atom, and methyl recombination reaction to form ethane, initiating the decomposition process and contributing to the hydrogen formation have a lower H element flux value at high pressure as compared to the flux value at sub-atmospheric pressures. The lower flux value implies that the rate parameters for the pressure-dependent reactions are not accurate and need to be increased especially in the high pressure limit.

The results obtained from the gas phase numerical models show that NUIG-Mech 1.1 [90]'s mechanism performs the best among the ones considered. The mechanism is firmly based on thermochemical principles and has been validated against a large set of experimental databases. It might be possible that the data at 4 atm and the lower temperatures reflect the catalytic initiation of the pyrolysis process by

the carbon formed during the reaction at 892 K and 1093 K where the gas-phase decomposition would be relatively slow. On the other hand, at 1292 K and 4 atm, the faster gas-phase decomposition can compete with the catalytic initiation hence a good agreement with the experimental data is obtained.

Overall, it is possible that the lack of model agreement is due to incorrect reaction rate parameters, missing catalysis in the numerical model, or both. Designing an experiment that would allow for the measurement of only homogeneous reactions under the present conditions is highly desirable; however, such an experiment is challenging with a batch reactor because either methane has to be diluted or the experiment has to be carried out at very small residence times to avoid the formation of carbon particles. Operating the reactor at a low partial pressure of methane will produce decomposition results for low pressure cases, a topic already studied in the literature. Also, it is very difficult to carry out experiments corresponding to residence times of the order of milliseconds in a batch reactor. Unfortunately, it is not possible to obtain measurements of homogeneous reactions under the present reactor operating conditions.

The gas-phase model with carbon formation is observed to show accelerated decomposition at 1292 K and 398.8 kPa, whereas the model still underpredicts methane and hydrogen mole fraction profiles at 892 K and 1093 K. Finally, it becomes critical to fit NUIGMech 1.1 [90] mechanism rate parameters taking into account the carbon generated inside the reactor and comparing that to the experimental data obtained in the present study.

3.2 Conclusion

A batch reactor was fabricated and used to study MTD at high pressure and varying temperature [2]. To analyze the results, a batch reactor numerical model was also developed and equipped with a variety of reaction mechanisms. The model was first validated in the gas phase by reproducing available experimental literature data

before being used to analyze experimental results and perform a H flux reaction path analysis.

High pressure methane pyrolysis experiments were performed in the temperature range of 892–1292 K at a pressure of 4 atm. Compared to decomposition under sub-atmospheric conditions, high pressure conditions resulted in higher methane conversion and hydrogen formation, especially at lower temperatures, such as 892 K and 1093 K. Available reaction mechanisms were not able to accurately track the decomposition products at low temperatures and elevated pressure without carbon formation. At high temperature and pressure (1292 K and 4 atm), most of the reaction models accurately predicted methane and hydrogen mole fractions, and the first peak of the intermediate products. NUIGMech 1.1 [90] mechanism provided the best agreement with the sub- and above-atmospheric pressure experimental data.

A reaction path flux analysis showed that the deviation in the model predictions is due to the low reaction rates of fall-off reactions, such as $CH_4 \Longleftrightarrow CH_3 + H$ and $2\ CH_3 \Longleftrightarrow C_2H_6$, under low and medium temperature and high pressure conditions.

A gas-phase model accounting for the solid carbon was implemented based on the reaction of acetylene converting to carbon and hydrogen. The inclusion of the solid carbon did not show any significant rise in methane decomposition at 892 K and 1093 K. At 1292 K, the model overpredicted the experimental data which was attributed to the artificially low activation energy used for the carbon formation. Based on the model results, it can be said that the rate parameters of the reaction mechanism are slow and need to be tuned for high pressure methane pyrolysis conditions. The presented experimental data should be taken into consideration while calibrating the reaction rate parameters for elevated pressure conditions.

Chapter 4

Mechanism reduction and rate parameter optimization[1]

4.1 Model reduction

NUIGMech 1.1 [90] was reduced, against the target conditions mentioned in Section 2.2.2, to a skeletal mechanism consisting of 60 species and 343 reactions with an overall induced error of 25.69% compared to the original mechanism. An overall species and reaction reduction ratio of 4.41 and 5.41 were obtained, respectively, within the error provided. Figure 4.1 shows the reduction iterations in the number of species, reactions, and the error induced (see Appendix Table B.1 for tabulated error values at each reduction stage) vs the threshold value used. The stopping criteria for the simulations was a threshold value of 0.2 or an overall error of 30% in the reduced mechanism whichever was attained first. The simulations started from a threshold value of 0.01 and by the time it reached a value of 0.08, the error in the reduced mechanism was 25.69%. For the next threshold value of 0.09, the error in the reduced

[1]Parts of this chapter are reproduced from the following publications:

1. A Punia *et al.*, "Analysis of methane pyrolysis experiments at high pressure using available reactor models," *Chemical Engineering Journal*, p. 144 183, 2023.
2. J. Tatum *et al.*, "Dataset of methane pyrolysis products in a batch reactor as a function of time at high temperatures and pressures," *Data in Brief*, vol. 47, p. 108 953, 2023.
3. A. Punia *et al.*, "A reduced methane pyrolysis mechanism for above-atmospheric pressure conditions," *Chemical Engineering Journal*, vol. (Under review),

Author contributions are detailed in the Preface of this thesis.

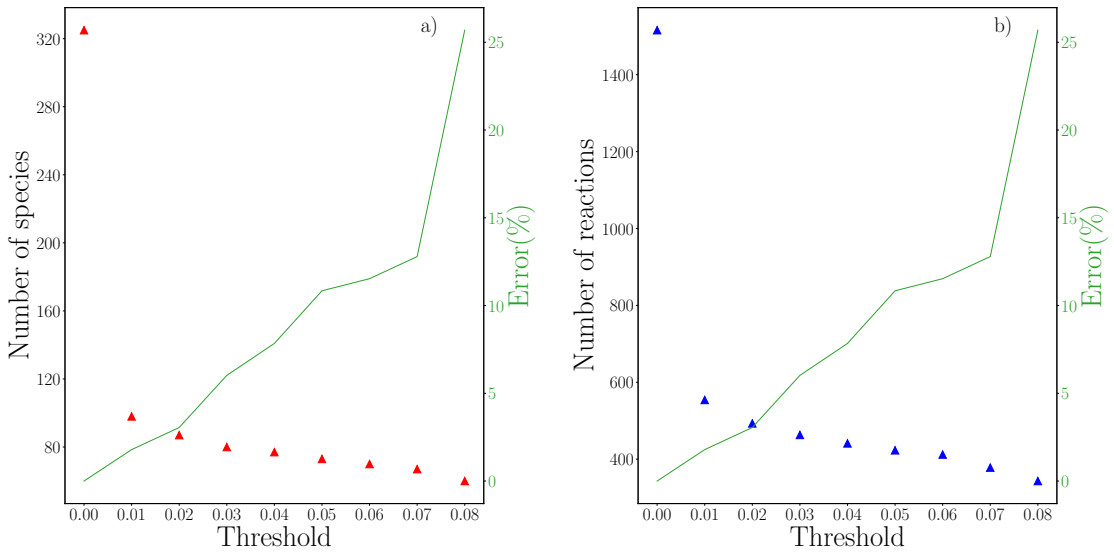

Figure 4.1: Comparison of the number of species, number of reactions, and overall error with an increase in the threshold.

mechanism was more than 30% and hence the simulation was terminated. The majority of the reduction happened in the first iteration where 227 species and 962 reactions associated with them were eliminated while inducing an error of only 1.79%. After this step, the reduced model consisted of 98 species and 554 reactions. Following the first reduction iteration, the slope of the species/reaction reduction gradually became flat, and the target species were found to be sensitive to the removal of the remaining species. Hence, further reduction in the number of species and reactions increased the overall error.

4.1.1 High-pressure (HP) reduction

The reduced model predictions were compared against the original model predictions [90] at temperatures of 892 K, 1093 K, and 1292 K, and an initial reactor pressure of 398.8 kPa in Figures 4.2, 4.3, and 4.4. At 892 K and 1093 K, due to the slower kinetics, the original and reduced models do not show any finite methane decomposition. Intermediate species at 1093 K, such as ethane, ethylene, and acetylene, were slightly overpredicted by the reduced model compared to the original model pre-

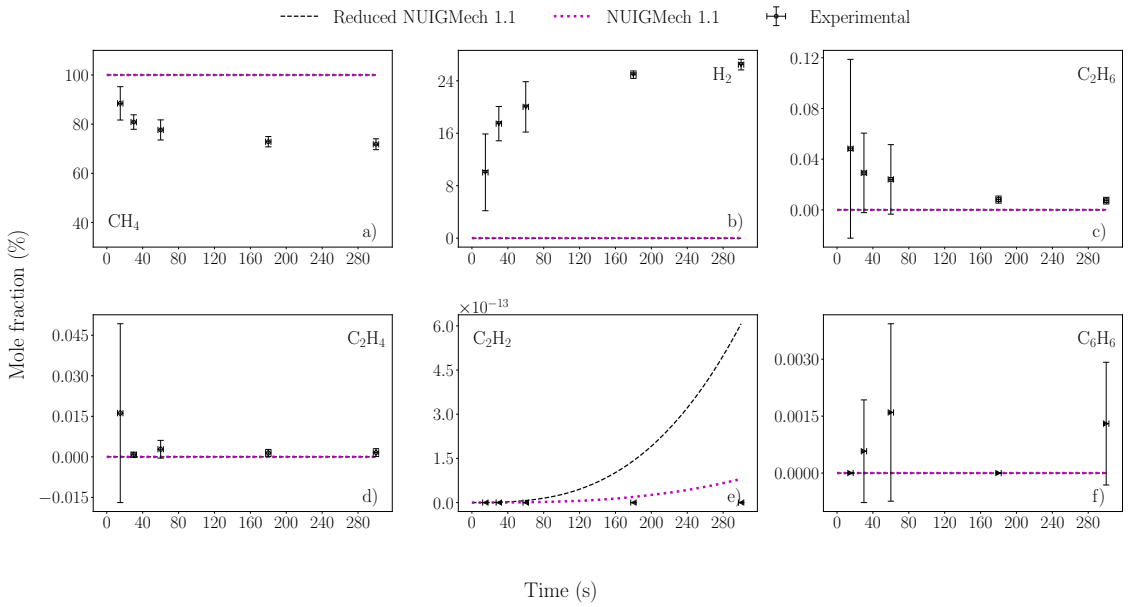

Figure 4.2: Comparison of the original and the reduced model predictions at 892 K and 398.8 kPa for: a) methane; b) hydrogen; c) ethane; d) ethylene; e) acetylene; and f) benzene.

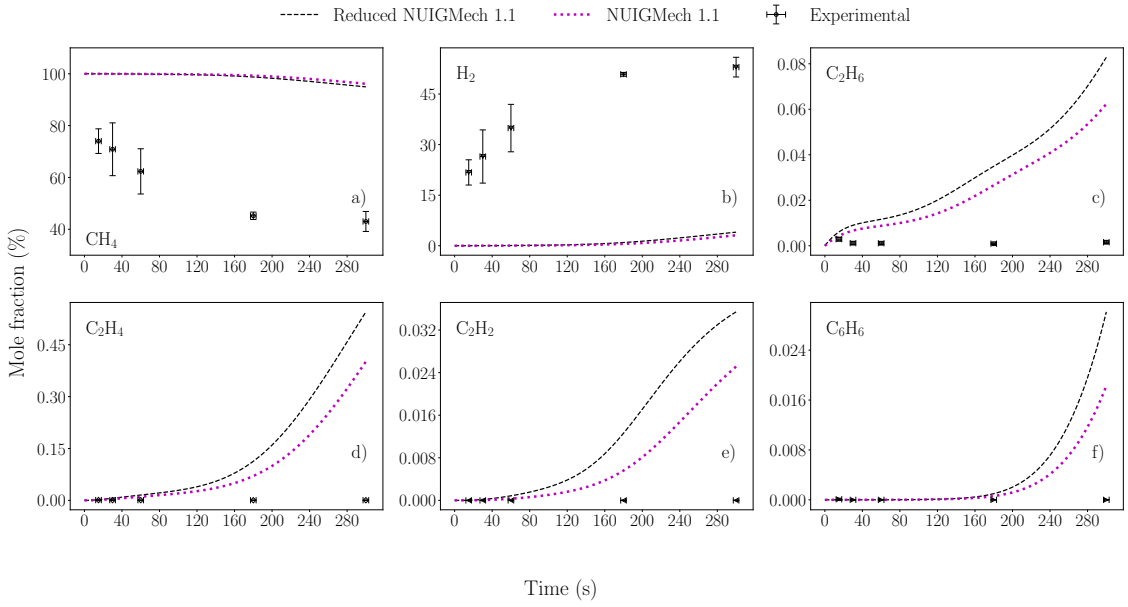

Figure 4.3: Comparison of the original and the reduced model predictions at 1093 K and 398.8 kPa for: a) methane; b) hydrogen; c) ethane; d) ethylene; e) acetylene; and f) benzene.

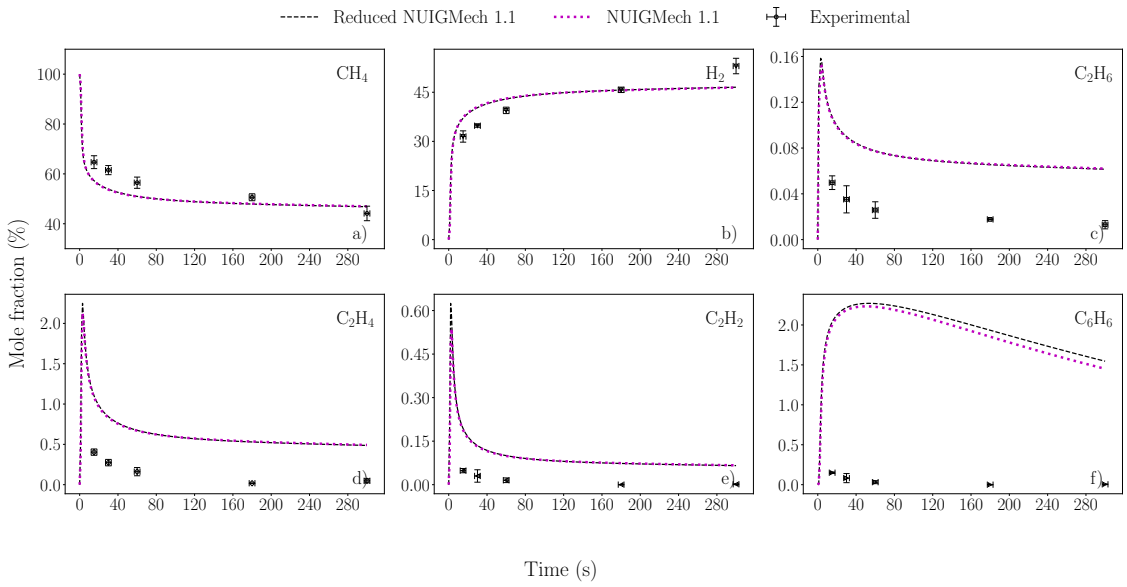

Figure 4.4: Comparison of the original and the reduced model predictions at 1292 K and 398.8 kPa for: a) methane; b) hydrogen; c) ethane; d) ethylene; e) acetylene; and f) benzene.

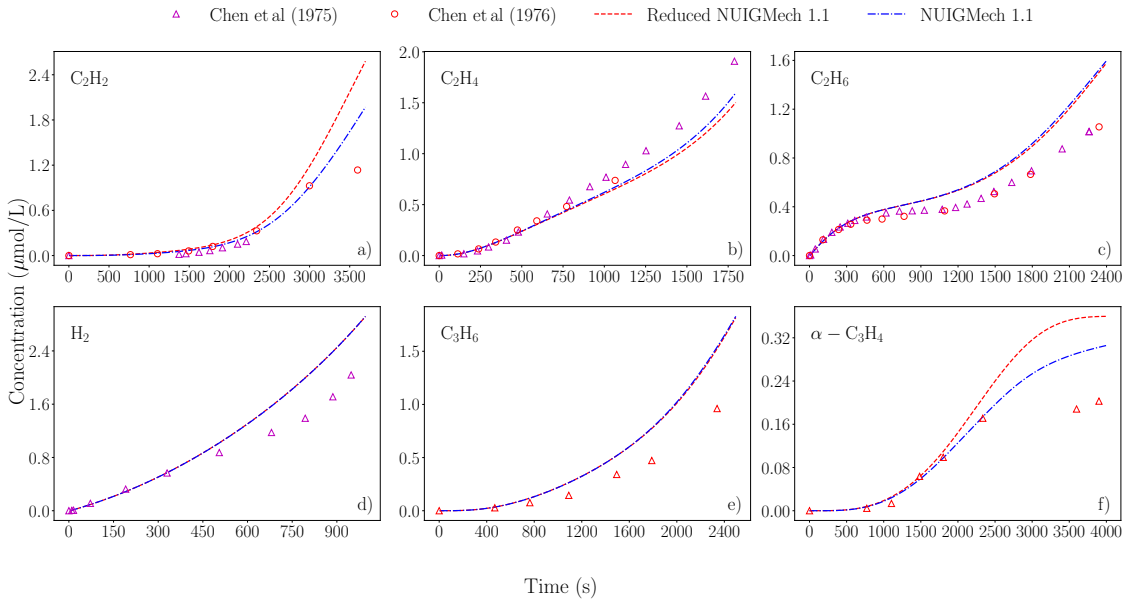

Figure 4.5: Comparison of the original and the reduced model predictions at 1038 K and 59 kPa for: a) acetylene; b) ethylene; c) ethane; d) hydrogen; e) propene; and f) allene.

dictions, however, the observed discrepancy between the two models was insignificant as methane decomposition had not started yet.

At 1292 K and 398.8 kPa, faster kinetics led to substantial initial methane decomposition and hydrogen production until steady-state condition were achieved inside the batch reactor. The reduced model accurately captured the experimentally observed steep methane decomposition and hydrogen formation in the first few seconds of the reaction. Additionally, the intermediate species profiles attained a peak in the initial decomposition stages and gradually declined followed by a steady-state profile. The reduced model captured the original models behaviour and reproduced the intermediate species profiles.

Based on the results above, we concluded that the reduced model inherits the methane decomposition chemistry for the target species considered and depicts a good agreement with the original model predictions at high-pressure.

4.1.2 Low-pressure (LP) reduction

Figure 4.5 compares the original and the reduced model predictions at 1038 K and 59 kPa [31]. The primary, secondary, and tertiary decomposition species were accurately tracked by the reduced mechanism for a residence time ranging from 0–4000 s. Additionally, ethane autocatalysis, usually observed at low-pressures [29, 31, 32, 92], was accurately captured by the reduced model. Except for allene (α-C_3H_4), the reduced model predictions were in good agreement with the intermediate species profiles. For the case of allene, as shown in Figure 4.5f, the profile was well captured for the first 2000 s, after which the reduced model showed an overprediction. It is hypothesized that the overprediction in allene concentration was due to missing elementary reactions in the reduced model leading to their formation. The reduced model predictions were further validated against the low-pressure experimental data given in references [33, 45] (see Appendix B.3 for additional comparison).

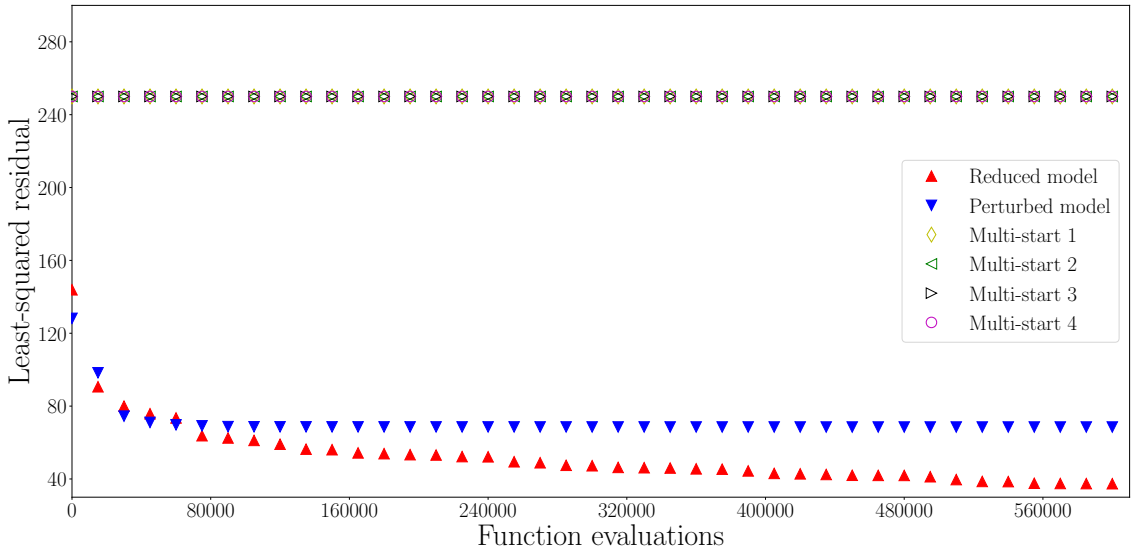

Figure 4.6: Reduction in least-square residual with an increase in the number of function evaluations using the reduced, perturbed, and random multi-start kinetic models as initial design variable sets. A Coliny pattern search method was used during the fitting process.

4.1.3 Discussion

Based on the results obtained from the original and reduced model, it is clear that within the error specified, the reduced model accurately reproduces the detailed model predictions for target species given in Section 2.2.2 and even for non-target species, such as C_6H_6, both at low and high-pressure methane pyrolysis conditions. Both mechanisms, however, struggled to accurately track low-temperature and high-pressure batch reactor experimental data [1]. To find a mechanism valid over a range of low- and high-pressure conditions, the reduced mechanism rate parameters, i.e., the pre-exponential factors and the activation energies of the gas-phase reactions, were fitted against methane and hydrogen mole fraction profiles obtained from the data by Tatum et al. [2] for 892 K, 1093 K, and 1292 K, and 398.8 kPa.

4.2 Rate parameter optimization

Figure 4.6 shows the least-square residual variation with function evaluations for the optimized set of rate parameters obtained using several rate parameter set as a starting guess. Using the original reduced model rate parameters, close to 60% residual reduction was achieved in the first 80,000 function evaluations. An overall 75% reduction in the residual was finally achieved. The multi-start random design sets were found to generate non-physical rate parameters and never converged to an optimal solution. Finally, when the original reduced model set of parameters were perturbed, the optimizer was able to achieve physical solution but the residual was 45% larger than the residual obtained using the base/reduced mechanism parameters as initial guess. This study highlights the complex nature of the least-square optimization problem, and shows that the final solution might be local. On the other hand, it also shows that using the reduced model parameters as an initial guess for the optimization leads to the most improved solution among the optimization cases considered.

It was observed that, although the optimization algorithm achieved a significantly lower value of the residual, some species exhibited an unrealistically rapid increase in concentration after the initial few seconds. To address the issue, a post-optimization sensitivity analysis was performed by independently changing the forward rate constant of each reaction by three orders of magnitude in each direction and comparing the initial change in species concentration with the experimental data. The kinetic parameters of the reactions showing a more realistic species concentration profile, i.e., CH_4, H_2, were modified and the updated mechanism was taken as the optimal solution.

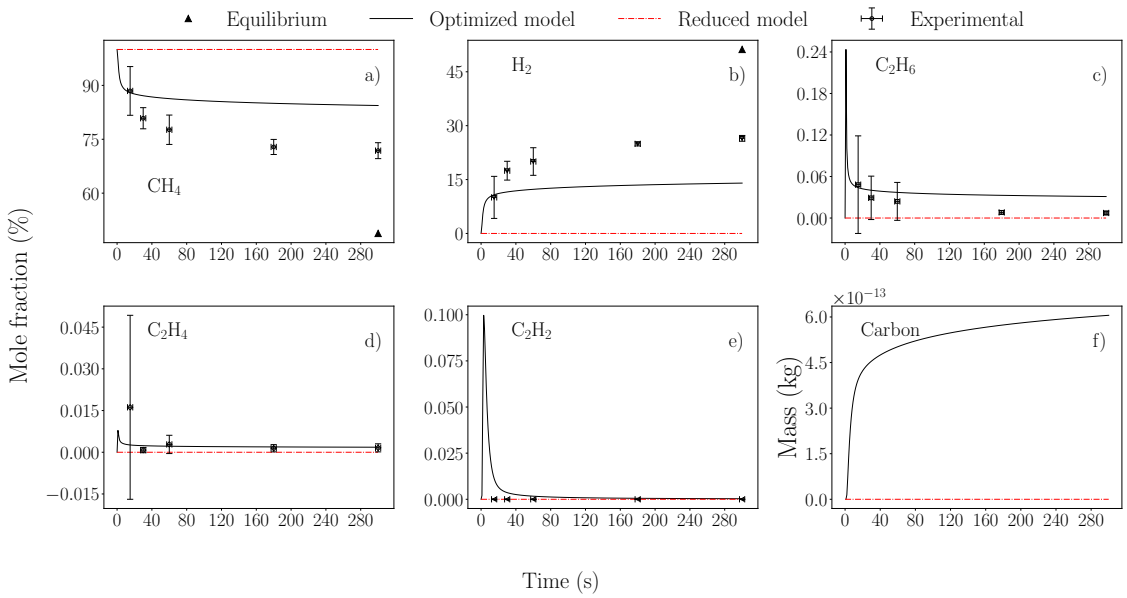

Figure 4.7: Comparison of the optimized and reduced model predictions against the experimental data at 892 K and 398.8 kPa for a) methane; b) hydrogen; c) ethane; d) ethylene; e) acetylene; and f) carbon. The triangle in CH_4 and H_2 indicates the mole fraction percentage predicted using the thermodynamic equation (1.2.1).

4.2.1 Model validation at above-atmospheric pressure

4.2.1.1 Low temperature

Figure 4.7 shows the experimental and predicted results obtained using the reduced and optimized model with carbon formation at 892 K and 398.8 kPa. A significant improvement in the species predictions was obtained with the optimal set of rate parameters. The major species predictions were found to be in better agreement with the experimental data than the original mechanism predictions although an underprediction in methane consumption and hydrogen formation was observed. Intermediate species, such as ethane and ethylene, attained a peak in the first few seconds (< 15 s) of the decomposition followed by a gradual decline in the mole fraction percentage. A similar behaviour was observed in experiments where ethane and acetylene concentrations peaked out and declined gradually with residence time [2]. This can be attributed to carbon formation via the acetylene pathway. In the initial decomposition stage, the concentrations of primary decomposed species, such as methane, ethane,

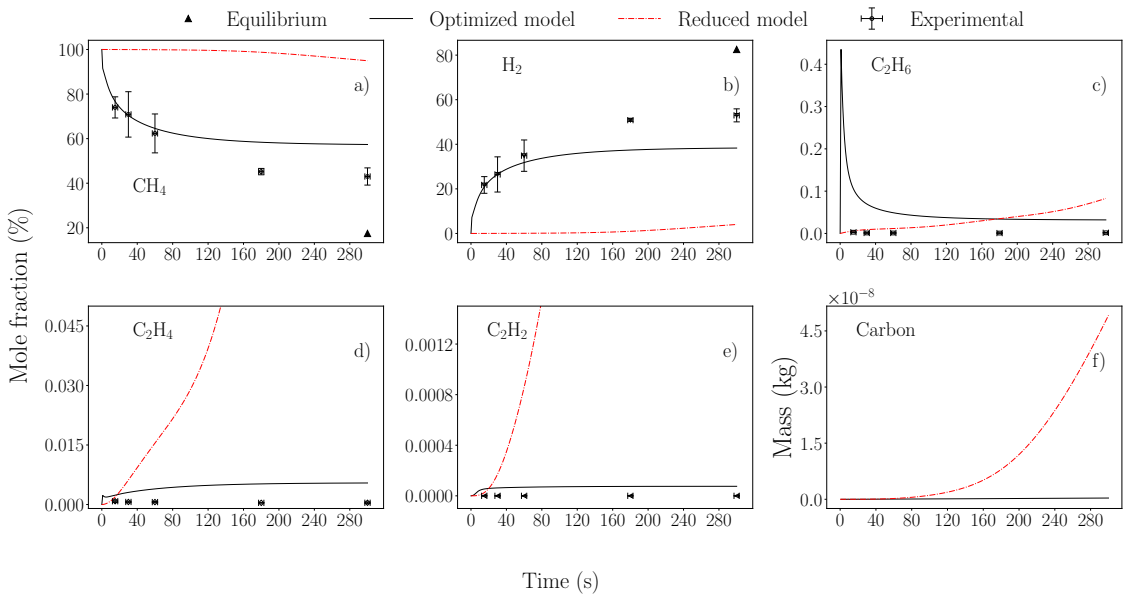

Figure 4.8: Comparison of the optimized and reduced model predictions against the experimental data at 1093 K and 398.8 kPa for a) methane; b) hydrogen; c) ethane; d) ethylene; e) acetylene; and f) carbon. The triangle in CH_4 and H_2 indicates the mole fraction percentage predicted using the thermodynamic equation (1.2.1).

and ethylene, are high, thereby generating large amounts of acetylene. The increase in acetylene formation was compensated by a sharp decrease in ethane and ethylene mole fraction percentages, after which the decomposition chemistry inside the reactor becomes slow and the intermediate species profiles attain a steady-state value. Based on the results, it can be said that the fitted model can accurately track methane and hydrogen mole fractions, and capture the physical phenomenon in ethane, ethylene, and acetylene mole fraction profiles under low-temperature conditions.

4.2.1.2 Intermediate temperature

Figure 4.8 shows the experimental data, reduced, and optimized model predictions at 1093 K and 398.8 kPa. While the reduced model struggled to accurately predict the major decomposition products, i.e., methane and hydrogen, the optimized model accurately tracks methane and hydrogen mole fraction profiles. For intermediate species, the optimized model predicts an initial peak in mole fractions followed by a decline in the mole fraction percentage, due to carbon formation. This behavior was

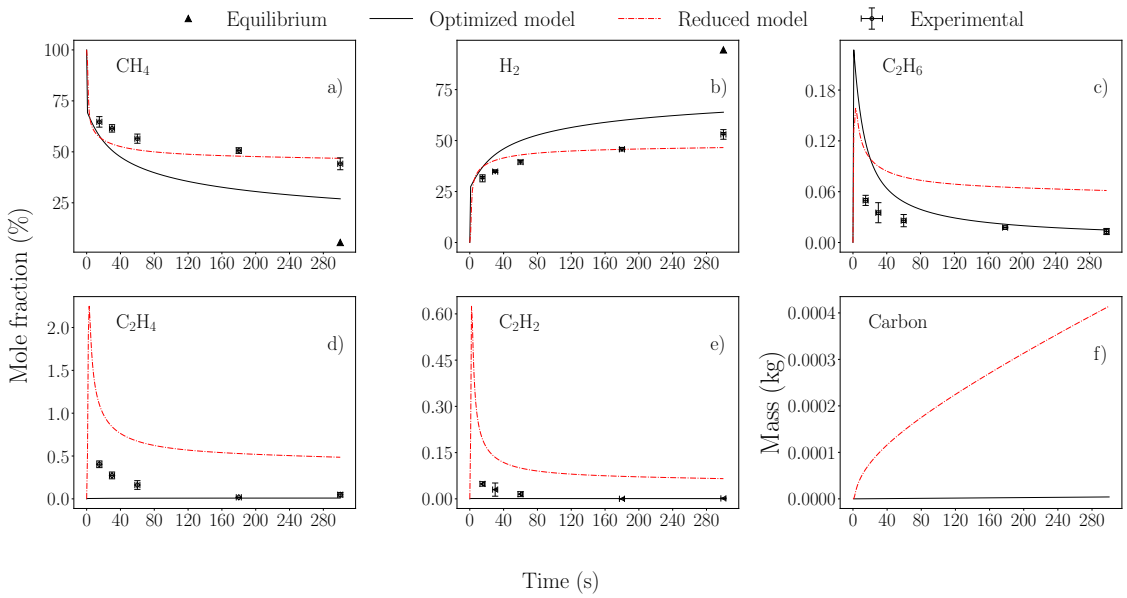

Figure 4.9: Comparison of the optimized and reduced model predictions against the experimental data at 1292 K and 398.8 kPa for a) methane; b) hydrogen; c) ethane; d) ethylene; e) acetylene; and f) carbon. The triangle in CH_4 and H_2 indicates the mole fraction percentage predicted using the thermodynamic equation (1.2.1).

overpredicted in the case of ethane, whereas for ethylene and acetylene, the optimized model predicted no formation. The optimized model predictions were thus consistent with the experimental data.

The optimized model shows less carbon formation compared to the reduced model predictions as the majority of the carbon gets transferred to heavier hydrocarbons, such as indene (C_9H_8). The carbon formation model had acetylene as the sink species and might be the reason for lesser carbon formation in the optimized model compared to the carbon formation from the reduced model.

4.2.1.3 High temperature

Figure 4.9 shows the experimental data, original, and optimized model predictions at 1292 K and 398.8 kPa. The optimized model overpredicts the experimental methane conversion. The optimal parameters can only achieve a compromise between all three temperatures. Figures 4.9a, 4.9b, and 4.9c show that at high-temperature and high-pressure, the optimized mechanism predicts very fast methane decomposition result-

ing in a sharp rise in product concentrations in the first few seconds. Afterwards, the methane decomposition and hydrogen formation profiles attain steady-state conditions. Ethane concentration was better tracked by the optimized model compared to the reduced model. The ethylene and acetylene mole fraction profiles obtained from the optimized model underpredict the experimental concentrations due to accelerated heavier hydrocarbon formation. With the optimized model generating a large amount of PAHs, only a small amount of solid carbon was predicted compared to the reduced model predictions.

4.2.2 Model validation at low-pressure

4.2.2.1 Low temperature

Figures 4.10 and 4.11 show the optimized and reduced model predictions obtained at a temperature of 1038 K, and at pressures of 13 kPa and 59 kPa, respectively. Note that low pressure data was not used in the parameter estimation as the reduced model already provided accurate results and most reactions had independent low and high pressure-dependent rate parameters. Therefore, the aim is to make sure the optimized values did not introduce significant errors at low pressures. Figure 4.10 shows that, at 13 kPa, the optimized model is able to track the intermediate species observed during the experiments by Chen et al. [32], i.e., ethane and ethylene, even though the new parameters slightly overpredict ethane production. Figure 4.11, at 1038 K and 59 kPa, also shows the optimized model results agree with experiments with only a minor underprediction in ethylene and an overprediction in ethane observed after 300 s. The optimized model still followed the decomposition profiles under low-temperature and low-pressure with good accuracy.

4.2.2.2 Intermediate temperature

Figure 4.12 shows a comparison of the decomposition products [31] and the reduced and optimized model predictions at an intermediate temperature of 1103 K and at

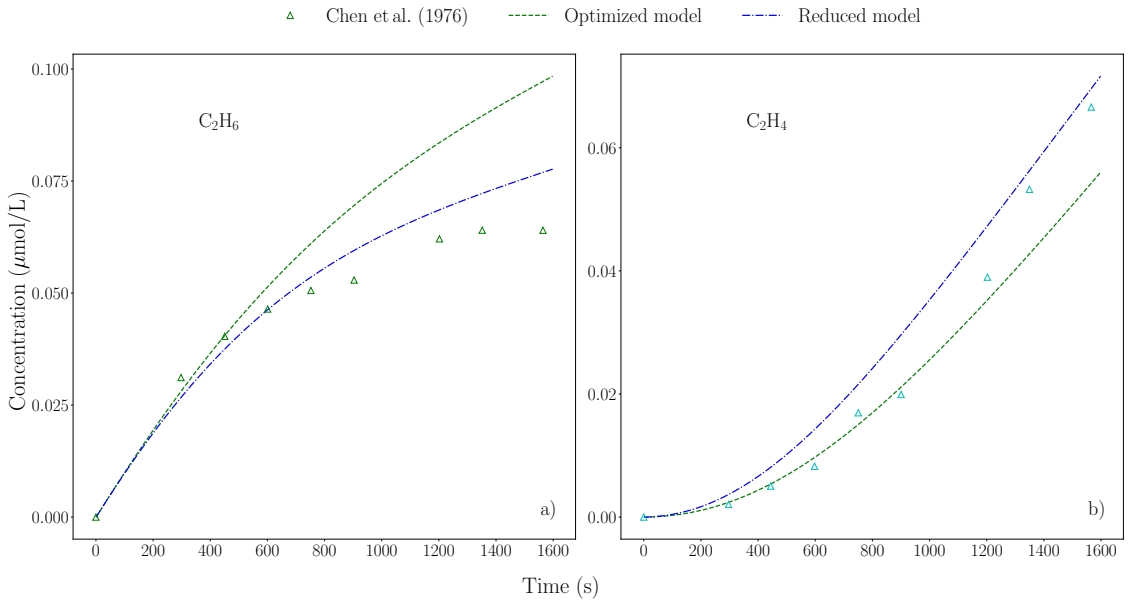

Figure 4.10: Comparison of the optimized model predictions against the experimental data at 1038 K and 13 kPa for a) ethane; and b) ethylene.

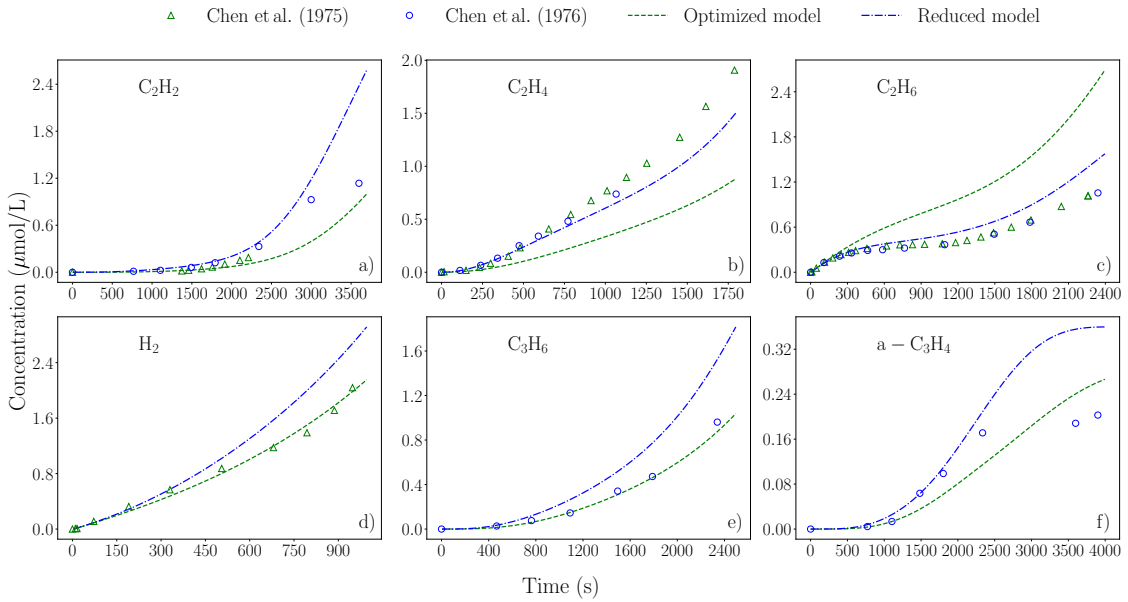

Figure 4.11: Comparison of the optimized model predictions against the experimental data at 1038 K and 59 kPa for a) acetylene; b) ethylene; c) ethane; d) hydrogen; e) propene; and f) allene.

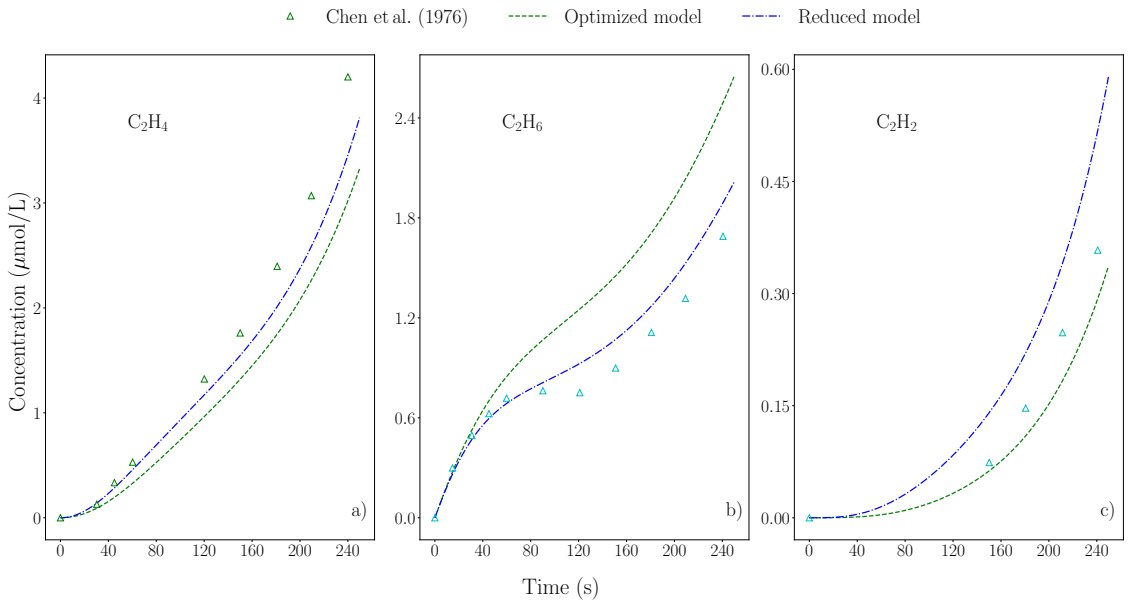

Figure 4.12: Comparison of the optimized model predictions against the experimental data at 1103 K and 59 kPa for a) ethylene; b) ethane; and c) acetylene.

a pressure of 59 kPa. The optimized model accurately predicts the transient profiles of ethylene and acetylene across the experimental time range. The model predictions for ethane agreed with the experimental data up to the first 60 s of the decomposition period, after which a minor overprediction was observed. The discrepancy observed was again attributed to the optimized model not being able to convert the available ethane in the reactor to ethylene leading to an overestimated concentration.

The optimized model was further tested against the batch reactor data of Arutyunov et al. [33]. Figure 4.13 shows the optimized and reduced model predictions for methane, hydrogen, acetylene, ethylene, and ethane at 1100 K and 58 kPa. The optimized model accurately predicted the major decomposition products, i.e., methane and hydrogen, for a residence time of 1800 s. The experimentally observed minor products were accurately captured by the reduced and fitted model up to the first 500 s, after which a slight overprediction was observed. The discrepancy was attributed to one of the following reasons: i) either there was carbon formation in the system which acted as a catalyst and the gas-phase model did not account for; or ii)

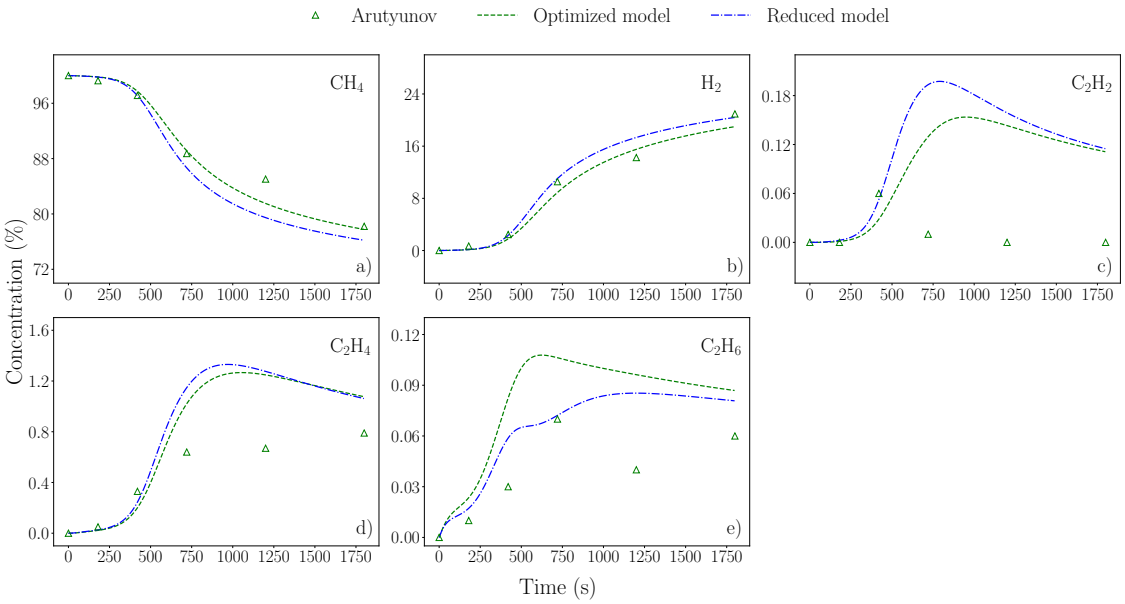

Figure 4.13: Comparison of the optimized model predictions against the experimental data from Arutyunov et al. [33] at 1100 K and 58 kPa for a) methane and hydrogen; b) acetylene; c) ethylene; and d) ethane.

as the uncertainties in the experimental data were not available, and the concentration (%) of acetylene, ethylene, and ethane were less than 1% in the product mixture, the experimental error might have contributed to the difference. With the inclusion of the carbon formation model at low pressures, the model generated similar profiles for acetylene, ethylene, and ethane. This meant that under low-pressure conditions, the reactor generated large quantities of higher-order hydrocarbons and less carbon as discussed earlier. The latter case of the model predictions within the experimental error range was, thus, taken as one of the contributing factors to the observed discrepancy.

4.2.2.3 High temperature

Figure 4.14 shows the optimized model predictions and the experimental data [33] for methane and hydrogen at a temperature of 1200 K and at pressures of 15 kPa and 93 kPa. In this case, the kinetics of methane decomposition are dominated by the temperature with pressure playing a minor role and the transient methane decomposition

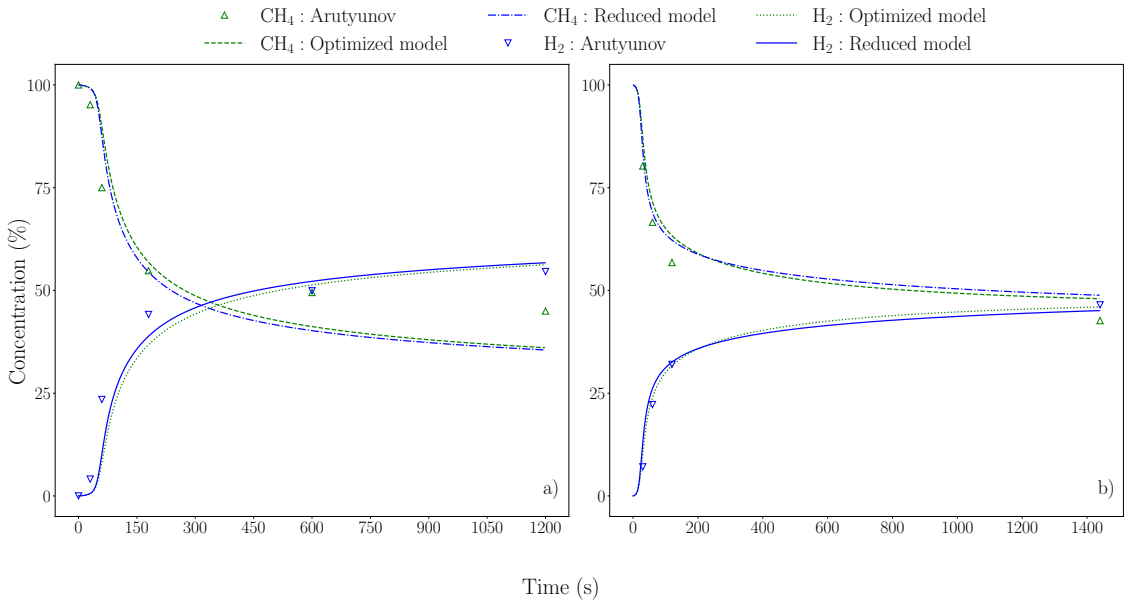

Figure 4.14: Comparison of the optimized model predictions for methane and hydrogen against the experimental data Arutyunov et al. [33] at 1200 K and at a) 15 kPa; and b) 93 kPa.

is accurately tracked by the optimized model at both pressures. Similarly, hydrogen concentration profiles at different pressures were in line with the experimental data points.

Figure 4.15 shows the model predictions and the experimental data for methane, hydrogen, acetylene, ethylene, and ethane at 1200 K and 58 kPa. The optimized model predictions for the major species observed, i.e., methane and hydrogen, also show good agreement with the experimental data. The model predictions for the minor species agreed with the experimental data up to the first peak observed, after which the model followed the experimental data with an offset. It was hypothesized that the observed discrepancy was due to the formation of carbon in the reactor under high-temperature conditions. The inclusion of carbon formation in the model, however, yielded the same concentration profiles for the minor species. Overall, the agreement of the optimized model predictions with the experimental data is good and can be considered as acceptable. Further validation of the optimized model at low-pressure conditions is shown in Appendix B.3.

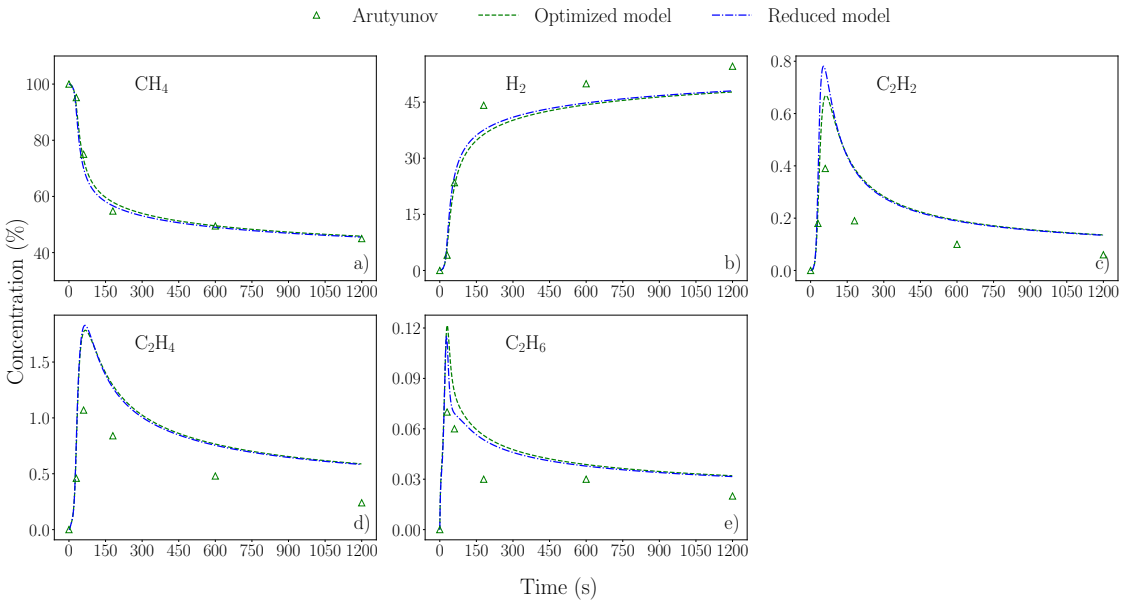

Figure 4.15: Comparison of the optimized model predictions against the experimental data at 1200 K and 58 kPa for a) methane; b) hydrogen; c) acetylene; d) ethylene; and e) ethane.

4.2.3 Discussion

Although, the optimized model predictions show good agreement with the experimentally available data in the literature up to 1100 K, a disagreement in ethylene and ethane concentration profiles was observed. The reason for this discrepancy was due to the modification of the rate parameters in the high-pressure limit during optimization for the fall-off reaction C_2H_4+ H (+M) <=> C_2H_5 (+M). During low-pressure decomposition of methane, the primary decomposition (up to 1000 s) products observed are hydrogen and ethane [31]. The ethane molecules formed undergo decomposition with hydrogen and form an ethyl radical and a hydrogen molecule via the reaction C_2H_6+ H <=> C_2H_5 + H_2. The forward rate constant for the fall-off reaction C_2H_4+ H <=> C_2H_5 (+M) was reduced during the optimization as the activation energy for the high-pressure limit was increased by the algorithm. To maintain the same value of the equilibrium constant, the backward rate was required to be reduced by a similar proportion. As a result, ethane molecules in the reactor could not convert to

ethyl radicals resulting in the overprediction after the primary stage. Similarly, due to a reduced backward rate constant, the formation of ethylene was not sufficient to accurately follow the experimental profile. The ethylene formation reaction was, in particular, found to be critical for accurately predicting methane decomposition and hydrogen formation at high-pressures. Hence, a slight discrepancy was incorporated in the optimized model for low-temperature, low-pressure conditions as a trade-off for the significant increase in accuracy at high-pressure.

4.3 Path flux analysis

To identify the critical reaction paths impacting the species concentrations, a path flux study of the reduced and optimized mechanisms was performed, and the carbon element flux was captured. The analysis also gave an idea of how additional reactions, if any, were activated in the optimized model. The detailed methodology for the analysis performed is given by Punia et al. [1].

Figure 4.16 shows the carbon element flux transfer between species via different reaction pathways at 892 K and 398.8 kPa obtained using the reduced and optimized mechanisms. An increased kinetic activity was observed using the optimized set of kinetic parameters. The formation of propyl radical (n-C_3H_7) from isopropyl radical (i-C_3H_7) showed the largest transfer of carbon. The propyl radical, in turn, contributed to the formation of ethylene (C_2H_4) and active methyl radicals (CH_3). The methyl radicals contributed to increased consumption of methane and propene (C_3H_6) formation. The ethylene molecules assisted in acetylene formation, thereby opening a path to PAHs, solid carbon formation and H_2, i.e., the production of C_2H_2. Acetylene and propene were also found to aid aromatic formation via the formation of C_5H_6 rings. The altered rate parameters activated the above-mentioned reaction paths and thus contributed to a rise in methane decomposition.

Figure 4.17 shows the transfer of the carbon element flux across different species at 1093 K and 398.8 K using the reduced and fitted reaction models. The most crit-

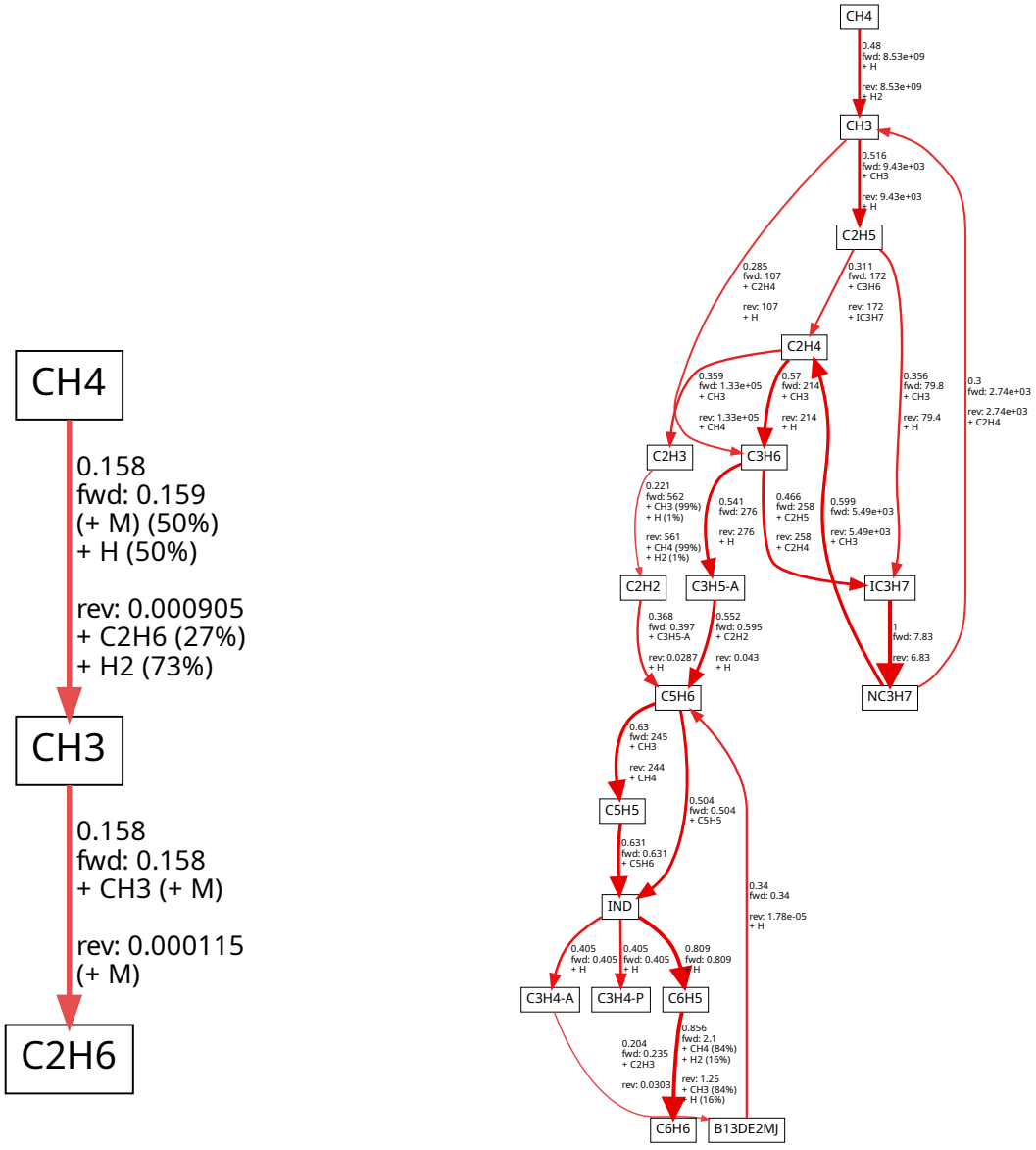

(a) Reduced model (b) Optimized model

Figure 4.16: Reaction flux diagram for carbon element at 892 K and 398.8 kPa using the reduced and the optimized kinetic models at 100 s. 'fwd' and 'rev' are the net forward and reverse carbon element fluxes, respectively. The number above the 'fwd' flux represents the net flux as given by Punia et al. [1]. The flux diagram was obtained using a threshold limit of 0.1 and 0.2 for the reduced and fitted reaction models, respectively.

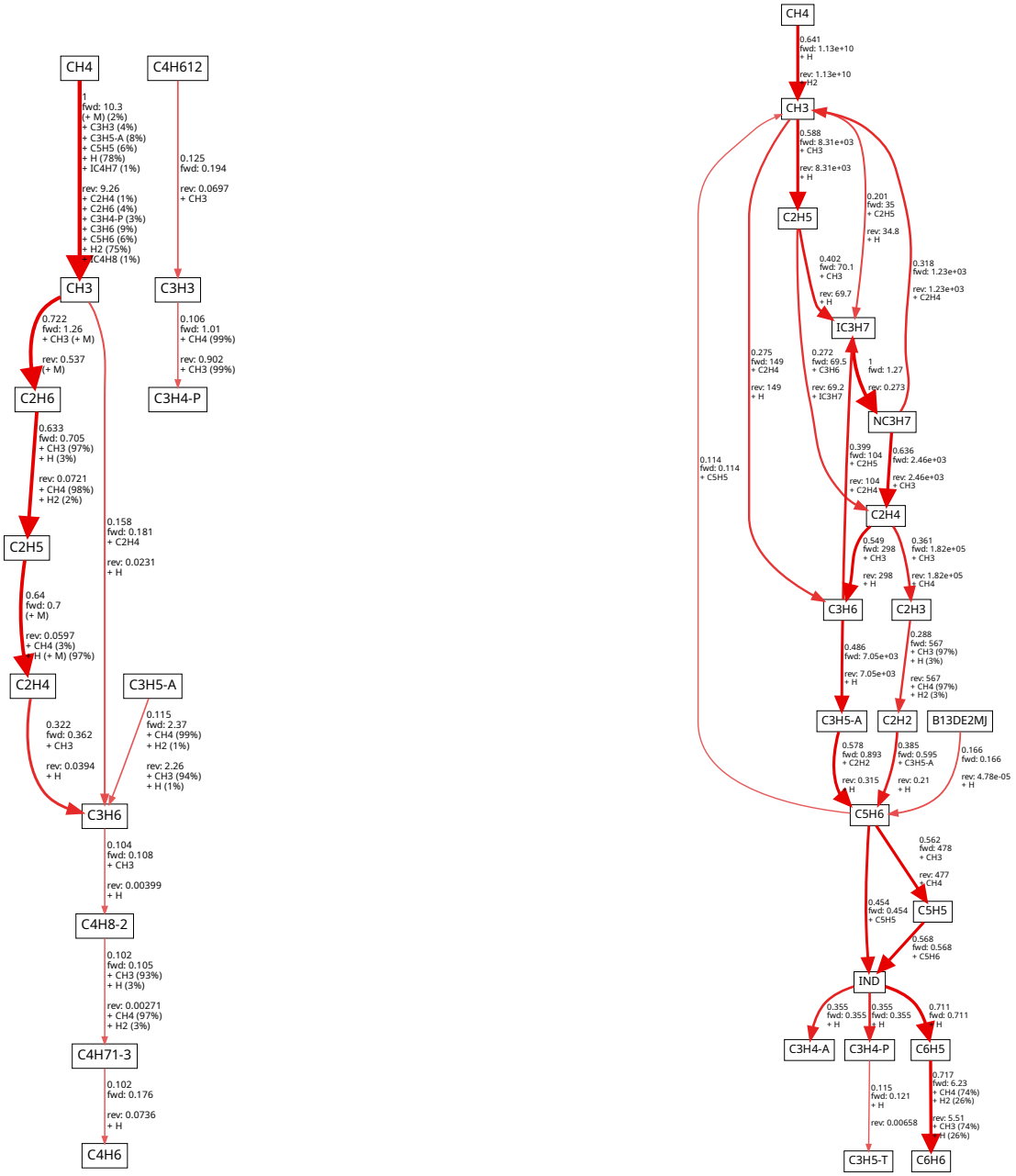

(a) Reduced model (b) Optimized model

Figure 4.17: Reaction flux diagram for carbon element at 1093 K and 398.8 kPa using the reduced and the optimized kinetic models at 100 s. 'fwd' and 'rev' are the net forward and reverse carbon element fluxes, respectively. The number above the 'fwd' flux represents the net flux as given by Punia et al. [1].

ical reaction in the reduced model was $CH_4 <=> CH_3 + H$ and the majority of the carbon element transfer occurred via the following path: $CH_3 \rightarrow C_2H_6 \rightarrow C_2H_5 \rightarrow C_2H_4 \rightarrow C_3H_6$ and as the carbon flux transfer was limited to the primary and the secondary hydrocarbons, the decomposition was underpredicted. Additionally, the flux magnitude was not sufficient to contribute to the formation of acetylene, i.e. the carbon-forming species. With the fitted set of rate parameters, i.e., Figure 4.17b, the primary decomposition pathway was bypassed and additional reaction pathways were created to increase decomposition. The carbon flux transfer from the optimized model bypassed C_2H_6 formation from CH_3 owing to the attainment of steady-state at a residence time of 100 s. An additional pathway, i.e., $C_2H_5 \rightarrow IC_3H_7 \rightarrow NC_3H_7 \rightarrow C_2H_4 \rightarrow C_2H_3 \rightarrow C_2H_2$, resulted in an increase in the formation of ethylene and contributed to the formation of acetylene and heavier hydrocarbons under high-pressure conditions. The formation of active CH_3 radicals from linear hydrocarbons, such as NC_3H_7, and aromatic hydrocarbons, such as C_5H_6, ensured that the decomposition of methane is continuous.

Figure 4.18 shows the carbon element flux transfer across different species at 1292 K and 398.8 K using the reduced and fitted kinetic models at 100 s. Based on the fluxes obtained from the reduced model, the majority of the flux transfer shifted to heavier hydrocarbons. The hydrogenation of indene (C_9H_8) forming a phenyl radical (C_6H_5) was the most critical reaction. One of the reasons for the shift in the decomposition kinetics to heavier hydrocarbons is due to the attainment of steady-state profiles for different species. On the other hand, the flux diagram obtained from the fitted kinetic model shows that, even with a coarse threshold limit, the reactions responsible for the initial dissociation of methane exist under high-pressure conditions. Due to the continuous decomposition of methane to various intermediate products, the fitted model slightly overpredicted methane and hydrogen mole fraction profiles (Figure 4.9).

Based on the results obtained from the path flux analysis, it can be concluded that

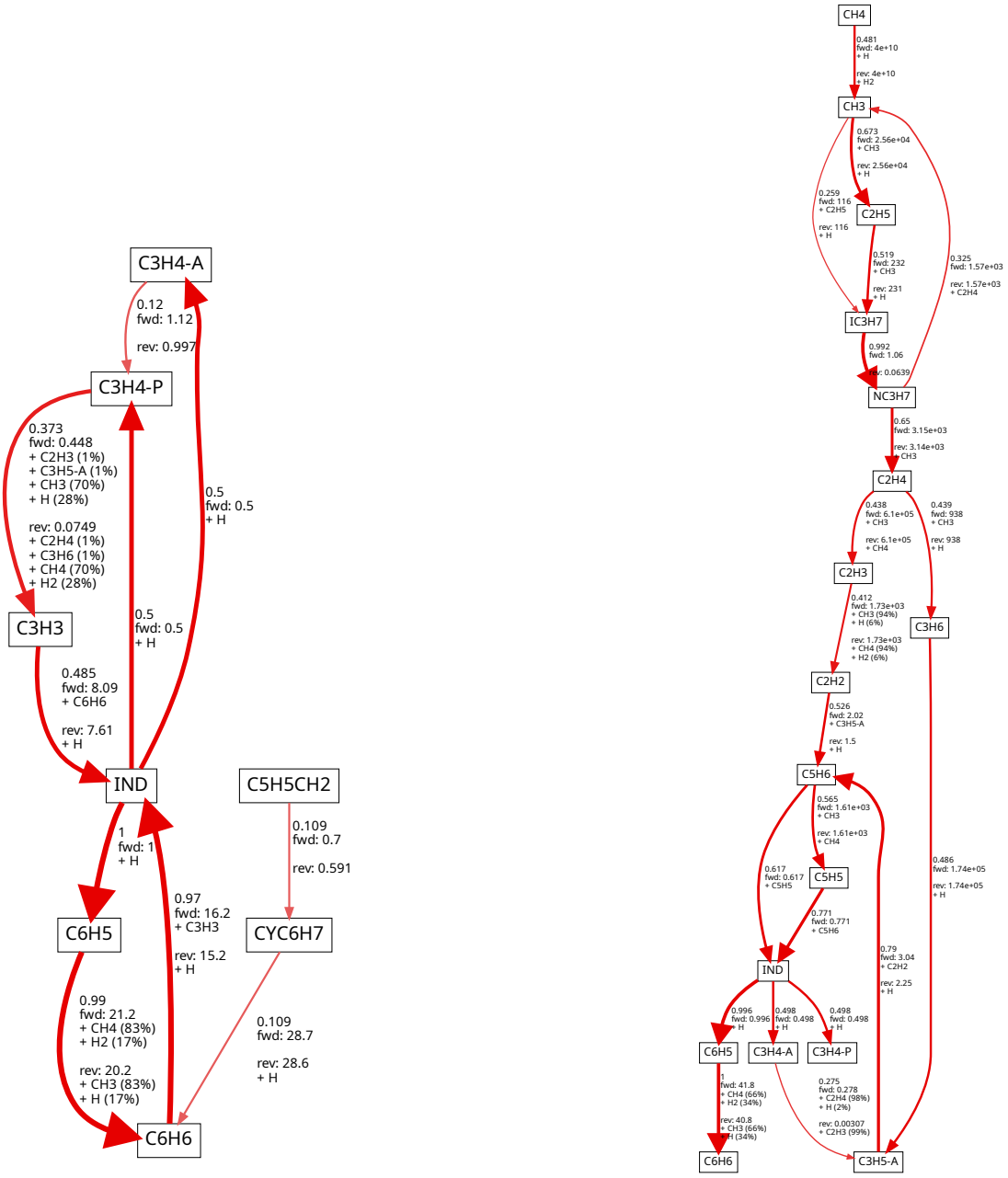

(a) Reduced model

(b) Optimized model

Figure 4.18: Reaction flux diagram for carbon element at 1292 K and 398.8 kPa using the reduced and the optimized kinetic models at 100 s. 'fwd' and 'rev' are the net forward and reverse carbon element fluxes, respectively. The number above the 'fwd' flux represents the net flux as given by Punia et al. [1]. The flux diagram was obtained using a threshold limit of 0.1 and 0.25 for the reduced and fitted reaction models, respectively.

the altered set of reaction rate parameters, especially under low-temperature conditions of 892 K and 1093 K, drove up methane decomposition and hydrogen formation by activating additional reaction pathways. The movement of carbon flux starting from methane to heavier hydrocarbons increased rapidly to accurately capture the thermal decomposition.

4.3.1 Use of non-similar threshold values for the path flux analysis

The threshold values for the path flux analysis for the reduced and optimized mechanisms were intentionally kept different. One of the reasons was that the reduced mechanism showed limited carbon flux transfer activity for a particular value of the threshold. Due to this, the flux diagram contained fewer species thereby making the analysis limited. The flux diagram obtained using the optimized mechanism shows significant flux transfer activity even with a coarse threshold value. Hence, in the present study, a refined threshold value was used for the reduced mechanism, whereas a coarser value was used while generating the flux diagram using the optimized reaction mechanism.

Chapter 5

Carbon formation

In the previous two chapters, a single-step sink reaction, given in Equation (2.1.16), has been assumed to contribute to the formation in the form of solid carbon. However, carbon is produced in the form of soot. The formation of soot particles is governed by different sub-processes, as discussed in Chapters 1 and 2, and need to be accounted for. Additionally, the single-step reaction model is not able to provide information regarding the produced soot particle, such as the number concentration, number of primary particles per aggregate, primary particle diameter, particle mobility diameter, and particle gyration diameter. Hence, a 0D monodisperse population balance method was coupled to the batch reactor model in Chapter 4 to estimate soot formation during pyrolysis and to track the particle concentration and its morphology over time. The soot formation model was adopted from the work by Kholghy et al. [151] which was initially proposed to study soot formation for the combustion conditions. The particle growth model, however, can be used for different decomposition conditions and, hence, was tested in this work for the pyrolysis conditions.

5.1 Validation against the benchmark results

The soot model was developed in stages targeting individual sub-physics, such as coagulation, surface growth, and aggregation. Before coupling with the gas-phase model, the sub-models implemented were first independently validated against the

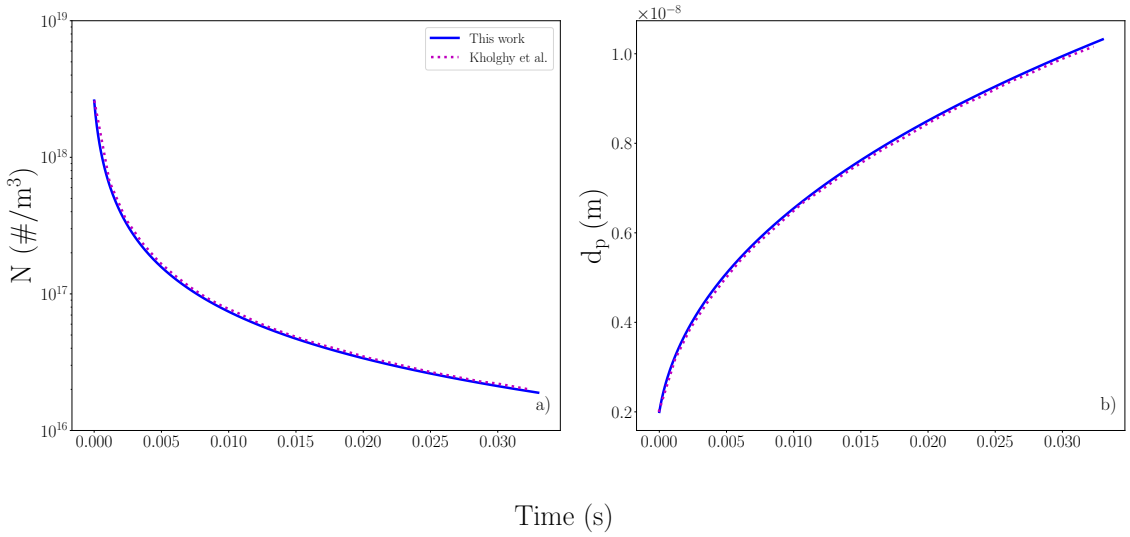

Figure 5.1: Aggregate number density (left) and particle diameter (right) comparison between the model implemented in this work and data reproduced from Kholghy et al. [151] for pure coagulation at 1830 K and 101325 Pa.

model results from Kholghy et al. [151] for the following cases discussed below.

5.1.1 Pure coagulation

In pure coagulation, two particles of same size collide, fuse together, and generate a single particle with a diameter bigger than the colliding particles. The monodisperse population balance model in this case was validated against the results by Kholghy et al. [151] for an initial particle concentration of 2.6 $\times 10^{18}$ (#/m^3) and an initial particle diameter of 2 nm. To simulate the model, only the particle number density, i.e., N, was solved using Equation (2.2.23). Therefore, the mobility diameter (d_m) remained the same as the particle diameter (the number of primary particles in an aggregate (n_p) had a value of 1). Figure 5.1 shows the change in the number density of the aggregate (sphere in this case) and the particle diameter with time. With an increase in the particle size the particle number density decreases. The model implemented accurately follows the particle concentration and particle diameter profiles for the data obtained from the literature.

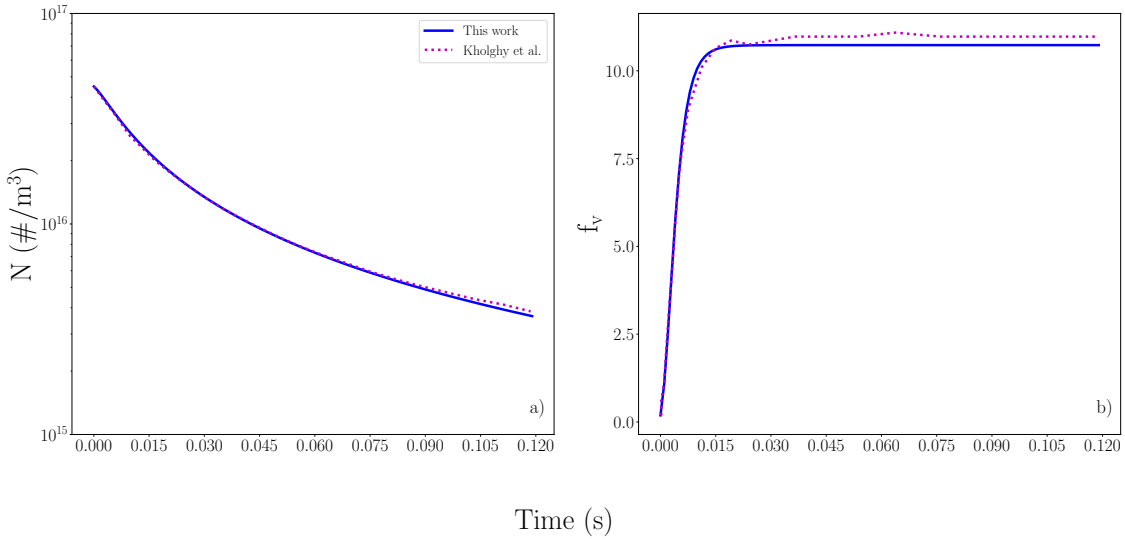

Figure 5.2: Aggregate number density (left) and soot volume fraction (right) comparison between the model implemented in this work and data reproduced from Kholghy et al. [151] for simultaneous coagulation and surface growth at 1830 K and 101325 Pa.

5.1.2 Coagulation and surface growth

Once the coagulation model was validated, a soot surface growth sub-model was added. For the case of coagulation and surface growth, the agglomerates were assumed to be perfect spheres after collision and surface growth, and the number of primary particles per aggregate (n_p) still has a value of 1. For this case, a total of three variables, i.e., aggregate number density (N), total carbon molar (C_{tot}), and mass of a single aggregate (m_{ag}), were solved in time. Soot with a primary particle diameter of 2 nm with an initial concentration of 4.5 $\times 10^{16}$ (#/m^3) at 1830 K and 101.325 kPa was allowed to grow due to coagulation and surface growth. Figure 5.2 shows the particle number density and soot volume fraction over time. It can be seen that the model accurately captures the data reported by Kholghy et al. [151] for pure coagulation and surface growth.

5.1.3 Aggregation/agglomeration and surface growth

Generally, as the soot particles grow in size, they collide and stick to each other due to the Van der Waals force instead of fusing together. Hence, to account for the sticking of the particles, the soot model was further improved and a soot aggregation/agglomeration sub-model was coupled with surface growth instead of soot coagulation. Note that the primary particles are in point contact in this case and the increase in the primary particle size is only due to the surface growth. To predict the particle evolution in time, in addition to the previous three variables, total particle surface area was solved for such that the governing equation contain a total of four variables, i.e., N, C_{tot}, A_{tot}, and m_{ag}. Soot with a primary particle diameter of 2 nm with an initial concentration of 4.5 $\times 10^{16}$ (#/m^3) at 1830 K and 101.325 kPa was allowed to agglomerate and grow due to surface growth. Figure 5.3 shows the evolution of the aggregate number density, primary particles per aggregate, primary particle diameter, and particle mobility diameter over time and compares the results to those from Khology et al. [151]. The model implemented accurately tracks the data reproduced from the Kholghy et al. [151]'s model. The particle concentration attains a steady-state value after around 9 ms. The primary particle diameter grows due to the surface growth for the first 10 ms, after which the primary particles do not grow in size. This is in agreement with the Kholghy et al. [151]'s model assumption that particle nucleation and surface growth acts for a very short duration of time. In the absence of surface growth, the particles stick to each other and the number of primary particles per aggregate and the mobility diameter of the particle increases. Overall, the soot model implementation is accurate and can be further used to predict the particle formation during methane pyrolysis.

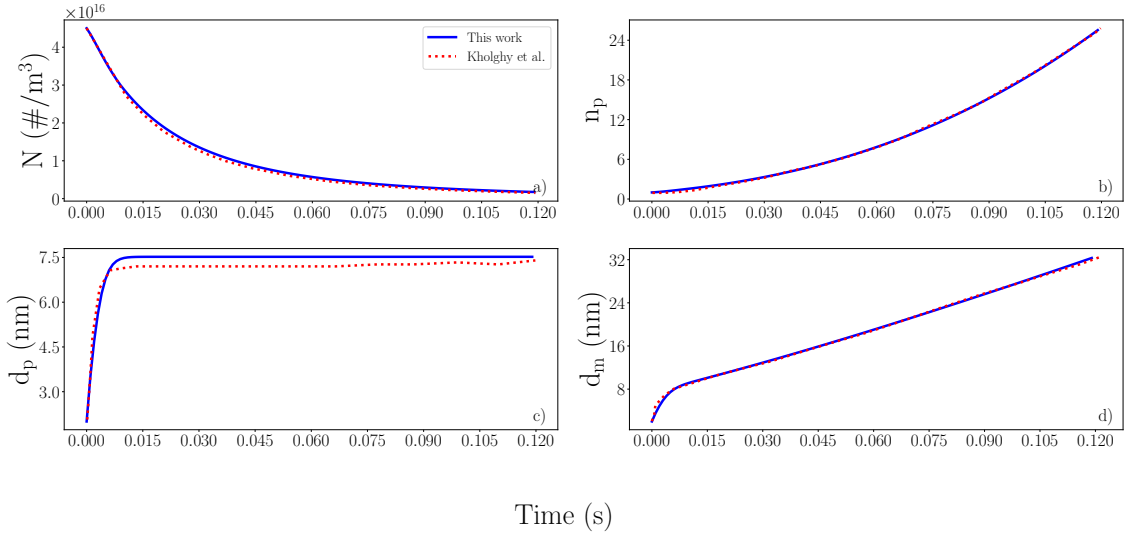

Figure 5.3: Comparison of a) the aggregate number density; b) the number of primary particles per aggregate; c) primary particle diameter; and d) the mobility diameter with the data reproduced from Kholghy et al. [151]'s model for simultaneous aggregation/agglomeration and surface growth at 1830 K and 101325 Pa in a premixed ethylene flame.

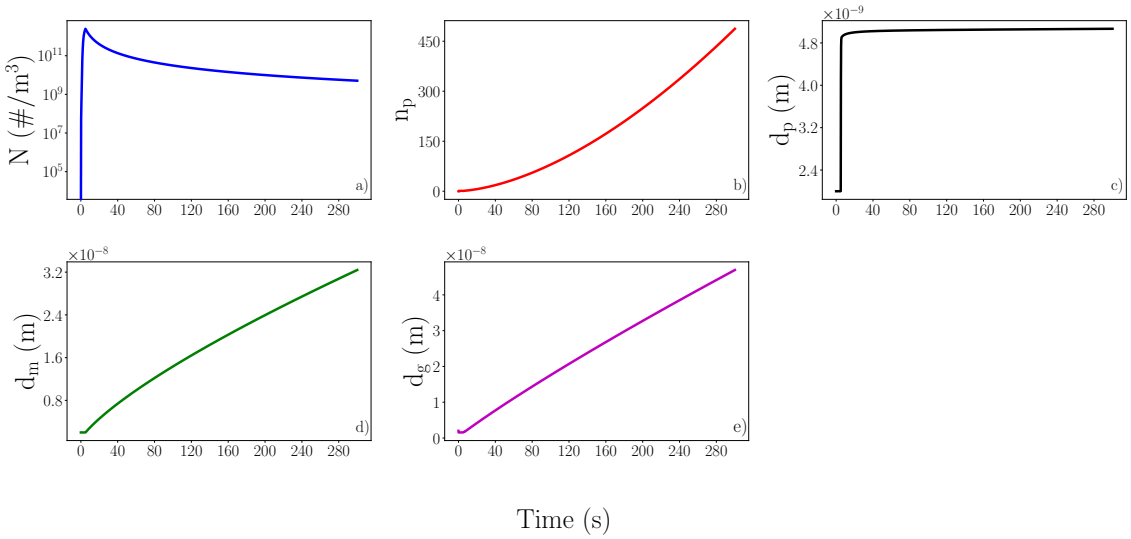

Figure 5.4: Transient evolution of a) soot particle number density; b) the number of primary particles per aggregate; c) soot primary particle diameter; d) soot particle mobility diameter; and e) soot particle gyration diameter, at 892 K and 398.8 kPa.

5.2 Soot formation during methane pyrolysis

5.2.1 Low temperature

Figure 5.4 shows the transient evolution of the particle number density (N), number of primary particles per aggregate (n_{p}), primary particle diameter (d_{p}), particle mobility diameter (d_{m}), and particle gyration diameter (d_{g}) for the soot generated during methane pyrolysis at 892 K and 398.8 kPa. The particle concentration density increased during the nucleation period for the first five seconds and reached a value of about 10^{12} particles, after which soot aggregation and surface growth from acetylene dominated. The number of primary particle per aggregate stayed constant for the nucleation period after which its value increased over time due to increasing aggregate size, and the final soot aggregate contained around 450 primary particles. With an aggregate like structure, the particle mobility and gyration diameters also increased to an approximate value of 32 nm and 48 nm, respectively. The primary particle diameter, on the other hand, attained a steady-state value of approximately 4.8 nm and did not grow further. The growth of the primary particles was inhibited after around 10 s as the surface growth phenomenon acted for a very short period of time. Acetylene's concentration, the species responsible for surface growth, at 892 K and 398.8 kPa, was so low that its contribution to the particle growth was negligible after around 40 s. Hence, the primary particle diameter did not change, whereas the aggregate mobility diameter increased with respect to time due to the sticking of the particles. A note that the small decline in the gyration diameter just after the nucleation period is due to the scaling law [174] used to calculate the gyration diameter. Till the nucleation period, all the particles are assumed to be of 2 nm and the mobility diameter remains unchanged because the number of primary particles (n_{p}) has a value of 1. Hence, the value of the gyration diameter when calculated using the expression, $\frac{d_m}{1.29}$, becomes slightly less than the primary particle diameter for the fraction of seconds after the nucleation period.

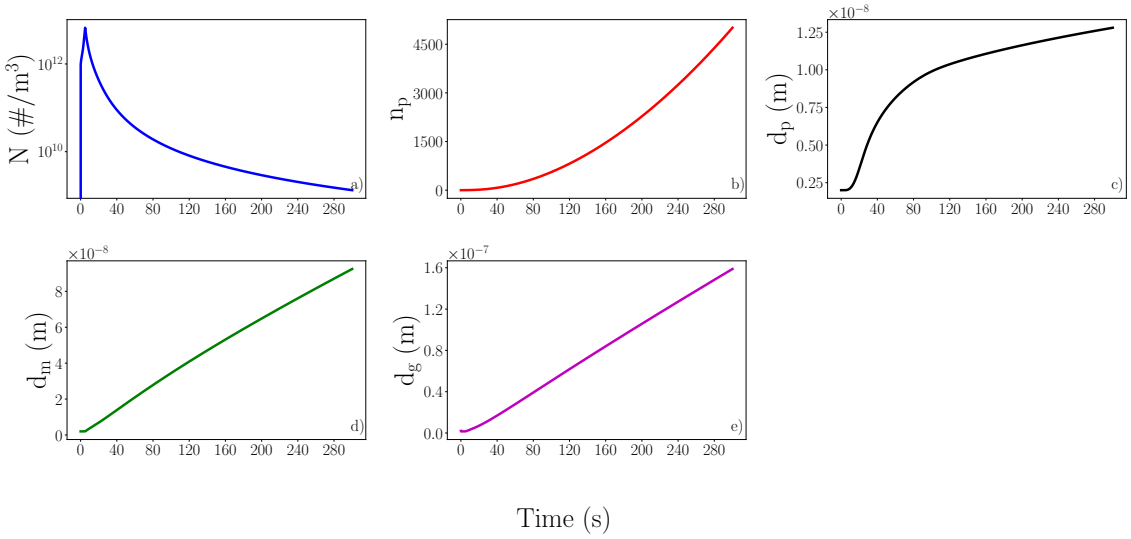

Figure 5.5: Transient evolution of a) soot particle number density; b) the number of primary particles per aggregate; c) soot primary particle diameter; d) soot particle mobility diameter; and e) soot particle gyration diameter, at 1093 K and 398.8 kPa.

5.2.2 Intermediate temperature

Figure 5.5 shows the numerical predictions for the particle number density (N), number of primary particles per aggregate (n_{p}), primary particle diameter (d_{p}), particle mobility diameter (d_{m}), and particle gyration diameter (d_{g}) over time for the soot generated at 1093 K and 398.8 kPa. With an increase in the reactor temperature, the particle concentration reaches a value close to 10^{13} due to soot nucleation. After the nucleation period, the increase in the primary particle size leads to a decrease in the particle number concentration and approaches a steady-state value at the end of the reaction with a diameter of 12.5 nm. With a 200 K increase in temperature, the primary particle size increases by a factor of 4 compared to the particle size at 892 K. The increase in the primary particle diameter is due to acetylene getting consumed at the surface of the particle. Figure 4.8 shows that acetylene attains a steady-state concentration at the very start of the reaction, however when the surface growth model is included, the concentration of acetylene decreases rapidly and reaches a mole fraction (%) value close to zero after around 100 s. The effect of the surface growth model on

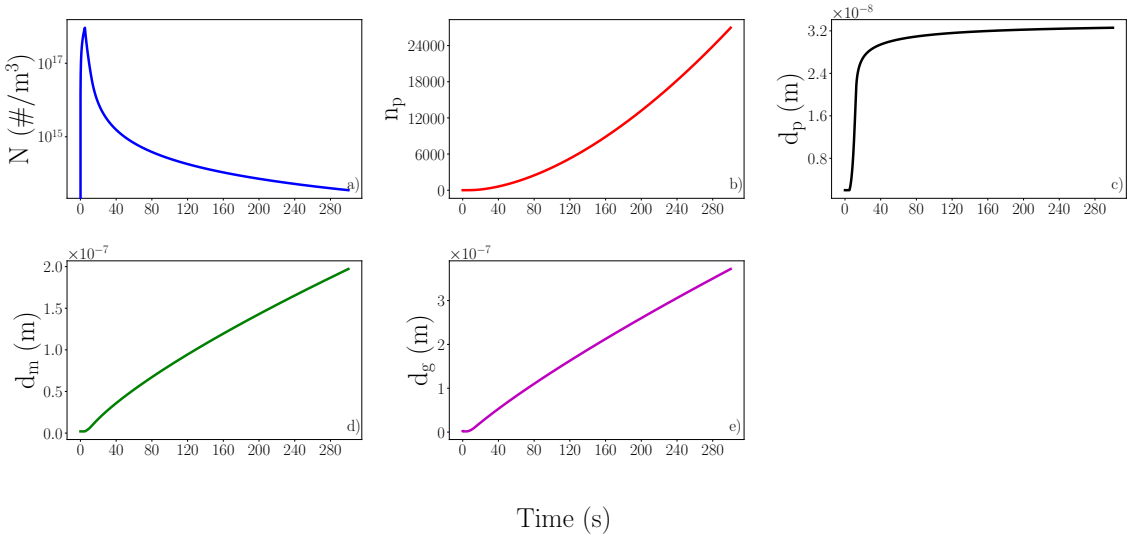

Figure 5.6: Transient evolution of a) soot particle number density; b) the number of primary particles per aggregate; c) soot primary particle diameter; d) soot particle mobility diameter; and e) soot particle gyration diameter, at 1292 K and 398.8 kPa.

acetylene consumption is discussed later in this chapter.

5.2.3 High temperature

Figure 5.6 shows the numerical predictions for the particle number density (N), number of primary particles per aggregate (n_p), primary particle diameter (d_p), particle mobility diameter (d_m), and particle gyration diameter (d_g) over time for the soot generated at 1292 K and 398.8 kPa. At elevated temperatures, the particles consumption rate is fast as the majority of the primary particles aggregate and decrease the overall number density. Simultaneously, the surface growth phenomenon is dominant for the ten seconds after nucleation. The primary particle diameter attains a steady-state value of approximately 32 nm, an increase by a factor of 7 and 2.5 compared to the primary particle diameters at 892 K and 1093 K, respectively. After around 15 s, soot aggregation dominates the change in particle number density and particle morphology as the number of primary particles and particle mobility diameter depend on it in the absence of surface growth. Acetylene, at this temperature, gets quickly

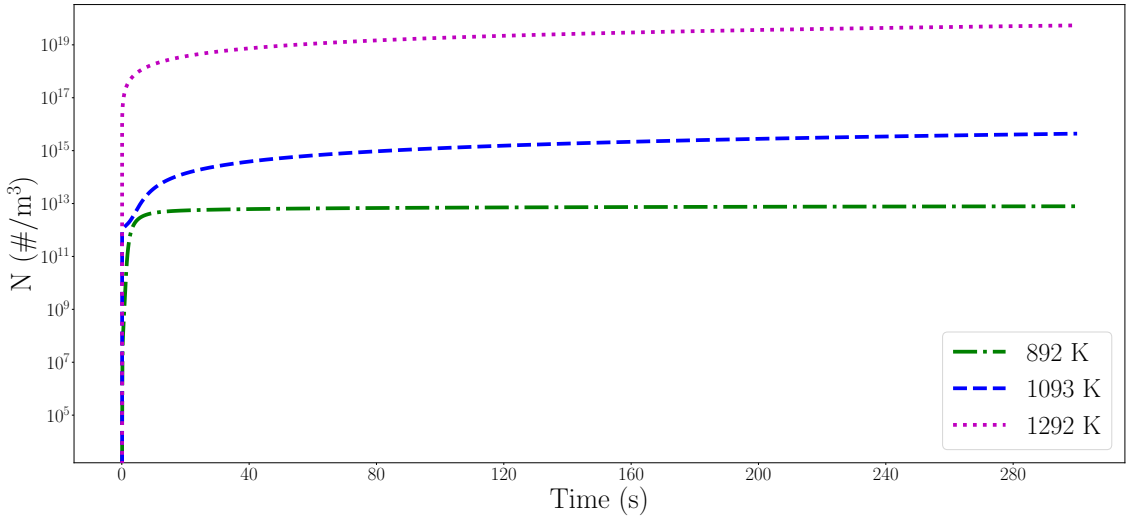

Figure 5.7: Transient evolution of soot particle number density for particle nucleation at 892 K, 1093 K, and 1292 K, and at 398.8 kPa.

consumed and the model shows that no acetylene is left in the reactor after around 15 s.

The soot generated during methane pyrolysis inside the batch was predicted using the model in this work. As soot particles continuously evolve in time, experimentally capturing them was difficult, especially at the temperatures studied. Therefore, the soot model in the present study was not validated. However, in one of our upcoming works where the experimental data for soot is collected in a flow reactor, the gas and solid-phase model will be validated against the data obtained.

5.2.4 Discussion

Based on the results predicted, a number of studies were performed to identify: a) the residence time up to which the effects of the nucleation exist; b) the effect of particle nucleation for different residence times on soot formation; c) the change in the mass consumption of acetylene due to the surface growth model; and d) the structure of the soot particles, at different temperatures, with the help of particle's mobility and gyration diameters.

5.2.4.1 Particle nucleation

As acetylene concentration was different at different temperatures, it was important to test the contribution of nucleation affecting the particle concentration over time. Hence, the restriction that nucleation happens only in the first 5 s was removed and transient evolution of pure soot nucleation from acetylene was predicted at different temperatures. Figure 5.7 shows the aggregate number density vs time for soot nucleation at 892 K, 1093 K, and 1292 K, and 398.8 kPa. It can be seen that temperature plays a significant role in the particle nucleation with higher temperature leading to larger number of particles nucleating. The nucleation process, however, is fast, and is active only for a very short duration of time. At the start of the reaction, due to a fast growth of acetylene in the gas-phase, particles form inside the reactor at a very fast rate. However, with increase in time, acetylene concentration decreases and the number of particles, in the absence of soot aggregation, attain a steady-state value after approximately the first 20 s at all temperatures. After this time period, nucleation virtually ceases to exist. Additionally, if the nucleation was allowed to happen for the whole of the decomposition time while considering soot aggregation and surface growth, it would not be possible to assume a monodisperse model at a particular time as the nucleating particle would have a size of 2 nm, whereas the particles due to aggregation and surface growth would have a different primary particle diameter.

5.2.4.2 Effect of particle nucleation for different residence times on soot formation

After studying pure nucleation, the transient effect of soot nucleation for different residence times on soot formation was investigated. Figure 5.8 shows the evolution of the aggregate number density, number of primary particles per aggregate, primary particle diameter, particle mobility diameter, and particle gyration diameter at 892 K and 398.8 kPa assuming soot nucleation happens for a residence time of 0.5 s, 1 s, 3 s,

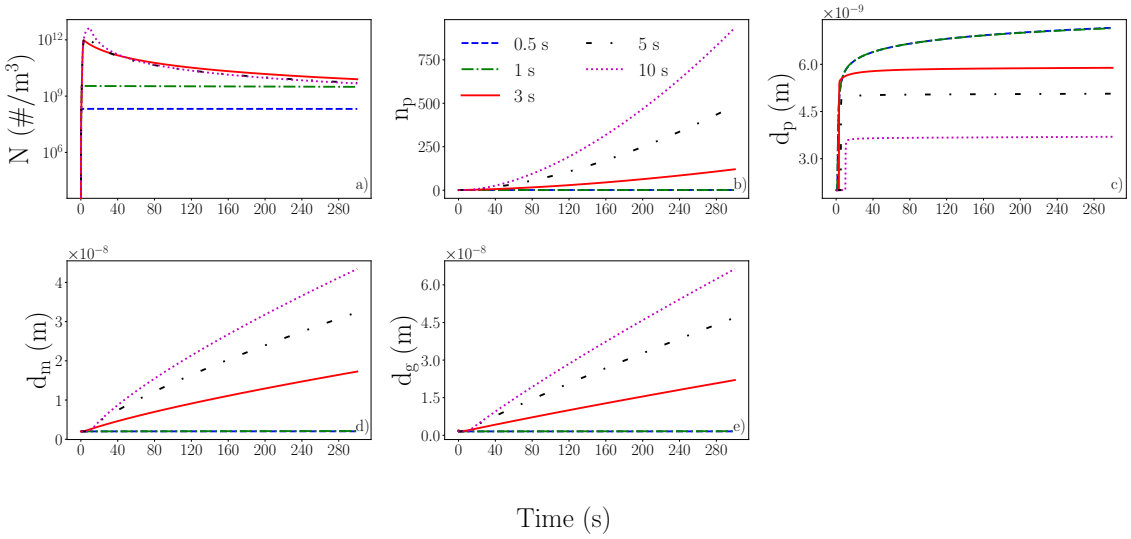

Figure 5.8: Transient evolution of a) soot particle number density; b) the number of primary particles per aggregate; c) soot primary particle diameter; d) soot particle mobility diameter; and e) soot particle gyration diameter, at different nucleation times at 892 K and 398.8 kPa.

5 s, and 10 s. The aggregate number density was found to be directly proportional to the nucleation time. The longer the nucleation time, more the number of particles generated inside the reactor. After the nucleation period, the decline in the aggregate number density was observed for the case where the nucleation time was the largest. The almost constant aggregate number density for the case of 0.5 s and 1 s was attributed to a reduced value of the particle aggregation rate as the initial number of particles decreased by almost three order of magnitude compared to the case where nucleation was allowed to happen for 5 s. Hence, the aggregate number density attained a steady-state value. As the number density was not changing, the number of primary particles in the aggregate did not change. Consequently, the particle mobility and gyration diameters stayed the same with respect to time for the above-mentioned cases. Also, the collision frequency, β, another term responsible for the decrease in the aggregate number density, did not change as the value of the mobility diameter was constant using which the value of β was obtained.

Another observation that was made at 892 K was that when nucleation acted for

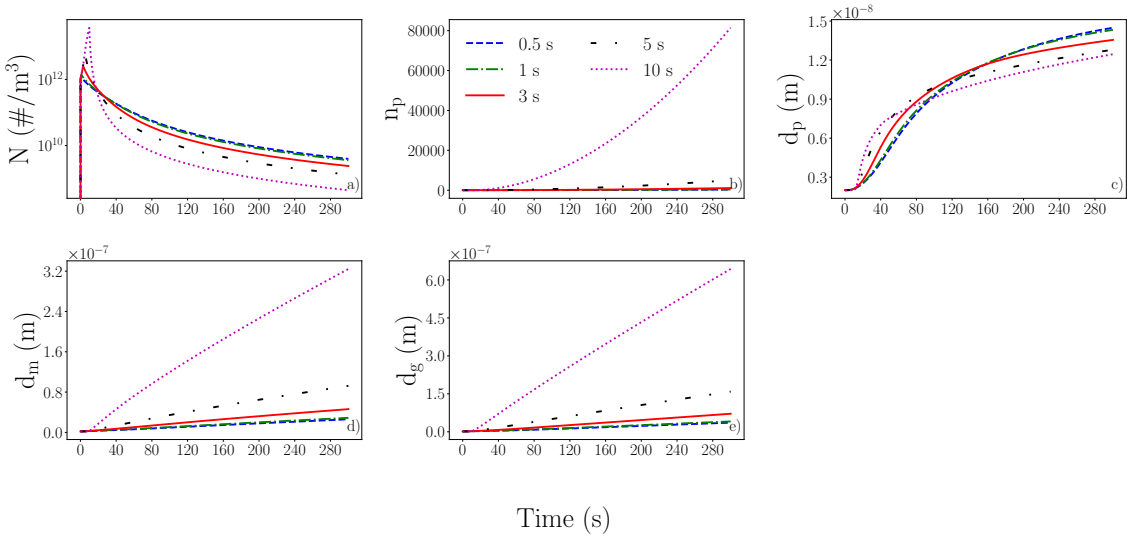

Figure 5.9: Transient evolution of a) soot particle number density; b) the number of primary particles per aggregate; c) soot primary particle diameter; d) soot particle mobility diameter; and e) soot particle gyration diameter, at different nucleation times at 1093 K and 398.8 kPa.

a longer time ($>$ 3 s), most of acetylene in the reactor got consumed in generating newer particles instead of surface growth. Hence, the growth of the primary particles was inhibited without any acetylene left inside the reactor. On the other hand, when the nucleation is limited to below 3 s, the primary particle diameter increases at a much faster rate due to ample amounts of acetylene available in the reactor for surface growth.

Figure 5.9 shows the transient evolution of the aggregate number density, number of primary particles per aggregate, primary particle diameter, particle mobility diameter, and particle gyration diameter at 1093 K and 398.8 kPa assuming the soot nucleation happens for a residence time of 0.5 s, 1 s, 3 s, 5 s, and 10 s. The aggregate number density decreases sharply immediately after the longest nucleation period case (10 s) and the particles decrease at a gradual rate after around 40 s. The longest soot nucleation time gives the smallest primary particle diameter at the end of the reaction due to less availability of acetylene for surface growth. However, the number of primary particles per aggregate increase exponentially due to the fact that

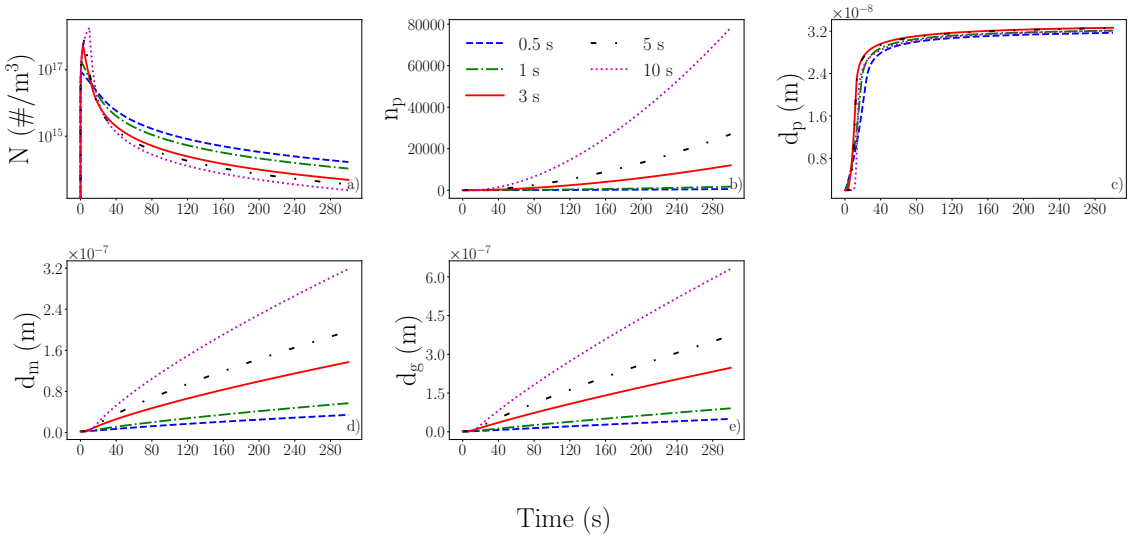

Figure 5.10: Transient evolution of a) soot particle number density; b) the number of primary particles per aggregate; c) soot primary particle diameter; d) soot particle mobility diameter; and e) soot particle gyration diameter, at different nucleation times at 1292 K and 398.8 kPa.

there is no significant increase in the primary particle size due to surface growth. Hence, sticking of bigger particles will only increase the number of primary particles per aggregate, mobility diameter, and the gyration diameter.

Figure 5.10 shows the transient evolution of the aggregate number density, number of primary particles per aggregate, primary particle diameter, particle mobility diameter, and particle gyration diameter at 1292 K and 398.8 kPa assuming the soot nucleation happens for a residence time of 0.5 s, 1 s, 3 s, 5 s, and 10 s. With an increase in the temperature, the aggregate number density increases to 10^{18} particles for the longest nucleation period. In this case, the primary particle diameter attains a steady-state value for all the nucleation periods compared meaning that surface growth at 1292 K happens for a significantly short period of time. Due to the collision of larger particles, the number of primary particles per aggregate increases with residence time and show the largest value for the longest nucleation period.

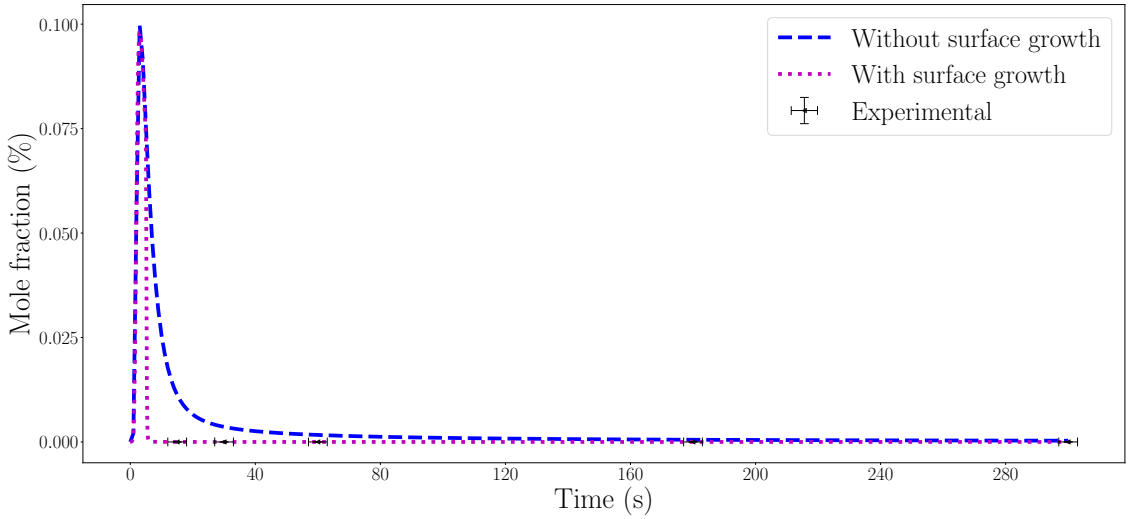

Figure 5.11: Transient evolution of experimental and model predictions of mole fraction (%) of acetylene with and without surface growth at 892 K and 398.8 kPa.

5.2.4.3 Change in acetylene consumption due to surface growth

As acetylene was assumed to be the species for growth on the surface of soot particles, it formation or consumption rate changed with the inclusion of the surface growth model. A parametric study was performed and the change in acetylene consumption was observed at different temperatures with and without the surface growth phenomena. Note that "without surface growth" model corresponds to continuous nucleation of particles from the gas-phase and was given by Equation (2.1.19) in mass terms.

Figure 5.11 shows the experimental data and the optimized model predictions for acetylene mole fraction profile at 892 K and 398.8 kPa with and without the inclusion of the surface growth model. With the inclusion of the surface growth model (after 5 s of nucleation period), acetylene gets instantly consumed from the gas-phase and leads to the growth of the soot particles. As acetylene was almost undetected at 892 K, it means that it got consumed at the very start of the reaction and the optimized model with surface growth gives similar predictions. In the absence of the surface growth model, acetylene consumption rate is comparatively slow and is only due to

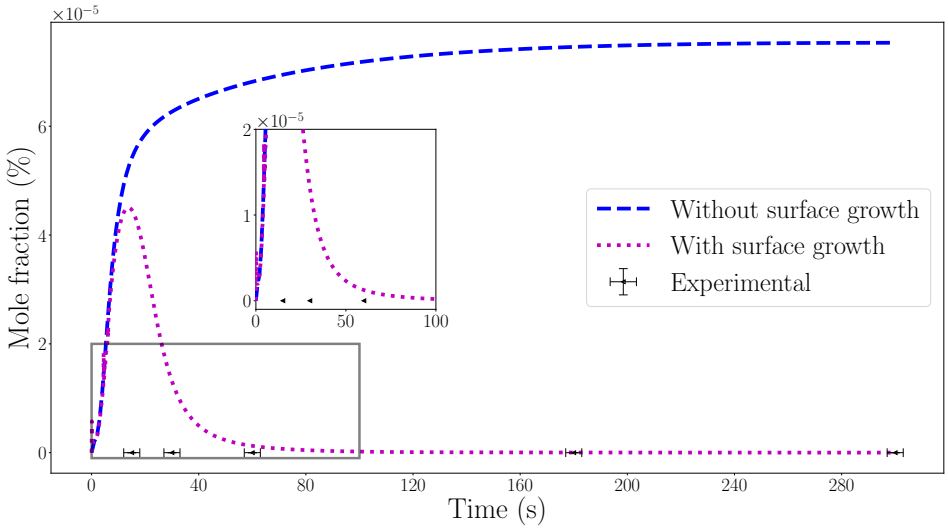

Figure 5.12: Transient evolution of experimental and model predictions of mole fraction (%) of acetylene with and without surface growth at 1093 K and 398.8 kPa.

the nucleation process. The effect of change in acetylene kinetics on particle growth or formation is visible only until around 40 s, after which no acetylene is left inside the reactor. It was hypothesized that the accelerated consumption of acetylene might lead to change in the reaction pathways and a decrease in its concentration gets compensated by further decomposition of light and heavier hydrocarbons, such as methane, benzene and indene, back to acetylene as the sink species. However due to slower kinetics at 892 K, additional acetylene was not observed inside the reactor, both during experiments and in the model.

Figure 5.12 shows the experimental data and optimized model predictions for acetylene mole fraction profile at 1093 K and 398.8 kPa with and without the inclusion of the surface growth model. At 1093 K, acetylene kinetics is governed by the surface growth model. Acetylene concentration increases and attains a steady-state value for pure nucleation case. However, the rate of acetylene consumption significantly increases due to the surface growth model and acetylene reaches a steady-state value of close to zero around 80 s. Both the sub-models, however, overpredict the experimental data profile.

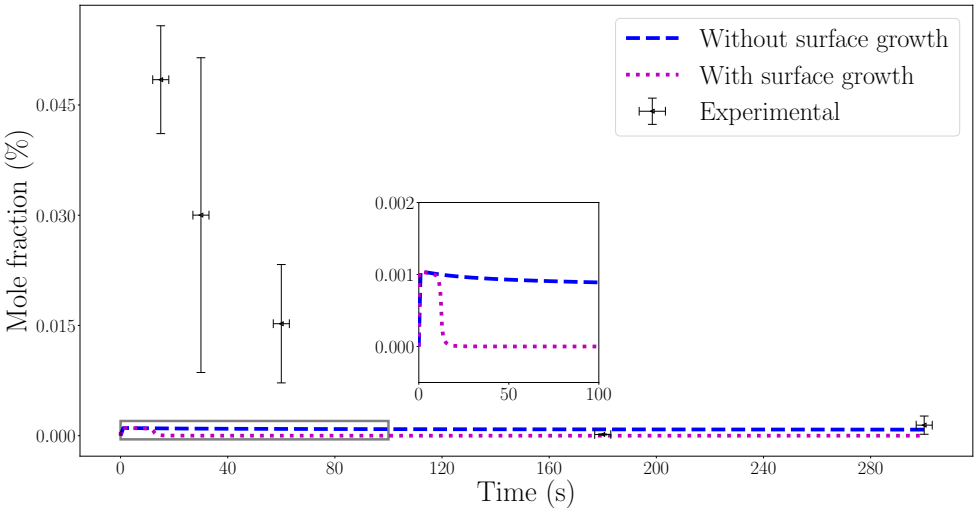

Figure 5.13: Transient evolution of experimental and model predictions of mole fraction (%) of acetylene with and without surface growth at 1292 K and 398.8 kPa.

Figure 5.13 shows the experimental data and the optimized model predictions for acetylene mole fraction profile at 1292 K and 398.8 kPa with and without the inclusion of the surface growth model. At high temperature of 1292 K, the optimized model underpredicts the experimental data in time with or without the surface growth model. In the absence of the surface growth model, acetylene attains a constant mole fraction profile, whereas the mass consumption of acetylene due to the surface growth model is almost instant after the nucleation period.

5.2.4.4 Particle structure

At 892 K, as shown in Figure 5.4, the particle mobility and gyration diameters are close to each other, indicating that the mass distribution inside the aggregate structure is uniform. This means that the aggregate is compact and dense in nature [174]. Once the particles are in point contact with each other, the increase in mass due to surface growth fills the pores in the aggregate leading to a dense structure. Under this case, the particles behave more like a monodisperse population as assumed by the model. The soot particle morphology at 1292 K was also found to show dense par-

ticle characteristics as the mobility and the gyration diameters were found to attain similar values in Figure 5.6d and 5.6e.

At 1093 K, Figure 5.5 shows that the particle mobility and gyration diameters were not close to each other and it was hypothesized that the particle structure was porous and elongated in nature. Ideally, it should be expected that if the soot structure has a uniform mass distribution at 892 K and 1292 K, then the particle structure must show similar characteristics at 1093 K. However, it should be noted that at 892 K and 1292 K, the surface growth phenomenon existed for a short duration of time after the nucleation period, whereas at 1093 K, soot surface growth existed for a comparatively longer duration. The surface growth model is more sensitive to the gyration diameter as compared to the mobility diameter. Hence, the gyration diameter at 1093 K was significantly greater than the mobility diameter of the particle and the soot generated behaves more like a fractal structure. Overall, it can be said that the surface growth model at 1093 K dominates the particle morphology for a longer residence time compared to soot aggregation.

5.2.4.5 Note on collision frequency between the particles

The collision frequency expression in the present work was modified compared to the value proposed by Kholghy et al. [151]. Due to the range of temperatures and residence times studied in the present work which were 892–1292 K compared to 1830 K in the original work related to combustion, the originally proposed values of the collision frequency were found not to be suitable. At lower temperatures of 892 K and 1093 K, the collision frequency was not sufficient enough to sustain soot aggregation, whereas at 1292 K the collision frequency was so high that all the particles generated during nucleation vanished before the simulation finished. Hence, the collision frequency was increased by two orders of magnitude at 892 K and 1093 K to artificially increase the particle collision rate, and lowered by three orders of magnitude at 1292 K to lower the particle collision rate.

Chapter 6

Conclusion and future work[1]

6.1 Conclusion

A batch reactor numerical model including a multi-step kinetic model and a soot formation model was developed. The model was validated in the gas phase by reproducing available experimental literature data and to analyze experimental results from a in-house batch reactor. A H-element flux reaction path analysis was used to identify the most critical reactions.

Comparing the available kinetic models in the literature to high-pressure methane pyrolysis experiments performed in the temperature range of 892–1292 K at a pressure of 4 atm it was observed that the available models were not able to accurately track the decomposition products at low temperatures and elevated pressure neither with nor without carbon formation.

It was only high temperature and pressure (1292 K and 4 atm) that most of the reaction models accurately predicted methane and hydrogen mole fractions, and the first peak of the intermediate products. NUIGMech 1.1 [90] mechanism provided the

[1]Parts of this chapter are reproduced from the following publications:

1. A Punia *et al.*, "Analysis of methane pyrolysis experiments at high pressure using available reactor models," *Chemical Engineering Journal*, p. 144 183, 2023.
2. J. Tatum *et al.*, "Dataset of methane pyrolysis products in a batch reactor as a function of time at high temperatures and pressures," *Data in Brief*, vol. 47, p. 108 953, 2023.
3. A. Punia *et al.*, "A reduced methane pyrolysis mechanism for above-atmospheric pressure conditions," *Chemical Engineering Journal*, vol. (Under review),

Author contributions are detailed in the Preface of this thesis.

best agreement with the sub- and above-atmospheric pressure experimental data.

A reaction path flux analysis showed that the deviation in the model predictions was due to the low reaction rates of fall-off reactions, such as $CH_4 \Longleftrightarrow CH_3 + H$ and $2\ CH_3 \Longleftrightarrow C_2H_6$, under low and medium temperature and high pressure conditions.

A gas-phase model accounting for the solid carbon was implemented based on the reaction of acetylene converting to carbon and hydrogen. The inclusion of the solid carbon did not show any significant rise in methane decomposition at temperatures of 892 K and 1093 K, and at a pressure of 398.8 kPa. At 1292 K and 398.8 kPa, the model overpredicted the experimental data which was attributed to the artificially low activation energy used for the carbon formation. Based on the model results, it was concluded that the rate parameters of the reaction mechanism needed to be tuned for high pressure methane pyrolysis conditions using the presented experimental data.

The original mechanism contained a large number of reactions and species. To reduce the number of design variables for the optimization, a mechanism reduction framework was developed for pyrolysis conditions in this work. Using a graph-based method, DRGEP, a detailed kinetic mechanism consisting of 1516 reactions and 325 species was reduced, in the temperature range 900–1400 K and 0.1–4 atm, to a skeletal mechanism containing 343 reactions and 60 species targeting CH_4, H_2, C_2H_2, C_2H_4, C_2H_6, α-C_3H_4, and p-C_3H_4 . The reduced/skeletal mechanism accurately reproduced the original mechanism predictions within the user-specified error limit.

A reaction mechanism optimization framework was developed and the rate parameters of the reduced mechanism were fitted against the high-pressure data at 892 K, 1093 K, and 1292 K, and 398.8 kPa. The reduced mechanism contained different sets of rate parameters at different pressures, hence the number of design variables were further reduced by selecting the rate parameters for fitting only in the high-pressure limit. The optimized set of rate parameters was able to predict product concentrations in agreement with the experimental data at varying temperatures, as

well as, at low and high-pressures. A high-pressure path flux analysis on carbon element demonstrated that under low-temperature conditions of 892 K and 1093 K, additional pathways, such as C_2H_5 <=> IC_3H_7 <=> NC_3H_7 <=> C_2H_4 <=> C_2H_3 <=> C_2H_2, became activated driving up methane decomposition. The proposed kinetic model is the first available mechanism that can be used to accurately predict methane decomposition for a wide range of operating conditions.

Finally, a monodisperse population balance model for tracking the amount of soot generated, based on the model available in the literature, was integrated into the developed batch reactor with the proposed kinetic model. The soot model implemented was first validated against the results from the literature and then coupled with the optimized kinetic model in Cantera. The developed model is the first to integrate a kinetic pyrolysis model with a soot model for high-pressure methane pyrolysis. The results show that at high-pressure, soot agglomeration is the dominant phenomena and the surface growth plays a comparatively minor role in the particle growth. The primary particles in an aggregate, however, continue to increase thereby increasing its mobility and gyration diameters. A parametric study shows that particle concentration due to nucleation increases with an increase in the temperature, but quickly attains a steady-state value. The effect of varied nucleation times on soot formation showed that longer nucleation times lead to smaller primary particles at the end of the reaction. Another study on the effect of the soot model on the gas-phase showed that acetylene gets quickly consumed in the reactor when the surface growth model is included, whereas without the surface growth model, its consumption was delayed. A particle morphological study shows that at 892 K and 1292 K, the particles behaves as a compact structure with a uniform mass distribution, whereas at 1093 K, the particle appears have more like a porous structure. The coupled gas and the solid-phase model can be used to predict methane thermal decomposition products ranging from the gas-phase to solid-phase in the form of soot.

6.2 Future work

In this study, acetylene was considered as the soot precursor. However, the majority of the studies in the literature have considered heavier hydrocarbons, such as benzene, naphthalene, or pyrene, as the soot precursor. If these species are to be considered as the soot nucleating species, their formation/consumption chemistry in the gas-phase needs to be accurately tracked. Hence, while performing the model reduction, these species should be included as the global quantities of interest. Once the model reduction is achieved, the reduced model can be fitted against the additional high-pressure data for the major species, such as methane and hydrogen, and minor species, such as ethane, ethylene, acetylene, benzene, and naphthalene. The optimized mechanism will be further close to the actual decomposition chemistry for methane.

Another improvement in the soot model is to use the currently implemented soot model in a sectional way. In the present model, the nucleation process is limited to the first five seconds of residence time after which soot surface growth and aggregation/agglomeration takes place. An improved model would use a sectional approach to account for the particle size distribution. This would ensure polydisperity and would be helpful in characterizing the soot particle.

In this work, predictions from the soot model have been provided without any validation. Hence, the soot model will be integrated with a plug flow reactor model in future and validated against the aggregate number density, number of primary particles per aggregate, primary particle diameter, particle mobility diameter, and particle gyration diameter obtained from the inhouse facility and from the literature. Additionally, the effect different soot precursors have on the gas-phase composition will be studied.

Based on the state-of-art literature, one of the key challenges that remain is the unavailability of high-pressure experimental data for methane pyrolysis. The majority of the studies that have been conducted are at atmospheric pressure and this

work is one of the few studies that focused on understanding methane pyrolysis at above-atmospheric pressures. Higher pressures has many advantages, such as higher methane conversions and hydrogen yield, and compact reactor sizes. An extension of this work could be the measurement of major species, such as methane and hydrogen, and minor species, such as ethane, ethylene, acetylene, allene, benzene, and naphthalene, in the temperature range of 900–1400 K and across a pressure range of 4–10 atm. The availability of the data at high-pressure will help in the validation of the proposed kinetic model.

Bibliography

[1] A Punia, J Tatum, L Kostiuk, J Olfert, and M Secanell, "Analysis of methane pyrolysis experiments at high pressure using available reactor models," *Chemical Engineering Journal*, p. 144 183, 2023.

[2] J. Tatum, A. Punia, L. Kostiuk, M. Secanell, and J. Olfert, "Dataset of methane pyrolysis products in a batch reactor as a function of time at high temperatures and pressures," *Data in Brief*, vol. 47, p. 108 953, 2023.

[3] A. Punia, L. Kostiuk, J. Olfert, and M. Secanell, "A reduced methane pyrolysis mechanism for above-atmospheric pressure conditions," *Chemical Engineering Journal*, vol. (Under review),

[4] IEA, "World energy outlook 2023," IEA Paris, France, 2023.

[5] C. A. Tracker, "Climate action tracker," *online:¡ http://climateactiontracker. org*, 2020.

[6] P. IEA, "World energy outlook 2019," *Int. Energy Agency*, 2019. [Online]. Available: https://www.iea.org/reports/world-energy-outlook-2019.

[7] J. C. Minx, W. F. Lamb, M. W. Callaghan, L. Bornmann, and S. Fuss, "Fast growing research on negative emissions," *Environmental Research Letters*, vol. 12, no. 3, p. 035 007, 2017.

[8] J. Wilcox, P. C. Psarras, and S. Liguori, "Assessment of reasonable opportunities for direct air capture," *Environmental Research Letters*, vol. 12, no. 6, p. 065 001, 2017.

[9] A. Abánades *et al.*, "Development of methane decarbonisation based on liquid metal technology for co2-free production of hydrogen," *International Journal of Hydrogen Energy*, vol. 41, no. 19, pp. 8159–8167, 2016.

[10] C Beuttler, L Charles, and J Wurzbacher, "The role of direct air capture in mitigation of anthropogenic greenhouse gas emissions," *Front. Clim. 1: 10. doi: 10.3389/fclim*, 2019.

[11] Y. Wang *et al.*, "A review of low and zero carbon fuel technologies: Achieving ship carbon reduction targets," *Sustainable Energy Technologies and Assessments*, vol. 54, p. 102 762, 2022.

[12] P. Halder *et al.*, "Performance, emissions and economic analyses of hydrogen fuel cell vehicles," *Renewable and Sustainable Energy Reviews*, vol. 199, p. 114 543, 2024.

[13] J. Manna, P. Jha, R. Sarkhel, C. Banerjee, A. Tripathi, and M. Nouni, "Opportunities for green hydrogen production in petroleum refining and ammonia synthesis industries in india," *international journal of hydrogen energy*, vol. 46, no. 77, pp. 38 212–38 231, 2021.

[14] R. Weiss and J. Ikäheimo, "Flexible industrial power-to-x production enabling large-scale wind power integration: A case study of future hydrogen direct reduction iron production in finland," *Applied Energy*, vol. 365, p. 123 230, 2024.

[15] D. Pashchenko, "Green hydrogen as a power plant fuel: What is energy efficiency from production to utilization?" *Renewable Energy*, p. 120 033, 2024.

[16] V. Sage *et al.*, "Recent progress and techno-economic analysis of liquid organic hydrogen carriers for australian renewable energy export–a critical review," *International Journal of Hydrogen Energy*, vol. 56, pp. 1419–1434, 2024.

[17] A. Badakhsh and S. M. Bhagavathy, "Caveats of green hydrogen for decarbonisation of heating in buildings," *Applied Energy*, vol. 353, p. 122 152, 2024.

[18] Y. Goh, S. Lauro, S. T. Barber, S. A. Williams, and T. A. Trabold, "Cleaner production of flexographic ink by substituting carbon black with biochar," *Journal of Cleaner Production*, vol. 324, p. 129 262, 2021.

[19] A. Evans and R. Evans, "The composition of a tyre: Typical components," *The Waste & Resources Action Programme*, vol. 5, 2006.

[20] Y Ding and E Alpay, "Adsorption-enhanced steam–methane reforming," *Chemical Engineering Science*, vol. 55, no. 18, pp. 3929–3940, 2000.

[21] L. J. Catalan and E. Rezaei, "Coupled hydrodynamic and kinetic model of liquid metal bubble reactor for hydrogen production by noncatalytic thermal decomposition of methane," *International journal of hydrogen energy*, vol. 45, no. 4, pp. 2486–2503, 2020.

[22] A. S. Gordon, "Pyrolysis of methane flowing through a porcelain tube in the region 1000," *Journal of the American Chemical Society*, vol. 70, no. 1, pp. 395–401, 1948.

[23] Y. Cangel and M. A. Boles, "Thermodynamics: An engineering approach 4th edition in si units," *Singapore (SI): McGraw-Hill*, 2002.

[24] C. Guéret, M. Daroux, and F. Billaud, "Methane pyrolysis: Thermodynamics," *Chemical Engineering Science*, vol. 52, no. 5, pp. 815–827, 1997.

[25] D Paxman, S Trottier, M. Flynn, L Kostiuk, and M Secanell, "Experimental and numerical analysis of a methane thermal decomposition reactor," *International Journal of Hydrogen Energy*, vol. 42, no. 40, pp. 25 166–25 184, 2017.

[26] G. Fau, N. Gascoin, P. Gillard, and J. Steelant, "Methane pyrolysis: Literature survey and comparisons of available data for use in numerical simulations," *Journal of analytical and applied pyrolysis*, vol. 104, pp. 1–9, 2013.

[27] A. Holmen, O. Olsvik, and O. Rokstad, "Pyrolysis of natural gas: Chemistry and process concepts," *Fuel Processing Technology*, vol. 42, no. 2-3, pp. 249–267, 1995.

[28] D. M. Matheu, W. H. Green Jr, and J. M. Grenda, "Capturing pressure-dependence in automated mechanism generation: Reactions through cycloalkyl intermediates," *International journal of chemical kinetics*, vol. 35, no. 3, pp. 95–119, 2003.

[29] D. M. Matheu, A. M. Dean, J. M. Grenda, and W. H. Green, "Mechanism generation with integrated pressure dependence: A new model for methane pyrolysis," *The Journal of Physical Chemistry A*, vol. 107, no. 41, pp. 8552–8565, 2003.

[30] W. Green *et al.*, "Computer construction of detailed chemical kinetic models for gas-phase reactors," *Industrial & engineering chemistry research*, vol. 40, no. 23, pp. 5362–5370, 2001.

[31] C.-J. Chen, M. Back, and R. Back, "The thermal decomposition of methane. i. kinetics of the primary decompositionto c2h6+ h2; rate constant for the homogeneous unimolecular dissociation of methane and its pressure dependence," *Canadian Journal of Chemistry*, vol. 53, no. 23, pp. 3580–3590, 1975.

[32] C.-J. Chen, M. Back, and R. Back, "The thermal decomposition of methane. ii. secondary reactions, autocatalysis and carbon formation; non-arrhenius behaviour in the reaction of ch3 with ethane," *Canadian Journal of Chemistry*, vol. 54, no. 20, pp. 3175–3184, 1976.

[33] V. S. Arutyunov and V. I. Vedeneev, "Pyrolysis of methane in the temperature range 1000–1700 k," *Russian Chemical Reviews*, vol. 60, no. 12, p. 1384, 1991.

[34] M Plevan *et al.*, "Thermal cracking of methane in a liquid metal bubble column reactor: Experiments and kinetic analysis," *International Journal of Hydrogen Energy*, vol. 40, no. 25, pp. 8020–8033, 2015.

[35] F Billaud, C Gueret, and J Weill, "Thermal decomposition of pure methane at 1263 k. experiments and mechanistic modelling," *Thermochimica acta*, vol. 211, pp. 303–322, 1992.

[36] T. Keipi, T. Li, T. Løvås, H. Tolvanen, and J. Konttinen, "Methane thermal decomposition in regenerative heat exchanger reactor: Experimental and modeling study," *Energy*, vol. 135, pp. 823–832, 2017.

[37] Q. Sun, Y. Tang, and G. R. Gavalas, "Methane pyrolysis in a hot filament reactor," *Energy & fuels*, vol. 14, no. 2, pp. 490–494, 2000.

[38] O. Olsvik, O. A. Rokstad, and A. Holmen, "Pyrolysis of methane in the presence of hydrogen," *Chemical Engineering & Technology: Industrial Chemistry-Plant Equipment-Process Engineering-Biotechnology*, vol. 18, no. 5, pp. 349–358, 1995.

[39] O. Rokstad, O Olsvik, and A Holmen, "Thermal coupling of methane," in *Studies in Surface Science and Catalysis*, vol. 61, Elsevier, 1991, pp. 533–539.

[40] F. G. Billaud, C. P. Gueret, and F. Baronnet, "Thermal coupling of methane in a tubular flow reactor: Experimental setup and influence of temperature," *Industrial & engineering chemistry research*, vol. 31, no. 12, pp. 2748–2753, 1992.

[41] C Gueret and F Billaud, "Thermal coupling of methane: Influence of hydrogen at 1330 c. experimental and simulated results," *Journal of analytical and applied pyrolysis*, vol. 29, no. 2, pp. 183–205, 1994.

[42] D. Murphy, R. Carroll, and J. Klonowski, "Analysis of products of high-temperature pyrolysis of various hydrocarbons," *Carbon*, vol. 35, no. 12, pp. 1819–1823, 1997.

[43] F. G. Billaud, F. Baronnet, and C. P. Gueret, "Thermal coupling of methane in a tubular flow reactor: Parametric study," *Industrial & engineering chemistry research*, vol. 32, no. 8, pp. 1549–1554, 1993.

[44] D. Davidson, M. Di Rosa, A. Chang, R. Hanson, and C. Bowman, "A shock tube study of methane decomposition using laser absorption by ch3," in *Symposium (International) on Combustion*, Elsevier, vol. 24, 1992, pp. 589–596.

[45] V. Arutyunov, V. Vedeneev, R. Moshkina, and V. Ushakov, "Pyrolysis of methane under static conditions at 1100-1400 k," *Kinetics and catalysis*, vol. 32, no. 2, pp. 234–240, 1991.

[46] V Kevorkian, C. Heath, and M. Boudart, "The decomposition of methane in shock waves1," *The Journal of Physical Chemistry*, vol. 64, no. 8, pp. 964–968, 1960.

[47] D. Napier and N Subrahmanyam, "Pyrolysis of methane in a single pulse shock tube," *Journal of Applied Chemistry and Biotechnology*, vol. 22, no. 3, pp. 303–317, 1972.

[48] Y. Hidaka, K. Sato, Y. Henmi, H. Tanaka, and K. Inami, "Shock-tube and modeling study of methane pyrolysis and oxidation," *Combustion and flame*, vol. 118, no. 3, pp. 340–358, 1999.

[49] D Paxman, S Trottier, M Nikoo, M. Secanell, and G. Ordorica-Garcia, "Initial experimental and theoretical investigation of solar molten media methane cracking for hydrogen production," *Energy Procedia*, vol. 49, pp. 2027–2036, 2014.

[50] M. Khan and B. L. Crynes, "Survey of recent methane pyrolysis literature," *Industrial & Engineering Chemistry*, vol. 62, no. 10, pp. 54–59, 1970.

[51] D. Davidson, R. Hanson, and C. Bowman, "Revised values for the rate coefficients of ethane and methane decomposition," *International journal of chemical kinetics*, vol. 27, no. 3, pp. 305–308, 1995.

[52] C. T. Bowman, "Non-equilibrium radical concentrations in shock-initiated methane oxidation," in *Symposium (International) on Combustion*, Elsevier, vol. 15, 1975, pp. 869–882.

[53] H. B. Palmer and T. J. Hirt, "The activation energy for the pyrolysis of methane1," *The Journal of Physical Chemistry*, vol. 67, no. 3, pp. 709–711, 1963.

[54] G. Kozlov and V. Knorre, "Single-pulse shock tube studies on the kinetics of the thermal decomposition of methane," *Combustion and Flame*, vol. 6, pp. 253–263, 1962.

[55] G. B. Skinner and R. A. Ruehrwein, "Shock tube studies on the pyrolysis and oxidation of methane," *The Journal of Physical Chemistry*, vol. 63, no. 10, pp. 1736–1742, 1959.

[56] O Olsvik and F Billaud, "Modelling of the decomposition of methane at 1273 k in a plug flow reactor at low conversion," *Journal of analytical and applied pyrolysis*, vol. 25, pp. 395–405, 1993.

[57] H. B. Palmer, J. Lahaye, and K. C. Hou, "Kinetics and mechanism of the thermal decomposition of methane in a flow system," *The Journal of Physical Chemistry*, vol. 72, no. 1, pp. 348–353, 1968.

[58] A Holmen, O. Rokstad, and A Solbakken, "High-temperature pyrolysis of hydrocarbons. 1. methane to acetylene," *Industrial & Engineering Chemistry Process Design and Development*, vol. 15, no. 3, pp. 439–444, 1976.

[59] M. Serban, M. A. Lewis, C. L. Marshall, and R. D. Doctor, "Hydrogen production by direct contact pyrolysis of natural gas," *Energy & fuels*, vol. 17, no. 3, pp. 705–713, 2003.

[60] O. Rokstad, O Olsvik, B Jenssen, and A Holmen, "Ethylene, acetylene, and benzene from methane pyrolysis," in *Novel Production methods for Ethylene, Light Hydrocarbons, and Aromatics*, M. Dekker New York, 1992.

[61] B. Eisenberg and H. Bliss, "Kinetics of methane pyrolysis," in *Chem. Eng. Prog., Symp. Ser.;(United States)*, Yale Univ., New Haven, CT, vol. 63, 1967.

[62] T Geißler *et al.*, "Experimental investigation and thermo-chemical modeling of methane pyrolysis in a liquid metal bubble column reactor with a packed bed," *International Journal of Hydrogen Energy*, vol. 40, no. 41, pp. 14 134–14 146, 2015.

[63] S. Abanades, H. Kimura, and H. Otsuka, "Kinetic investigation of carbon-catalyzed methane decomposition in a thermogravimetric solar reactor," *International Journal of Hydrogen Energy*, vol. 40, no. 34, pp. 10 744–10 755, 2015.

[64] K. Davis, W Cerven, and W. Solomon, "The use of methane as a fuel for hypersonic propulsion," in *31st Joint Propulsion Conference and Exhibit*, 1995, p. 2769.

[65] J. M. Roscoe and M. J. Thompson, "Thermal decomposition of methane: Autocatalysis," *International journal of chemical kinetics*, vol. 17, no. 9, pp. 967–990, 1985.

[66] L. S. Kassel, "The thermal decomposition of methane1," *Journal of the American Chemical Society*, vol. 54, no. 10, pp. 3949–3961, 1932.

[67] O. A. Rokstad, O. Olsvik, B. Jensen, and A. Holmen, "Innovation and intellectual property rights," in *Novel methods of producing ethylene, other olefins and aromatics*, L. F. Albright, B. L. Crynes, and S. Nowak, Eds., New York: Marcel Dekker, 1992, p. 259.

[68] M. Younessi-Sinaki, E. A. Matida, and F. Hamdullahpur, "Kinetic model of homogeneous thermal decomposition of methane and ethane," *International journal of hydrogen energy*, vol. 34, no. 9, pp. 3710–3716, 2009.

[69] J. Appel, H. Bockhorn, and M. Frenklach, "Kinetic modeling of soot formation with detailed chemistry and physics: Laminar premixed flames of c2 hydrocarbons," *Combustion and flame*, vol. 121, no. 1-2, pp. 122–136, 2000.

[70] H. Le Châtelier, "La loi de le châtelier," *Compt. Rend. l'Acad. Sci*, vol. 99, p. 786, 1884.

[71] F. P. Larkins and A. Z. Khan, "Pyrolysis of methane to higher hydrocarbons: A thermodynamic study," *Australian Journal of Chemistry*, vol. 42, no. 10, pp. 1655–1670, 1989.

[72] M. Steinberg, "Production of hydrogen and methanol from natural gas with reduced co2 emission," *International journal of hydrogen energy*, vol. 23, no. 6, pp. 419–425, 1998.

[73] J. K. Dahl, V. H. Barocas, D. E. Clough, and A. W. Weimer, "Intrinsic kinetics for rapid decomposition of methane in an aerosol flow reactor," *International Journal of Hydrogen Energy*, vol. 27, no. 4, pp. 377–386, 2002.

[74] J. Wyss *et al.*, "Rapid solar-thermal decarbonization of methane in a fluid-wall aerosol flow reactor–fundamentals and application," *International journal of chemical reactor engineering*, vol. 5, no. 1, 2007.

[75] D Trommer, D Hirsch, and A Steinfeld, "Kinetic investigation of the thermal decomposition of ch4 by direct irradiation of a vortex-flow laden with carbon particles," *International Journal of Hydrogen Energy*, vol. 29, no. 6, pp. 627–633, 2004.

[76] S. Abanades and G. Flamant, "Solar hydrogen production from the thermal splitting of methane in a high temperature solar chemical reactor," *Solar Energy*, vol. 80, no. 10, pp. 1321–1332, 2006.

[77] S. Abanades and G. Flamant, "Experimental study and modeling of a high-temperature solar chemical reactor for hydrogen production from methane cracking," *International journal of hydrogen energy*, vol. 32, no. 10-11, pp. 1508–1515, 2007.

[78] S. Rodat, S. Abanades, J. Coulié, and G. Flamant, "Kinetic modelling of methane decomposition in a tubular solar reactor," *Chemical Engineering Journal*, vol. 146, no. 1, pp. 120–127, 2009.

[79] P Homayonifar, Y Saboohi, and B Firoozabadi, "Numerical simulation of nanocarbon deposition in the thermal decomposition of methane," *International Journal of Hydrogen Energy*, vol. 33, no. 23, pp. 7027–7038, 2008.

[80] G. Patrianakos, M. Kostoglou, and A. Konstandopoulos, "One-dimensional model of solar thermal reactors for the co-production of hydrogen and carbon black from methane decomposition," *International Journal of Hydrogen Energy*, vol. 36, no. 1, pp. 189–202, 2011.

[81] N. Ozalp, K. Ibrik, and M. Al-Meer, "Kinetics and heat transfer analysis of carbon catalyzed solar cracking process," *Energy*, vol. 55, pp. 74–81, 2013.

[82] G. P. Smith *et al.*, "Gri-mech 3.0, 1999," *URL http://www. me. berkeley. edu/-gri_mech*, 2011.

[83] C.-W. Zhou *et al.*, "An experimental and chemical kinetic modeling study of 1, 3-butadiene combustion: Ignition delay time and laminar flame speed measurements," *Combustion and Flame*, vol. 197, pp. 423–438, 2018.

[84] L Elliott, D. Ingham, A. Kyne, N. Mera, M Pourkashanian, and C. Wilson, "Genetic algorithms for optimisation of chemical kinetics reaction mechanisms," *Progress in Energy and Combustion Science*, vol. 30, no. 3, pp. 297–328, 2004.

[85] J. R. Fincke, R. P. Anderson, T. A. Hyde, and B. A. Detering, "Plasma pyrolysis of methane to hydrogen and carbon black," *Industrial & Engineering Chemistry Research*, vol. 41, no. 6, pp. 1425–1435, 2002.

[86] H. Wang and M. Frenklach, "Detailed reduction of reaction mechanisms for flame modeling," *Combustion and Flame*, vol. 87, no. 3-4, pp. 365–370, 1991.

[87] E. Ranzi, A. Frassoldati, A. Stagni, M. Pelucchi, A. Cuoci, and T. Faravelli, "Reduced kinetic schemes of complex reaction systems: Fossil and biomass-derived transportation fuels," *International Journal of Chemical Kinetics*, vol. 46, no. 9, pp. 512–542, 2014.

[88] Y Song *et al.*, "The sensitizing effects of no2 and no on methane low temperature oxidation in a jet stirred reactor," *Proceedings of the Combustion Institute*, vol. 37, no. 1, pp. 667–675, 2019.

[89] N. Donato, C. Aul, E. Petersen, C. Zinner, H. Curran, and G. Bourque, "Ignition and oxidation of 50/50 butane isomer blends," *Journal of Engineering for Gas Turbines and Power*, vol. 132, no. 5, 2010.

[90] M. Baigmohammadi *et al.*, "Comprehensive experimental and simulation study of the ignition delay time characteristics of binary blended methane, ethane, and ethylene over a wide range of temperature, pressure, equivalence ratio, and dilution," *Energy & Fuels*, vol. 34, no. 7, pp. 8808–8823, 2020.

[91] M. Y. Sinaki, E. A. Matida, and F. Hamdullahpur, "Development of a reaction mechanism for predicting hydrogen production from homogeneous decomposition of methane," *International Journal of Hydrogen Energy*, vol. 36, no. 4, pp. 2936–2944, 2011.

[92] A. M. Dean, "Detailed kinetic modeling of autocatalysis in methane pyrolysis," *Journal of Physical Chemistry*, vol. 94, no. 4, pp. 1432–1439, 1990.

[93] K. Roy, C. Horn, P. Frank, V. G. Slutsky, and T. Just, "High-temperature investigations on the pyrolysis of cyclopentadiene," in *Symposium (International) on Combustion*, Elsevier, vol. 27, 1998, pp. 329–336.

[94] V. M. Shinde and P. Pradeep, "Detailed gas-phase kinetics and reduced reaction mechanism for methane pyrolysis involved in cvd/cvi processes," *Journal of Analytical and Applied Pyrolysis*, vol. 154, p. 104 998, 2021.

[95] K. E. Niemeyer and C.-J. Sung, "Reduced chemistry for a gasoline surrogate valid at engine-relevant conditions," *Energy & Fuels*, vol. 29, no. 2, pp. 1172–1185, 2015.

[96] T. Lu and C. K. Law, "A directed relation graph method for mechanism reduction," *Proceedings of the Combustion Institute*, vol. 30, no. 1, pp. 1333–1341, 2005.

[97] P. Pepiot-Desjardins and H. Pitsch, "An efficient error-propagation-based reduction method for large chemical kinetic mechanisms," *Combustion and Flame*, vol. 154, no. 1-2, pp. 67–81, 2008.

[98] A. S. Tomlin, M. J. Pilling, T. Turányi, J. H. Merkin, and J. Brindley, "Mechanism reduction for the oscillatory oxidation of hydrogen: Sensitivity and quasi-steady-state analyses," *Combustion and flame*, vol. 91, no. 2, pp. 107–130, 1992.

[99] R. Sankaran, E. R. Hawkes, J. H. Chen, T. Lu, and C. K. Law, "Structure of a spatially developing turbulent lean methane–air bunsen flame," *Proceedings of the combustion institute*, vol. 31, no. 1, pp. 1291–1298, 2007.

[100] X. Zheng, T. Lu, and C. Law, "Experimental counterflow ignition temperatures and reaction mechanisms of 1, 3-butadiene," *Proceedings of the Combustion Institute*, vol. 31, no. 1, pp. 367–375, 2007.

[101] K. E. Niemeyer, C.-J. Sung, and M. P. Raju, "Skeletal mechanism generation for surrogate fuels using directed relation graph with error propagation and sensitivity analysis," *Combustion and flame*, vol. 157, no. 9, pp. 1760–1770, 2010.

[102] S. M. Sarathy *et al.*, "Comprehensive chemical kinetic modeling of the oxidation of 2-methylalkanes from c7 to c20," *Combustion and flame*, vol. 158, no. 12, pp. 2338–2357, 2011.

[103] T. Yao, Y. Pei, B.-J. Zhong, S. Som, T. Lu, and K. H. Luo, "A compact skeletal mechanism for n-dodecane with optimized semi-global low-temperature chemistry for diesel engine simulations," *Fuel*, vol. 191, pp. 339–349, 2017.

[104] X. You, F. N. Egolfopoulos, and H. Wang, "Detailed and simplified kinetic models of n-dodecane oxidation: The role of fuel cracking in aliphatic hydrocarbon combustion," *Proceedings of the combustion institute*, vol. 32, no. 1, pp. 403–410, 2009.

[105] N. Gascoin, A. Navarro-Rodriguez, G. Fau, and P. Gillard, "Kinetic modelling of high density polyethylene pyrolysis: Part 2. reduction of existing detailed mechanism," *Polymer degradation and stability*, vol. 97, no. 7, pp. 1142–1150, 2012.

[106] N. Birakayala and E. A. Evans, "A reduced reaction model for carbon cvd/cvi processes," *Carbon*, vol. 40, no. 5, pp. 675–683, 2002.

[107] Y. Liu, Z. Wang, L. Li, K. Wan, and K. Cen, "Reaction mechanism reduction for ozone-enhanced ch4/air combustion by a combination of directed relation graph with error propagation, sensitivity analysis and quasi-steady state assumption," *Energies*, vol. 11, no. 6, p. 1470, 2018.

[108] E. Gimeno-Escobedo, A. Cubero, J. S. Ochoa, and N. Fueyo, "A reduced mechanism for the prediction of methane-hydrogen flames in cooktop burners," *International Journal of Hydrogen Energy*, vol. 44, no. 49, pp. 27 123–27 140, 2019.

[109] J. Liang, W. Jia, Y. Sun, and Q.-D. Wang, "Skeletal chemical kinetic mechanism generation for methanol combustion and systematic analysis on the ignition characteristics," *Asia-Pacific Journal of Chemical Engineering*, vol. 15, no. 3, e2434, 2020.

[110] M. Frenklach, H. Wang, and M. J. Rabinowitz, "Optimization and analysis of large chemical kinetic mechanisms using the solution mapping method—combustion of methane," *Progress in Energy and Combustion Science*, vol. 18, no. 1, pp. 47–73, 1992.

[111] D. A. Sheen, X. You, H. Wang, and T. Løvås, "Spectral uncertainty quantification, propagation and optimization of a detailed kinetic model for ethylene combustion," *Proceedings of the Combustion Institute*, vol. 32, no. 1, pp. 535–542, 2009.

[112] M. Furst *et al.*, "Optimization of chemical kinetics for methane and biomass pyrolysis products in moderate or intense low-oxygen dilution combustion," *Energy & fuels*, vol. 32, no. 10, pp. 10 194–10 201, 2018.

[113] S. Harris, L Elliott, D. Ingham, M Pourkashanian, and C. Wilson, "The optimisation of reaction rate parameters for chemical kinetic modelling of combustion using genetic algorithms," *Computer methods in applied mechanics and engineering*, vol. 190, no. 8-10, pp. 1065–1090, 2000.

[114] Y. Zhong, Y. Ding, K. Lu, S. Mao, and C. Li, "Kinetic parameters and reaction mechanism study of biomass pyrolysis by combined kinetics coupled with a heuristic optimization algorithm," *Fuel*, vol. 334, p. 126 622, 2023.

[115] K. Wan *et al.*, "Development of reduced and optimized reaction mechanism for potassium emissions during biomass combustion based on genetic algorithms," *Energy*, vol. 211, p. 118 565, 2020.

[116] *MATLAB version 9.10.0.1613233 (R2017a)*, The Mathworks, Inc., Natick, Massachusetts, 2017.

[117] T. Becker, M. Richter, and D. W. Agar, "Methane pyrolysis: Kinetic studies and mechanical removal of carbon deposits in reactors of different materials," *International Journal of Hydrogen Energy*, vol. 48, no. 6, pp. 2112–2129, 2023.

[118] J. Manion *et al.*, "Nist chemical kinetics database, nist standard reference database 17, version 7.0 (web version), release 1.6.8, data version 2015.09, national institute of standards and technology, gaithersburg, maryland, 20899-8320," *Web address: http://kinetics. nist. gov*, 2008.

[119] L. Cai and H. Pitsch, "Mechanism optimization based on reaction rate rules," *Combustion and Flame*, vol. 161, no. 2, pp. 405–415, 2014.

[120] M. E. DESIGNS, "Chemkin-pro," 2011.

[121] C. Version, *3, rotexo-cosilab gmbh & co. kg, bad zwischenahn, germany*, 2009.

[122] B Franzelli, E Riber, M Sanjosé, and T. Poinsot, "A two-step chemical scheme for kerosene–air premixed flames," *Combustion and Flame*, vol. 157, no. 7, pp. 1364–1373, 2010.

[123] R Langer *et al.*, "A comparison of numerical frameworks for modelling homogenous reactors and laminar flames," in *Joint Meeting: The German and Italian Sections of the Combustion Institute-41st Meeting ASICI*, ITA, 2018, pp. 9–14.

[124] D. G. Goodwin, H. K. Moffat, and R. L. Speth, *Cantera: An object-oriented software toolkit for chemical kinetics, thermodynamics, and transport processes*, http://www.cantera.org, Version 2.3.0, 2017. DOI: 10.5281/zenodo.170284.

[125] C. F. F. Rodriguez and J. Mantilla, "Modeling hcci engine combustion coupling cantera to kiva 4," SAE Technical Paper, Tech. Rep., 2015.

[126] V. Ricchiuti, R. Padilla, S Karnani, and D Dunn-Rankin, "Cantera simulations of water-laden methane/air nonpremixed counterflow flames," in *8th US National Combustion. Meeting*, 2013.

[127] A. Cuoci, A. Frassoldati, T. Faravelli, and E. Ranzi, "Opensmoke++: An object-oriented framework for the numerical modeling of reactive systems with detailed kinetic mechanisms," *Computer Physics Communications*, vol. 192, pp. 237–264, 2015.

[128] S. Van Damme, V. Dias, P. Bréquigny, H. Jeanmart, F. Contino, *et al.*, "Comparison of different chemical kinetics modeling codes," in *7th European Combustion Meeting 2015*, 2015.

[129] F. Manenti *et al.*, "Use of detailed kinetic models for multiscale process simulations of sulfur recovery units," in *XXXV Meeting of the italian section of the Combustion Institute*, Associazione sezione italiana del Combustion Institute, 2012, pp. 1–6.

[130] Q. Yang, P. Zhao, and H. Ge, "Reactingfoam-sci: An open source cfd platform for reacting flow simulation," *Computers & Fluids*, vol. 190, pp. 114–127, 2019.

[131] M. Frenklach, D. W. Clary, W. C. Gardiner Jr, and S. E. Stein, "Detailed kinetic modeling of soot formation in shock-tube pyrolysis of acetylene," in *Symposium (International) on Combustion*, Elsevier, vol. 20, 1985, pp. 887–901.

[132] A. J. Josephson, R. R. Linn, and D. O. Lignell, "Modeling soot formation from solid complex fuels," *Combustion and Flame*, vol. 196, pp. 265–283, 2018.

[133] G. Agafonov, A. Borisov, V. Smirnov, K. Y. Troshin, P. Vlasov, and J. Warnatz, "Soot formation during pyrolysis of methane and rich methane/oxygen mixtures behind reflected shock waves," *Combustion science and technology*, vol. 180, no. 10-11, pp. 1876–1899, 2008.

[134] A. Jain and Y. Xuan, "Effects of large aromatic precursors on soot formation in turbulent non-premixed sooting jet flames," *Combustion Theory and Modelling*, vol. 23, no. 3, pp. 439–466, 2019.

[135] A. Attili, F. Bisetti, M. E. Mueller, and H. Pitsch, "Formation, growth, and transport of soot in a three-dimensional turbulent non-premixed jet flame," *Combustion and flame*, vol. 161, no. 7, pp. 1849–1865, 2014.

[136] Q. Mao, A. C. van Duin, and K. Luo, "Formation of incipient soot particles from polycyclic aromatic hydrocarbons: A reaxff molecular dynamics study," *Carbon*, vol. 121, pp. 380–388, 2017.

[137] Y. Matsukawa *et al.*, "Reaction pathway for nascent soot in ethylene pyrolysis," *Combustion and Flame*, vol. 167, pp. 248–258, 2016.

[138] B. Öktem, M. P. Tolocka, B. Zhao, H. Wang, and M. V. Johnston, "Chemical species associated with the early stage of soot growth in a laminar premixed ethylene–oxygen–argon flame," *Combustion and Flame*, vol. 142, no. 4, pp. 364–373, 2005.

[139] M. Frenklach and H. Wang, "Detailed mechanism and modeling of soot particle formation," in *Soot formation in combustion*, Springer, 1994, pp. 165–192.

[140] C. Saggese *et al.*, "Kinetic modeling study of polycyclic aromatic hydrocarbons and soot formation in acetylene pyrolysis," *Energy & fuels*, vol. 28, no. 2, pp. 1489–1501, 2014.

[141] J. T. Mckinnon and J. B. Howard, "The roles of pah and acetylene in soot nucleation and growth," in *Symposium (International) on Combustion*, Elsevier, vol. 24, 1992, pp. 965–971.

[142] H. Wang, "Formation of nascent soot and other condensed-phase materials in flames," *Proceedings of the Combustion institute*, vol. 33, no. 1, pp. 41–67, 2011.

[143] R. Lindstedt and H Bockhorn, "Soot formation in combustion: Mechanisms and models," *Springer-Verlag Series in Chemical Physics*, vol. 59, pp. 417–441, 1994.

[144] J. H. Seinfeld and S. N. Pandis, *Atmospheric chemistry and physics: from air pollution to climate change*. John Wiley & Sons, 2016.

[145] M. Frenklach and S. J. Harris, "Aerosol dynamics modeling using the method of moments," *Journal of colloid and interface science*, vol. 118, no. 1, pp. 252–261, 1987.

[146] S. N. Rogak and R. C. Flagan, "Coagulation of aerosol agglomerates in the transition regime," *Journal of Colloid and Interface Science*, vol. 151, no. 1, pp. 203–224, 1992.

[147] A. Kazakov and M. Frenklach, "Dynamic modeling of soot particle coagulation and aggregation: Implementation with the method of moments and application to high-pressure laminar premixed flames," *Combustion and flame*, vol. 114, no. 3-4, pp. 484–501, 1998.

[148] H Kellerer, R Koch, and S Wittig, "Measurements of the growth and coagulation of soot particles in a high-pressure shock tube," *Combustion and Flame*, vol. 120, no. 1-2, pp. 188–199, 2000.

[149] C. Saggese *et al.*, "Kinetic modeling of particle size distribution of soot in a premixed burner-stabilized stagnation ethylene flame," *Combustion and Flame*, vol. 162, no. 9, pp. 3356–3369, 2015.

[150] M. Sirignano, J. Kent, and A. D'Anna, "Modeling formation and oxidation of soot in nonpremixed flames," *Energy & fuels*, vol. 27, no. 4, pp. 2303–2315, 2013.

[151] M. R. Kholghy and G. A. Kelesidis, "Surface growth, coagulation and oxidation of soot by a monodisperse population balance model," *Combustion and Flame*, vol. 227, pp. 456–463, 2021.

[152] M. Frenklach and H. Wang, "Detailed modeling of soot particle nucleation and growth," in *Symposium (International) on Combustion*, Citeseer, vol. 23, 1991, pp. 1559–1566.

[153] M. Frenklach, "On surface growth mechanism of soot particles," in *Symposium (International) on Combustion*, Elsevier, vol. 26, 1996, pp. 2285–2293.

[154] S. J. Harris and A. M. Weiner, "Determination of the rate constant for soot surface growth," *Combustion Science and Technology*, vol. 32, no. 5-6, pp. 267–275, 1983.

[155] H.-B. Zhang, X. You, and C. K. Law, "Role of spin-triplet polycyclic aromatic hydrocarbons in soot surface growth," *The journal of physical chemistry letters*, vol. 6, no. 3, pp. 477–481, 2015.

[156] H.-B. Zhang, D. Hou, C. K. Law, and X. You, "Role of carbon-addition and hydrogen-migration reactions in soot surface growth," *The Journal of Physical Chemistry A*, vol. 120, no. 5, pp. 683–689, 2016.

[157] M. Frenklach, R. I. Singh, and A. M. Mebel, "On the low-temperature limit of haca," *Proceedings of the Combustion Institute*, vol. 37, no. 1, pp. 969–976, 2019.

[158] S. Rodat, S. Abanades, J.-L. Sans, and G. Flamant, "Hydrogen production from solar thermal dissociation of natural gas: Development of a 10 kw solar chemical reactor prototype," *Solar energy*, vol. 83, no. 9, pp. 1599–1610, 2009.

[159] C. Keramiotis *et al.*, "Experimental and computational study of methane mixtures pyrolysis in a flow reactor under atmospheric pressure," *Energy*, vol. 43, no. 1, pp. 103–110, 2012.

[160] G. Agafonov, V. Smirnov, and P. Vlasov, "Shock tube and modeling study of soot formation during the pyrolysis and oxidation of a number of aliphatic and aromatic hydrocarbons," *Proceedings of the Combustion Institute*, vol. 33, no. 1, pp. 625–632, 2011.

[161] J. Olfert and S. Rogak, "Universal relations between soot effective density and primary particle size for common combustion sources," *Aerosol Science and Technology*, vol. 53, no. 5, pp. 485–492, 2019.

[162] C. Caliot, G. Flamant, G. Patrianakos, M. Kostoglou, and A. G. Konstandopoulos, "Two-dimensional model of methane thermal decomposition reactors with radiative heat transfer and carbon particle growth," *AIChE journal*, vol. 58, no. 8, pp. 2545–2556, 2012.

[163] B. Adams *et al.*, "Dakota: A multilevel parallel object-oriented framework for design optimization, parameter estimation, etc.: Version 6.0 user's manual," Sandia Technical Report SAND2014-4633, Tech. Rep., 2015.

[164] H. Eyring, "The activated complex and the absolute rate of chemical reactions.," *Chemical Reviews*, vol. 17, no. 1, pp. 65–77, 1935.

[165] R. Gilbert, K. Luther, and J Troe, "Theory of thermal unimolecular reactions in the fall-off range. ii. weak collision rate constants," *Berichte der Bunsengesellschaft für physikalische Chemie*, vol. 87, no. 2, pp. 169–177, 1983.

[166] G. Van Rossum and F. L. Drake, *Python 3 Reference Manual*. Scotts Valley, CA: CreateSpace, 2009, ISBN: 1441412697.

[167] W. R. Smith, "Chemical reaction equilibrium analysis," *Theory and Algorithms*, 1982.

[168] K. E. Niemeyer and C.-J. Sung, "On the importance of graph search algorithms for drgep-based mechanism reduction methods," *Combustion and Flame*, vol. 158, no. 8, pp. 1439–1443, 2011.

[169] P. O. Mestas, P. Clayton, and K. E. Niemeyer, *pyMARS v1.1.0*, 2018. DOI: 10.5281/zenodo.1245157. [Online]. Available: https://github.com/Niemeyer-Research-Group/pyMARS.

[170] E. W. Dijkstra, "A note on two problems in connexion with graphs," in *Edsger Wybe Dijkstra: His Life, Work, and Legacy*, 2022, pp. 287–290.

[171] T. H. Cormen, C. E. Leiserson, R. L. Rivest, and C. Stein, *Introduction to algorithms*. MIT press, 2022.

[172] J Revel, J. Boettner, M Cathonnet, and J. Bachman, "Derivation of a global chemical kinetic mechanism for methane ignition and combustion," *Journal de chimie physique*, vol. 91, pp. 365–382, 1994.

[173] F. Gelbard, Y. Tambour, and J. H. Seinfeld, "Sectional representations for simulating aerosol dynamics," *Journal of colloid and interface science*, vol. 76, no. 2, pp. 541–556, 1980.

[174] G. A. Kelesidis, E. Goudeli, and S. E. Pratsinis, "Morphology and mobility diameter of carbonaceous aerosols during agglomeration and surface growth," *Carbon*, vol. 121, pp. 527–535, 2017.

[175] J. T. Edward, "Molecular volumes and the stokes-einstein equation," *Journal of chemical education*, vol. 47, no. 4, p. 261, 1970.

[176] E. K. Lee *et al.*, "Catalytic decomposition of methane over carbon blacks for co2-free hydrogen production," *Carbon*, vol. 42, no. 12-13, pp. 2641–2648, 2004.

Appendix A: Gas-phase experiments and modelling analysis

A.1 Effect of carbon accumulation

Figure A.1 shows the hydrogen and methane concentrations measured by the GC in repeated experiments at 899 K and 1088 K without cleaning the vessel between experiments. Figure A.1a shows that at 899 K there was an increase in methane decomposition as more experiments were completed and thus an increase in the amount of hydrogen created. However, Figure A.1b shows that solid carbon accumulation at 1088 K led to a reduction in methane decomposition and thus a decrease in the amount of hydrogen created. It is generally believed that carbon accumulated on the vessel serves as a catalyst [76] and as carbon is a radiant absorber, it can warm due to radiant heat transfer, catalyzing the reaction further [76]. This means that if there was a small amount of carbon on the walls before the start of the reaction, then there would be a higher conversion efficiency for methane. Lee et al. [176] added carbon black of varying surface area and morphology to a reactor and found all reactions completed with carbon black saw an increase in the decomposition of methane for 1223 K, 1273 K, and 1323 K [176]. They also found that high-temperature reactions (1323 K) are self-catalyzing as more carbon black is generated at high temperatures [176].

The results shown in Figure A.1 show that at 899 K, the carbon acts as a catalyst and the conversion efficiency of the reaction increases as more tests are completed (more carbon accumulates on the reactor walls). However, at 1088 K, the conversion efficiency decreases as more tests are completed. This is the opposite of what was

expected for high-temperature methane pyrolysis. It is unclear why higher temperatures cause solid carbon to decrease the conversion efficiency for this process. Since carbon accumulation clearly affects the reaction rate, all results presented in the results section are after the vessel has been cleaned as described in the experimental methodology.

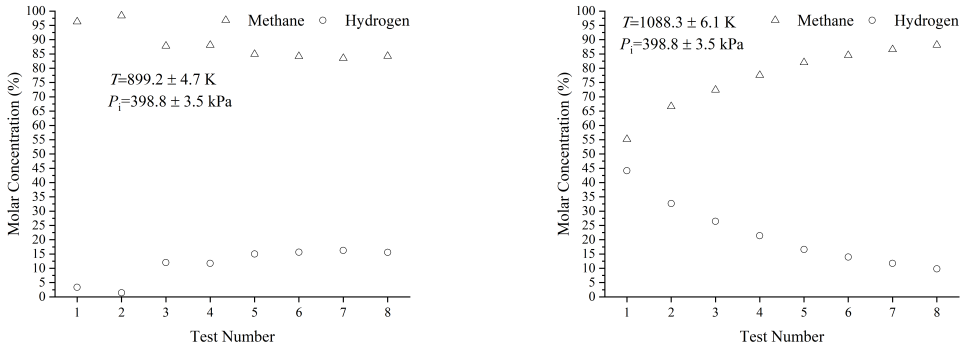

(a) (b)

Figure A.1: Hydrogen production as the test is repeated without cleaning at a) 899 K; and b) 1088 K.

A.2 Reaction path analysis

A reaction path analysis was performed at 892 K, 1093 K and 1292 K and 0.5 atm and 4 atm pressure to identify the slow and fast reactions responsible for hydrogen formation. The flux threshold value at 892 K was kept as 0.001 and at 1093 K and 1292 K, a value of 0.03 was used. Figures A.2, A.3, A.4, A.5, A.6 and A.7 show the reaction path diagrams at the above-mentioned conditions.

A.3 Equilibrium analysis calculation

The equilibrium analysis was performed at 892 K, 1093 K, and 1292 K, and 398.8 kPa to test the consistency of the experimental data obtained. The equilibrium model implemented in Cantera [124] was run at constant temperature and volume based on the concept of minimization of Gibbs free energy. It was assumed that methane,

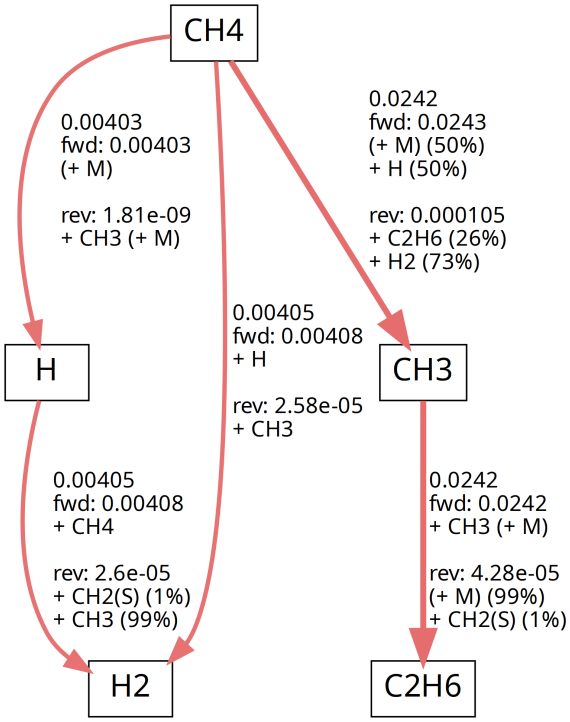

Figure A.2: Reaction flux diagram for hydrogen element at 892 K and 0.5 atm and 300 s. A flux threshold of 0.001 was used to filter the reactions below this value. The reaction mechanism used to generate the flux diagram was taken from reference [90]. 'fwd' and 'rev' are the net forward and reverse hydrogen element fluxes, respectively. The number above the 'fwd' flux represents the net flux as given by Equation (2.2.21).

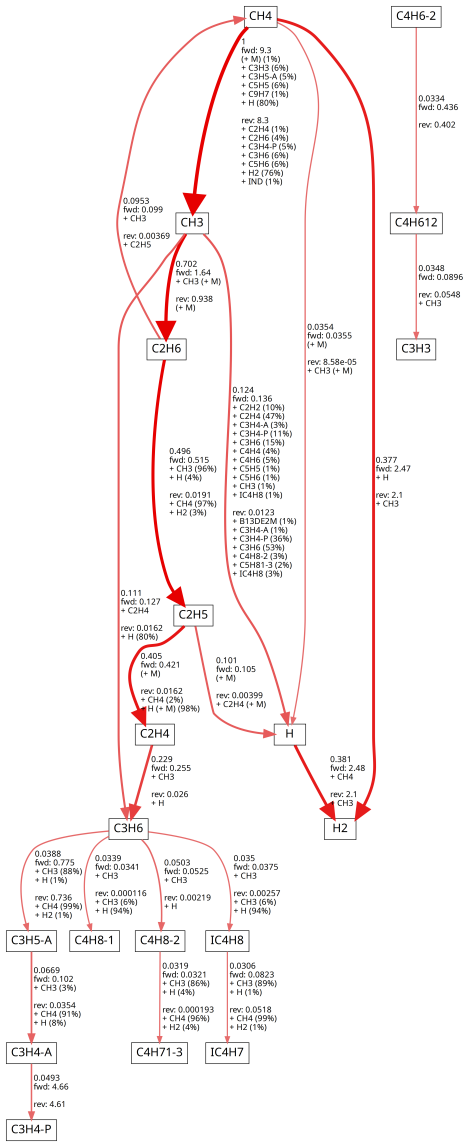

Figure A.3: Reaction flux diagram for hydrogen element at 1093 K and 0.5 atm and 300 s. A flux threshold of 0.03 was used to filter the reactions below this value. The reaction mechanism used to generate the flux diagram was taken from reference [90]. 'fwd' and 'rev' are the net forward and reverse hydrogen element fluxes, respectively. The number above the 'fwd' flux represents the net flux as given by Equation (2.2.21).

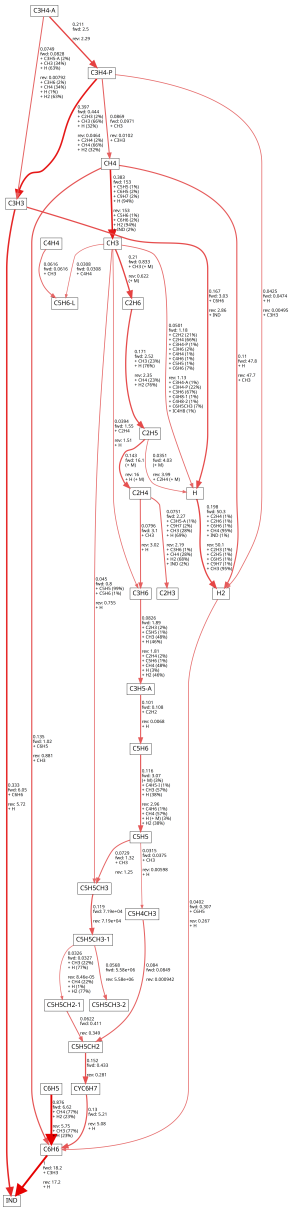

Figure A.4: Reaction flux diagram for hydrogen element at 1292 K and 0.5 atm and 300 s. A flux threshold of 0.03 was used to filter the reactions below this value. The reaction mechanism used to generate the flux diagram was taken from reference [90]. 'fwd' and 'rev' are the net forward and reverse hydrogen element fluxes, respectively. The number above the 'fwd' flux represents the net flux as given by Equation (2.2.21).

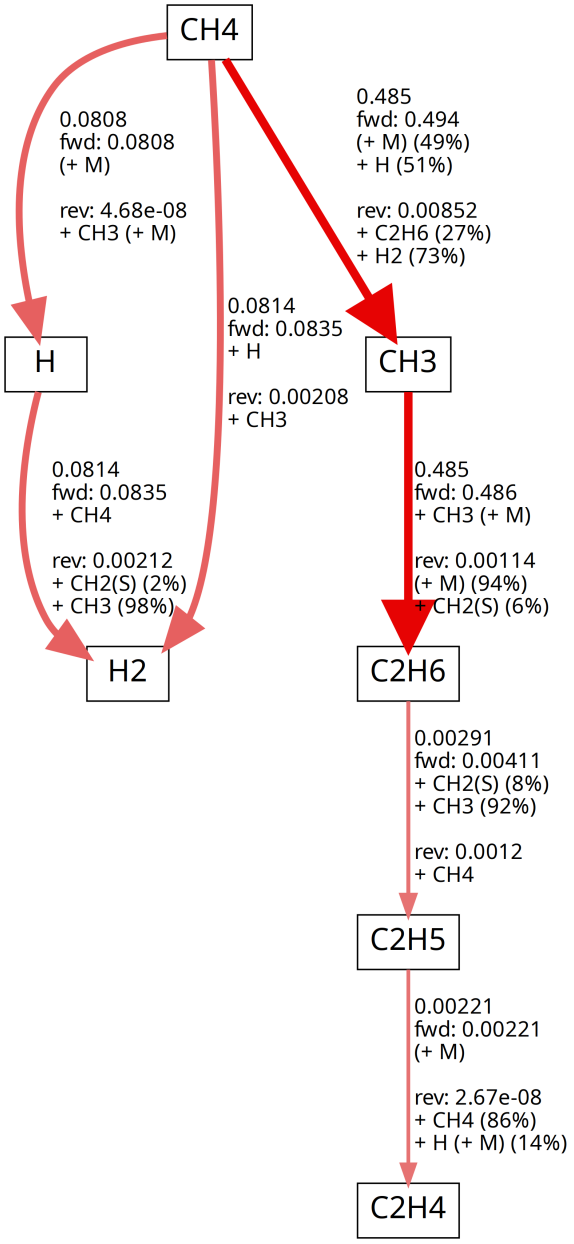

Figure A.5: Reaction flux diagram for hydrogen element at 892 K and 4 atm and 300 s. A flux threshold of 0.001 was used to filter the reactions below this value. The reaction mechanism used to generate the flux diagram was taken from reference [90]. 'fwd' and 'rev' are the net forward and reverse hydrogen element fluxes, respectively. The number above the 'fwd' flux represents the net flux as given by Equation (2.2.21).

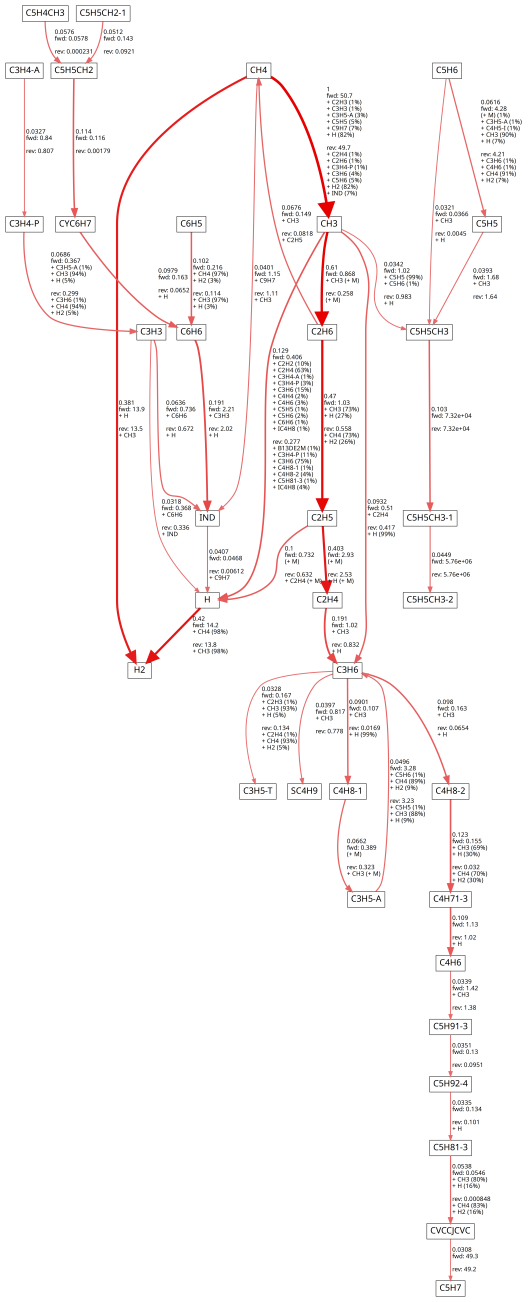

Figure A.6: Reaction flux diagram for hydrogen element at 1093 K and 4 atm and 300 s. A flux threshold of 0.03 was used to filter the reactions below this value. The reaction mechanism used to generate the flux diagram was taken from reference [90]. 'fwd' and 'rev' are the net forward and reverse hydrogen element fluxes, respectively. The number above the 'fwd' flux represents the net flux as given by Equation (2.2.21).

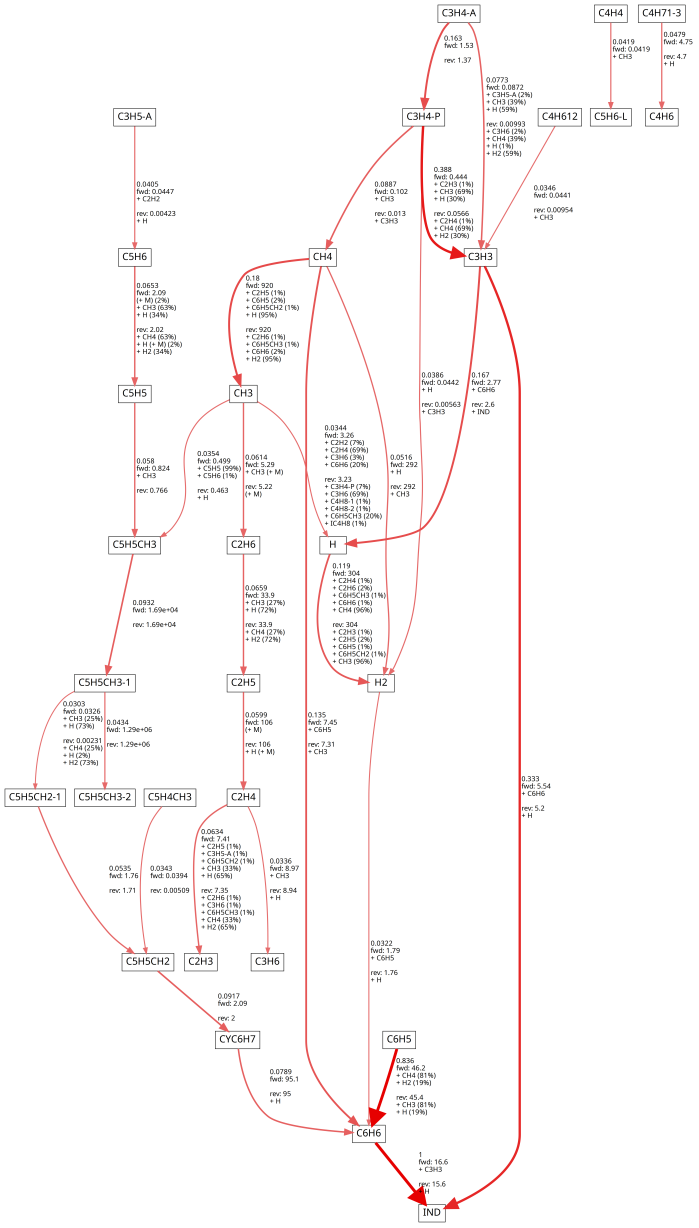

Figure A.7: Reaction flux diagram for hydrogen element at 1292 K and 4 atm and 300 s. A flux threshold of 0.03 was used to filter the reactions below this value. The reaction mechanism used to generate the flux diagram was taken from reference [90]. 'fwd' and 'rev' are the net forward and reverse hydrogen element fluxes, respectively. The number above the 'fwd' flux represents the net flux as given by Equation (2.2.21).

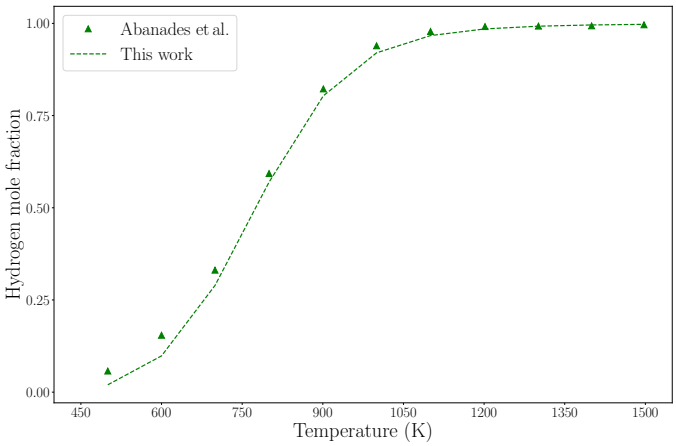

Figure A.8: Comparison of equilibrium hydrogen mole fraction in the gas phase (without solid carbon) obtained at different temperatures and 100 kPa pressure. The reference data for the equilibrium model validation was taken from Abanades et al. [9].

hydrogen, and solid carbon were the only species present inside the reactor. A test validation was performed from the literature [9] to make sure that the equilibrium model is correctly implemented. Figure A.8 shows the test validation performed in the temperature range of 500–1500 K and at 100 kPa. The equilibrium model accurately tracks the gas phase hydrogen mole fraction profile and agreement with the literature data is quite good. Note that the reported equilibrium mole fraction values are calculated from the species in the gas phase, i.e. methane and hydrogen.

Once the equilibrium model implementation was determined to be accurate, the mole fractions of methane and hydrogen, and carbon were separately obtained in the gas and solid phases, respectively, for the present work. This means that the reported equilibrium values of methane and hydrogen mole fractions in the present article reflect the gas-phase mole fractions.

Appendix B: Reaction-type entries and reduced model validation

B.1 Reaction-type entries in Cantera

Figure B.1 shows the rate parameter entry for a fall-off and pressure-dependent-Arrhenius type reaction in the cantera input file [124].

B.2 Model reduction data

Table B.1 gives detailed data about the iterations during the model reduction.

B.3 Reduced model validation under low-pressure conditions

Methane decomposition products predicted by the reduced model were also compared to the original model predictions at the experimental conditions from Chen et al. [31, 32] and Arutyunov et al. [33].

```
- equation: E + F (+M) <=> G (+M)
  type: falloff
  low-P-rate-constant: {A: A_low, b: b_low, Ea: Ea_low}
  high-P-rate-constant: {A: A_high, b: b_high, Ea: Ea_high}
  Troe: {A_troe: a_troe, T3: T3_troe, T1: T1_troe, T2: T2_troe}
  efficiencies: {C2H2: eff1, C2H4: eff2}
```

(a)

```
- equation: A + B <=> C + D
  type: pressure-dependent-Arrhenius
  rate-constants:
  - {P: X atm, A: A_X, b: b_X, Ea: Ea_X}
  - {P: Y atm, A: A_Y, b: b_Y, Ea: Ea_Y}
  - {P: Z atm, A: A_Z, b: b_Z, Ea: Ea_Z}
```

(b)

Figure B.1: Fall-off and pressure-dependent type reactions in Cantera [124] format in the input reaction mechanism.

Table B.1: Reduction in the number of species and reactions with an increase in the error in the reduced model.

Number of species	**Number of reactions**	**Error (η in %)**
325	1516	0
98	554	1.79
87	493	3.05
80	463	6.02
77	441	7.84
73	423	10.84
70	412	11.53
67	378	12.79
60	343	25.69

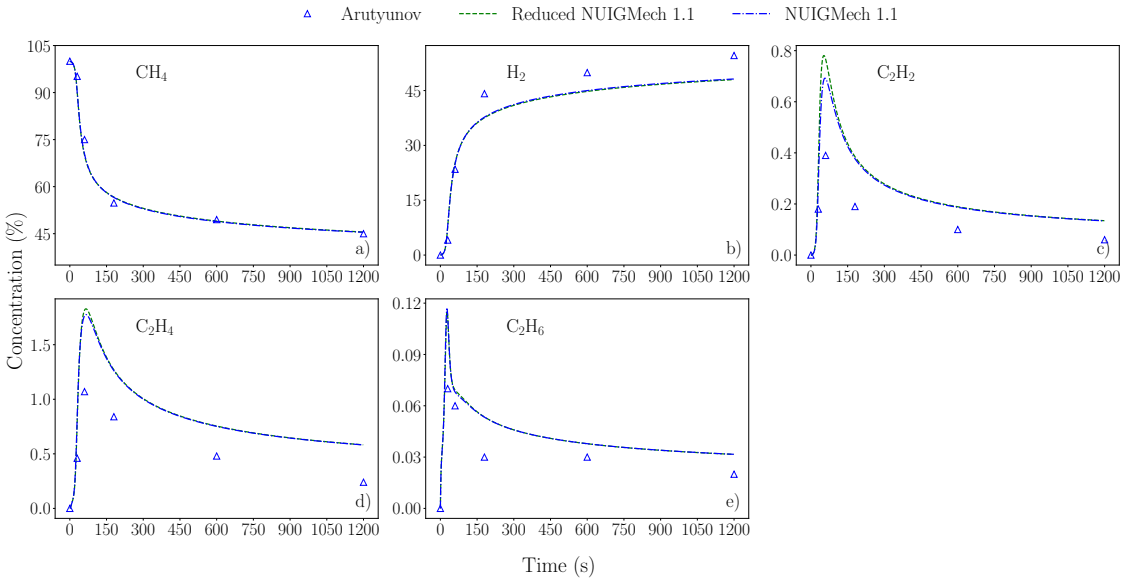

Figure B.2: Comparison of the original and the reduced model predictions at 1200 K and 58 kPa for: a) methane and hydrogen; b) acetylene; c) ethylene; and d) ethane.

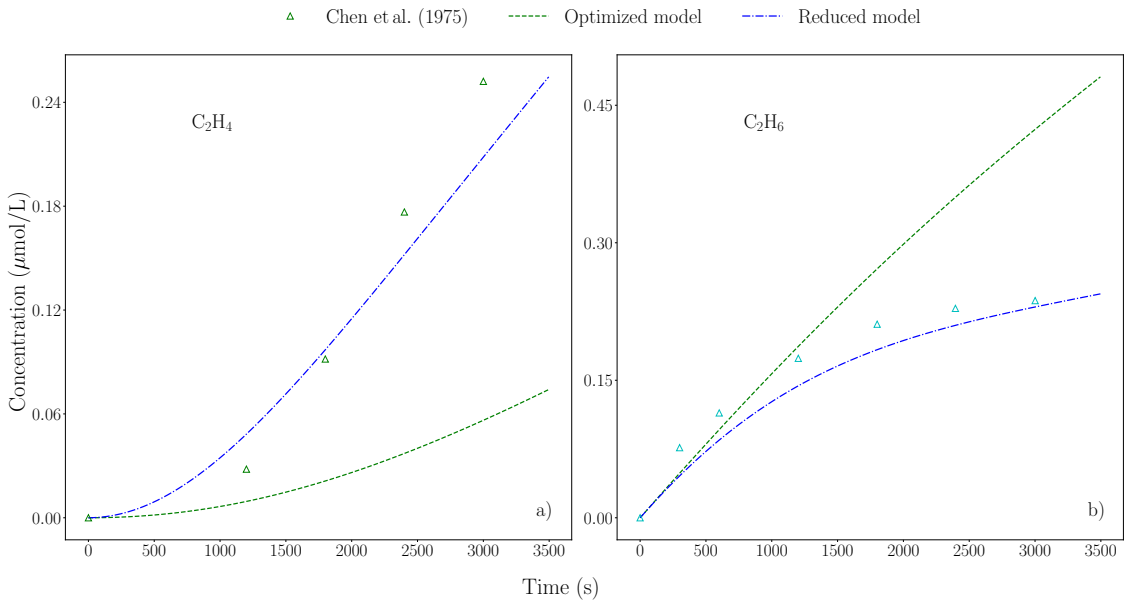

Figure B.3: Comparison of the fitted model predictions against the experimental data at 995 K and 59 kPa for a) ethylene; and b) ethane.

B.3.1 Original vs reduced model predictions

Figure B.2 shows the reduced and the original model predictions at 1200 K and 58 kPa. Almost 50% methane was found to decompose in the first 100 s, after which methane and hydrogen concentrations attained a flat steady-state curve. The intermediate species, on the other hand, attained a peak in the first few seconds of the reaction (< 150 s), followed by a gradual decline in concentrations. The reduced model accurately captured all the concentration profiles, except for the slight overprediction in acetylene concentration at the first peak observed. The magnitude of overprediction was minor and the discrepancy was within a relative error of 10%.

B.3.2 Reduced vs optimized model predictions

Figures B.3 show a comparison of the experimental data and the predictions obtained from the optimized and reduced models at 995 K and 59 kPa. The optimized model accurately predicts ethylene and ethane concentrations for the first 1200 s of residence time. After that, the ethylene concentration is underpredicted, whereas ethane profile

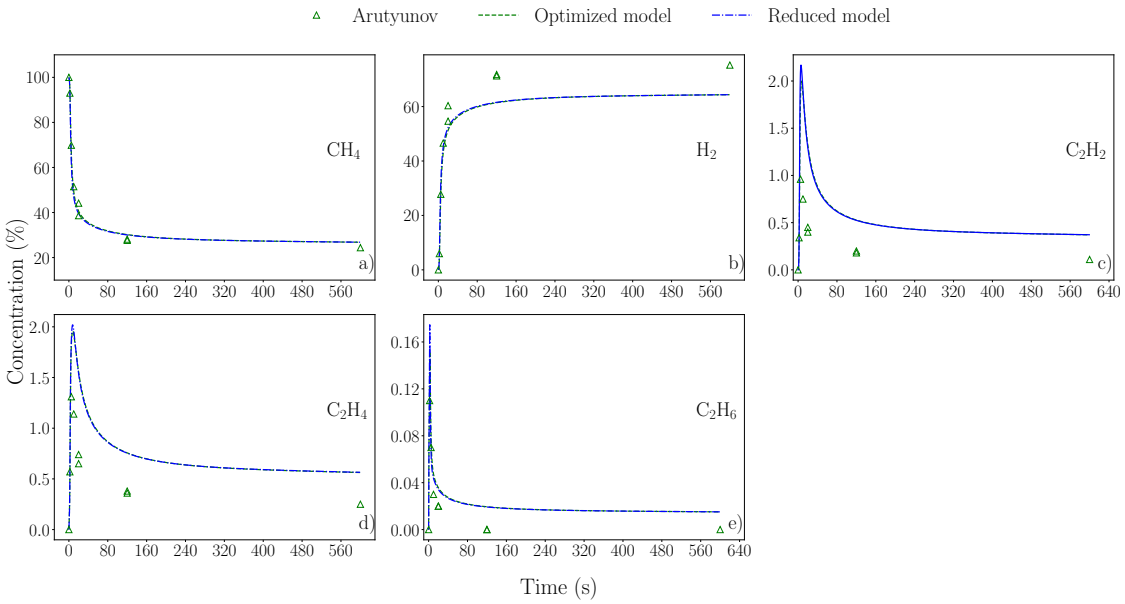

Figure B.4: Comparison of the fitted model predictions against the experimental data at 1300 K and 59 kPa for a) methane; b) hydrogen; c) acetylene; d) ethylene; and e) ethane.

is overpredicted.

Figure B.4 shows the final validation test for the fitted model against the experimental data available in the literature [45] at 1300 K and 59 kPa. The concentrations of methane and hydrogen were well predicted by the optimized model. The minor species were accurately predicted up to the first peak observed after which the species profiles gradually decreased and closely followed the experimental data points.